8-16-2013 12:00 AM

The Study of Nanophotonic Switching Mechanisms in Photonic and Metallic Heterostructures

Joel Cox
The University of Western Ontario

Supervisor
Mahi Singh
The University of Western Ontario

Graduate Program in Physics
A thesis submitted in partial fulfillment of the requirements for the degree in Doctor of Philosophy
© Joel Cox 2013

THE STUDY OF NANOPHOTONIC SWITCHING MECHANISMS IN PHOTONIC
AND METALLIC HETEROSTRUCTURES

(Thesis format: Integrated Article)

by

Joel D. <u>Cox</u>

Graduate Program in Physics

A thesis submitted in partial fulfillment
of the requirements for the degree of
Doctor of Philosophy

The School of Graduate and Postdoctoral Studies
The University of Western Ontario
London, Ontario, Canada

© Joel Douglas Cox 2013

Abstract

In this thesis, nanophotonic switching mechanisms and light-matter interactions are explored in photonic and metallic heterostructures and nanocomposites. These heterostructures are made using various combinations of photonic crystals (PCs), quantum dots (QDs), and graphene or metal nanoparticles (MNPs).

PC heterostructures are formed by combining different PCs so that photons in a specific energy range can propagate in certain regions along one direction and cannot propagate in others. This band structure engineering is used to form photonic quantum wells (PQWs) that have discrete energy states along one dimension. By simulating the photon transmission along the direction of confinement, resonant photon tunnelling is shown to occur at discrete energies. Double PQW (DPQW) heterostructures are also considered, where it is found that resonant states appear in split pairs due to coupling between PQWs.

Nonlinear DPQW heterostructures are also investigated, whereby two regions in the structure are made of Kerr-nonlinear PCs. Here it is shown that the application of an external pump laser field can be used to optically switch the resonant frequencies of bound states in the DPQW.

Energy transfer in a heterostructure made by embedding a QD-graphene nanodisk nanocomposite in a Kerr-nonlinear PC has been studied. Here it is shown that energy transfer occurs between the QD and graphene due to a dipole-dipole interaction. Energy transfer occurs for two distinct frequencies of an external probe laser field, and can be switched by changing the separation between the QD and graphene or by applying a pump laser field to the PC.

An alternative QD-graphene nanocomposite was investigated, where the local field created by plasmons in graphene is used to manipulate two-photon absorption in the QD. An external gate voltage is applied to graphene to modify the plasmon resonance frequency and therefore the frequency at which the local field enhancement has its maximum value. It is demonstrated that two-photon absorption in this nanocomposite can be switched on or off by modifying the gate voltage.

Finally, nonlinear second harmonic (SH) generation and two-photon photoluminescence (TPPL) has been studied experimentally and theoretically in QD-MNP hybrid systems. It is found that a secondary laser field resonant with the plasmons in the MNP can be used to enhance SH generation in the QDs.

Keywords

Nanophotonics, heterostructure, nanocomposite, photonic crystal, quantum dot, graphene, metal nanoparticle, resonant tunnelling, dipole-dipole interaction, plasmon, transfer matrix method, density matrix method

Co-Authorship Statement

This thesis contains both material from previously published manuscripts and unpublished results.

For the material presented in chapters 2 and 3, Joel Cox and Mahi Singh developed the theoretical formalism and wrote the manuscripts. Joel Cox performed the numerical calculations and produced the results in consultation with Mahi Singh.

In chapter 4, Joel Cox and Mahi Singh developed the main theoretical formalism and wrote the manuscript. Godfrey Gumbs, Miguel Antón, and Fernando Carreño contributed to the theory and edited the contents of the manuscript. Joel Cox performed the numerical simulations and produced the results in consultation with Mahi Singh, Miguel Antón, and Fernando Carreño.

In chapter 5, Joel Cox and Mahi Singh developed the theoretical formalism and wrote the manuscript. Joel Cox performed the numerical simulations and produced the results in consultation with Mahi Singh, Miguel Antón, and Fernando Carreño.

In chapter 6, Joel Cox and Mahi Singh developed the theoretical formalism and wrote most of the manuscript. Joel Cox performed the numerical simulations and produced the results in consultation with Mahi Singh. Catalina von Bilderling and Andrea Bragas performed the experimental work and wrote portions of the manuscript pertaining to the experimental methods.

For my family

Acknowledgments

I would like to express my deepest appreciation for my supervisor, Professor Mahi Singh, for his support, guidance, and patience during the past five years. I have been fortunate to have a supervisor who is devoted to his graduate students and who was always available to discuss research projects and answer questions. His vast knowledge of physics and his dedication to research were instrumental in the completion of this thesis.

My graduate experience would have been much more arduous and far less enjoyable without the camaraderie of my fellow group members, both past and present, who I acknowledge here (in order of appearance): Graeme Bart, Chris Racknor, I. Haque, Ali Hatef, and Daniel Schindel. I thank you all for your friendship and support over the years.

The Physics and Astronomy department at Western University has been my home for nearly a decade, and so I would like to extend my thanks to the many talented and knowledgeable faculty members who have taught me over the years, the helpful and friendly staff who have supported me, and the many students, both past and present, who have shared in my academic endeavors thus far.

I would also like to thank my mother, father, and brother for their continual support and unconditional love. My heartfelt appreciation and gratitude goes to my wonderful partner, Jennifer, whose love, encouragement, and kindness over the years helped make all of this possible. To all my friends: Thanks for the countless adventures, good times, and many happy memories.

Finally, I gratefully acknowledge the Ministry of Training, Colleges and Universities, Ontario, Canada, for support in the form of Ontario Graduate Scholarships from May 2011 to April 2013.

Table of Contents

List of Figures

xiv

Chapter 1

Introduction

1.1 Photonic Crystal Heterostructures

Considerable scientific effort has been devoted to the study of materials that can be used to develop the next generation of smaller, faster, and more efficient optoelectronic devices. Towards this end, photonic crystals [1, 2] have been widely studied due to their unique optical properties. Photonic crystals are materials which possess a dielectric constant that varies periodically in one, two, or three spatial dimensions, due to which an energy gap appears in the structure's photonic dispersion relation [3]. This so-called photonic band gap is a range of energies (frequencies) for electromagnetic waves that are prohibited from propagating in a photonic crystal, which gives it the ability to localize and control the flow of light within its structure.

The photonic band gap arises due to periodic multiple partial reflections of electromagnetic waves at the interfaces between alternating dielectric constants in a photonic crystal. For electromagnetic waves with frequencies that lie within the photonic band gap, these multiple reflections occur in phase and constructively interfere so that the incident wave is reflected back completely [3, 4]. The partial reflections of electromagnetic waves with frequencies outside of the photonic band gap are out of phase and destructively interfere, and so these waves can propagate in the photonic crystal with very low attenuation [4]. The frequencies of light that lie within the photonic band gap are determined by the periodic spacing of the constituent dielectric materials in the photonic crystal, and typically the wavelength of light reflected by

a photonic band gap is comparable to the crystal's lattice constant. The size (width) of the energy gap is determined by the contrast between the dielectric materials in the photonic crystal [5].

The photonic band gap in a photonic crystal is often viewed as the photonic analogue of the electronic band gap found in semiconductors [3, 4]. For this reason, significant effort has been devoted to the development of photonic crystal-based optical devices that mimic the functions of electronic semiconductor-based devices, such as transistors, filters, and integrated circuits [3, 6]. Many successful electronic devices have been produced by combining two or more semiconductors with different band gaps to form semiconductor heterostructure devices. In a semiconductor heterostructure, the electronic band gap varies with position, and therefore charge carriers encounter different potential energies in different regions of the structure [6, 7]. This type of band gap engineering can be used to localize or direct the propagation of electrons in a device. One well-known example of an electronic semiconductor heterostructure is the electronic quantum well, in which a thin slab of a semiconductor material with a narrow electronic band gap is placed within another semiconductor material that has a larger band gap. The electric potential of the resulting heterostructure varies along one spatial direction so that a potential well in the narrow-gap semiconductor layer is formed. This potential well confines charge carriers within the narrow-gap semiconductor region, restricting their motion in one dimension to discrete energy states [7]. The energies of these discrete or bound states can be tailored simply by selecting the width of the quantum well.

Photonic crystal heterostructures, the photonic analogue of semiconductor heterostructures, are formed by joining two or more photonic crystals with different photonic band gaps into a single structure. Here the photonic band gap varies with position, and therefore photons will experience different photonic band gaps in different regions of the structure [6]. This method of photonic band gap engineering can therefore be used to efficiently direct and control the propagation of light in an optical device. For example, Lin et al. [8] demonstrated highly efficient waveguiding in a two-dimensional photonic crystal slab waveguide consisting of a triangular array of holes etched through a slab of GaAs. By etching a strip of larger holes in the array, a photonic crystal heterostructure waveguide was formed. In their study, lossless guiding of light at the 1.5 μm telecommunications wavelength was observed. Takano et al. [9]

fabricated a multi-channel drop filter with high efficiency in a two-dimensional photonic crystal slab. Their device consisted of multiple connected photonic crystals composed of etched holes in a Si slab, each with their own lattice constant. Point-defect cavities were introduced in each photonic crystal, and a linear-defect input waveguide ran through each photonic crystal in the heterostructure. For multi-wavelength light propagating through the input waveguide, light matching the resonant frequency of the defect cavity in each photonic crystal region becomes trapped in that cavity, which is then extracted to separate outputs.

Photonic quantum wells [10-18] are a class of photonic crystal heterostructure that produces the photonic analogue of an electronic quantum well. A photonic quantum well can be formed using a low-band gap photonic crystal and a high band-gap photonic crystal, where the upper band edge of the low-band gap photonic crystal lies within the photonic band gap of the high-band gap photonic crystal [6, 12, 14, 15, 17, 18]. The photonic quantum well is formed by sandwiching the low-band gap photonic crystal between two high-band gap photonic crystals. The high-band gap photonic crystals act as potential barriers for photons, and confine light in one dimension within the low-band gap photonic crystal layer. Photons within the low-band gap photonic crystal must occupy bound states with discrete energy levels in the direction of confinement. Alternatively, a photonic quantum well can be fabricated by placing a homogeneous dielectric layer between two photonic crystal barriers [10, 11, 13, 16]. Photons with energies lying within the photonic band gap of the barriers will be confined in one dimension within the dielectric layer, with discrete energy levels along the direction of confinement.

The photonic confinement effect in photonic quantum wells has been studied experimentally in different types of photonic quantum wells made using various photonic crystals [10, 11, 15, 17]. In these studies, bound states in a photonic quantum well were investigated by studying the transmission spectrum for light travelling along the direction of confinement. Electromagnetic modes with a frequency corresponding to a bound state in the photonic well will tunnel through the photonic barriers and occupy that bound state for a finite period of time before escaping by tunnelling back out; thus the photon is said to have occupied a quasi-bound or resonant state within the well [6]. This phenomenon is known as resonant photon tunnelling, and leads to the appearance of discrete, sharp peaks of perfect photon transmittance in the transmission spectrum of a photonic quantum well [10-18]. The principle of resonant photon tunnelling can

be used to select electromagnetic modes of specific frequencies, and therefore can be directly applied to develop high-quality optical filters and resonant cavities using photonic quantum wells [6].

It is well-known that photonic crystals can be used to control the spontaneous emission rate of embedded quantum emitters (e.g. fluorescent atoms, molecules, or nanoparticles) due to their ability to enhance or suppress the electromagnetic (photonic) density of states within their structure [3, 5, 19-23]. The density of states in photonic crystals is strongly reduced or completely inhibited for photon frequencies that lie within the photonic band gap, and enhanced for frequencies outside the photonic band gap and near the photonic band edges. This phenomenon has been experimentally demonstrated by Lodahl et al. [21], who measured the spontaneous emission rate of CdSe quantum dots doped in three-dimensional TiO_2 inverse opal photonic crystals. They found that the spontaneous emission rate of the quantum dots could be either enhanced or suppressed depending on the frequencies of the photonic band gap in a photonic crystal sample. This principle has been used to develop quantum-optical devices that may be used in quantum information processing or ultrafast communication networks, including single-photon sources [22] and all-optical switches [20].

Photonic crystal heterostructures also offer many opportunities to tailor light-matter interactions in optically-active media such as atoms, molecules, or nanoparticles. In photonic heterostructures such as photonic quantum wells or photonic nanowires, electromagnetic modes are quantized along one or two directions. This quantization leads to sharp discontinuities in the photonic density of states corresponding to the energy levels of bound photonic modes. If the resonant frequency of an electronic transition in a quantum emitter matches the energy of a bound photonic state in a photonic quantum well or nanowire, there is a strong dipole-bound photon coupling. This phenomenon has been investigated by Singh, who has studied optical switching in photonic quantum wells [24] and transparency in photonic nanowires [25]. Ma and John have theoretically simulated all-optical logic operations with quantum dots doped in a 2-D/3-D photonic crystal heterostructure made by embedding a two-dimensional photonic crystal slab waveguide within a three-dimensional photonic crystal [26]. Their proposed switching mechanism relies on the sharp discontinuities in the photonic density of states provided by the photonic heterostructure.

1.2   Nonlinear Photonic Crystals

There is great demand for new types of communication and information processing systems that can operate at speeds, bandwidths and efficiencies that surpass those of today's microelectronic devices. For this purpose, photonic crystal-based switching elements have been widely studied in the literature [27-45]. Many photonic crystal switches are based on the idea of shifting the photonic band gap to allow or prevent light of certain frequencies to propagate through the crystal. By tuning the photonic band gap, the transmission of light through a photonic crystal can then be turned "off" or "on." However, the nature of a photonic band gap in a photonic crystal depends on the lattice spacing and sizes of the constituent periodically-arranged dielectric materials as well as their refractive indices. In order to dynamically alter the photonic band gap, one or more of these parameters should therefore be tunable. Typically, the geometry of a photonic crystal cannot be easily modified after it is fabricated [43], and so photonic crystal switching mechanisms usually rely on a modification of the refractive index of the constituent dielectric materials in a crystal.

Early all-optical switching mechanisms for photonic crystals were proposed by Scalora et al. [27] and Tran [29], in which a refractive index change in a photonic crystal was achieved through the nonlinear Kerr effect. The Kerr effect is a third-order nonlinear process by which the refractive index of a medium changes by an amount proportional to the intensity of an external laser field [44-46]. Scalora et al. [27] proposed that the transmission of a probe laser field with a frequency near the photonic band edge of a one-dimensional photonic crystal with a Kerr-nonlinear dielectric component could be switched on or off by applying a sufficiently intense pump laser field. In the "on" state, the frequency of the probe laser lies just outside of the photonic band gap and the probe field is transmitted through the photonic crystal. In the "off" state, the pump laser is applied to the photonic crystal, causing the photonic band gap to shift due to a change in the refractive index of the Kerr-nonlinear material. The frequency of the probe laser field then lies within the photonic band gap and the probe laser can no longer propagate through the photonic crystal. Tran [29] proposed a switching mechanism for a Kerr-nonlinear one-dimensional photonic crystal with a localized state within the photonic band gap that is created by a lattice defect in the crystal. A probe laser with a frequency matching that of the defect state would then propagate through the photonic crystal. When an

intense pump field is applied, the refractive index of the Kerr-nonlinear material shifts, thereby altering the frequency of the localized state. The probe laser field is then completely reflected by the photonic crystal.

Singh and Lipson [40] proposed an alternative all-optical switching mechanism for a Kerr-nonlinear photonic crystal doped with three-level nanoparticles. In this system, the resonance energy of one electronic transition in the nanoparticles lies close to the photonic band edge of the crystal, where the photonic density of states is enhanced. An external laser field couples with another transition in the nanoparticles, probing their absorption spectrum. Here, strong coupling between vacuum photons and the transition dipole moment in the nanoparticles leads to a transparent state in the nanoparticles' absorption spectrum. Upon application of an intense laser field, the photonic band edge of the nonlinear photonic crystal shifts away from the resonance frequency of the nanoparticles. In this case the nanoparticles are switched to an absorbing state.

Tunable photonic crystals that combine liquid crystals with photonic crystals have also been developed. Busch and John [30], for example, proposed a tunable photonic crystal made by infiltrating the void regions in a three-dimensional inverse opal photonic crystal with an optically birefringent nematic liquid crystal. They predicted that the application of an electric field to such a system could completely open or close the photonic band gap. Mertens et al. [33] fabricated three-dimensional macroporous silicon structures filled with a liquid crystal. They demonstrated that the photonic band edge of their photonic crystal can be shifted by changing the temperature.

To achieve ultrafast optical switching in photonic crystals, the response time for the change in a material's refractive index should be very low. Several groups have demonstrated ultrafast all-optical switching mechanisms in semiconductor photonic crystal structures that rely on a nonlinear refractive index change caused by the generation of photo-excited charge carriers [28, 32, 35, 39, 45]. Recently, ultrafast all-optical switching that relies on the nonlinear Kerr effect has been demonstrated in two- and three-dimensional photonic crystals made with polystyrene [36, 37, 41, 45]. Liu et al. [41] constructed a three-dimensional opal polystyrene nonlinear photonic crystal and achieved 10 fs ultrafast all-optical switching using a femtosecond pump-probe technique. The high performance of their all-optical switching mechanism was attributed

to the strong and fast Kerr nonlinear optical response of polystyrene [36, 37, 41-43]. The ultrafast all-optical switching mechanisms described here hold many promising applications in the future development of integrated photonic circuits, optical communication networks and ultrafast information processing systems [45].

1.3 Exciton-Plasmon Interactions in Nanocomposites

There has been growing scientific interest in the optoelectronic properties of nano-scale heterostructure systems composed of different types of nanoparticles. Recent advances in nanofabrication techniques have allowed researchers to combine various nanoparticles with complimentary optical properties into nanocomposite (hybrid) heterostructures, which provides attractive opportunities to modify or design specific optical processes in the constituent nanoparticles [47-60].

A significant amount of research on nanocomposites has been devoted to the study of exciton-plasmon interactions in metal-semiconductor nanostructures, which offer a wide range of opportunities to control light-matter interactions and electromagnetic energy flows on nanometer length scales [47]. In semiconductor nanostructures (i.e., quantum dots), optical excitations are dictated by the discrete energy levels of the electronic states in the semiconductor material's conduction and valence bands. These discrete energy levels depend on the size and shape of the nanostructure, and therefore can be controlled by their fabrication. Optical excitations in semiconductor nanoparticles occur when an electromagnetic field with an appropriate frequency excites an electron from a valence band state to a conduction band state, resulting in the formation of a bound electron-hole pair, or exciton [47].

In metal nanoparticles, optical excitations occur due to the collective oscillations of conduction band electrons driven by an electromagnetic field. These excitations are known as localized plasmons, and their resonance frequency depends on the size, shape, and composition of the metal nanoparticle, as well as the dielectric constant of the surrounding medium [48]. The exciton-plasmon interaction between semiconductor and metal nanoparticles is very strong when the nanoparticles are in close proximity and their optical excitation frequencies are resonant. In metal nanoparticle-semiconductor quantum dot hybrid systems, strong exciton-

plasmon coupling has been found to lead to many interesting effects such as energy transfer, exciton energy shifts, interference, and local field enhancement [47-60].

Theoretical studies of exciton-plasmon interactions in nanocomposite systems have predicted two-photon plasmonic switching phenomena [52], plasmonic electromagnetically induced transparency [56, 57, 59], and selective population transfer in three-level quantum dots [55, 60]. A number of experimental studies on these hybrid systems have also been performed. For example, Mertens et al. [50] demonstrated polarization-selective enhancement of quantum dot photoluminescence in silicon quantum dots coupled with elongated silver nanoparticles. Pons et al. [51] fabricated a CdSe-Zns quantum dot-gold metal nanoparticle hybrid system, where the quantum dot and metal nanoparticle were joined by a variable-length biological linker molecule. They observed quenching of the quantum dot photoluminescence, which was attributed to long-range energy transfer from the quantum dot to the proximal metal nanoparticle. Vasa et al. [53] fabricated a hybrid metal-semiconductor nanostructure consisting of a GaAs quantum well beneath a gold grating. They reported a significant shift and broadening of the quantum well exciton resonance due to strong exciton-plasmon coupling.

1.4 Plasmon-Enhanced Nonlinear Optics in Nanocomposites

Nanocomposite heterostructures that contain plasmonic (i.e. conducting) elements are particularly attractive in the study of nonlinear optical processes [47, 61-71], which scale with a high power of electric field. A number of recent experimental and theoretical studies have demonstrated that nonlinear optical processes such as two-photon absorption/luminescence [61-64] and second- [65, 66, 71] or third-harmonic generation [67] in semiconductor quantum dots can be enhanced by surface plasmons in metal nanoparticles, indicating that quantum dot-metal nanoparticle hybrid systems can be used for nonlinear optical applications such as all-optical switching, biosensing, and other types of signal processing [47, 48, 61, 62].

Nonlinear optical processes such as two-photon absorption and second harmonic generation have been widely studied in nanoparticles for applications in high-resolution scanning optical microscopy and biological imaging [68-70, 72-74]. In particular, two-photon fluorescence from biological markers (dyes, aptamers, etc.) enhanced by noble metal nanoparticles has numerous

applications in biological imaging [68-70, 72-74]. Zhang et al. [69], for example, demonstrated energy transfer between a commonly used molecular DNA label and gold nanoparticles under two-photon excitation using fluorescence lifetime imaging microscopy. They showed that this energy transfer can be used to provide detailed information in biological studies. Li et al. [64] demonstrated the enhancement of quantum dot fluorescence under one- and two-photon excitation in the presence of silica-coated gold nanorods. They concluded that their nanocomposite could be used in biological applications such as bio-imaging or photo-thermal therapy.

Second harmonic generation microscopy of semiconducting nanoparticles has recently emerged as a versatile and robust technique for molecular imaging of living cells and tissues, surpassing the sensitivity and resolution of conventional fluorescence microscopy. However, the second harmonic signal produced by these nanoparticles alone tends to be relatively weak when compared to two-photon fluorescence/luminescence signals [74]. One strategy to improve the intensity of second harmonic generation from semiconductor nanoparticles lies in exploiting the enhanced local field from surface plasmons in a nearby metal nanoparticle. For example, Jais et al. [66] observed an intensity enhancement factor of approximately 1000 for optical second harmonic generation in CdS quantum dots placed near silver nanoparticles. They showed that the metal nanoparticle plasmons are resonantly excited by the second harmonic emission of the quantum dots, indicating that the enhancement of second harmonic generation is mediated by the plasmons. Gong et al. [75] fabricated CdS-Ag core-shell nanocomposites and found that the metal nanoparticles greatly enhanced the optical nonlinearity of the quantum dots. Singh [71] has studied second harmonic generation in a quantum dot-metallic nanoparticle hybrid system, demonstrating that second harmonic generation can be enhanced by the dipole-dipole coupling between a two-photon excited quantum dot and metallic nanoparticle.

1.5   Objective and Outline of Thesis

The aim of this thesis is to explore nanophotonic switching phenomena and light-matter interactions in photonic heterostructures and nanocomposites. These systems are formed by combining two or more micro- or nano-structures with complementary optical properties into single systems, which gives the resulting heterostructure unique optical properties that exceed

the capabilities of its individual components. It is well-known that today's electronic communication and information processing devices are approaching a fundamental limit in their speed and efficiency. The switching mechanisms described in this thesis can be applied towards the development of fundamentally new types of optoelectronic devices that operate at higher speeds and efficiencies, surpassing those of their electronic counterparts. The one- and two-photon switching mechanisms described here can also be applied towards nano-scale sensing applications, whereby a change in an electronic or optical property of a device or nanostructure due to the presence of a substance can alter its optical response. This change in optical response can then be used to detect the substance or determine its optical or electronic properties. Recent advances in nanofabrication techniques have led to an ever-increasing number of available photonic nanostructures which can be used to create the next generation of nano-sensors, communication networks, and computational devices. In this thesis, the optical properties of several types of photonic heterostructures and nanocomposites are investigated theoretically.

The thesis is organized as follows: In Chapter 2 the resonant photonic states of both single- and double-photonic quantum well heterostructures are studied. Using the transfer matrix method, the transmission coefficients for each of these structures along the photon confinement direction are calculated. For the single photonic quantum well heterostructure, isolated peaks of perfect transmission appear in the transmission spectra of the superstructure. These peaks correspond to the bound photonic states in the photonic well, for which resonant photon tunnelling occurs. It is found that by changing the width of the photonic well, the number of resonant transmission states can be controlled. For the double photonic quantum well heterostructure, the simulated transmission spectra indicate that resonant tunnelling peaks occur in split pairs. This splitting is explained in terms of the coupling of degenerate bound photonic states in the individual, isolated photonic quantum wells. By modifying the separation between these photonic wells, the observed spectral splitting can be controlled. The results presented in this chapter indicate that the resonant photonic states in single- or double-photonic quantum wells can be used to develop photonic switching devices, waveguides, or high-quality optical filters.

In Chapter 3, the energy splitting of bound photonic states in Kerr-nonlinear double photonic quantum wells (waveguides) is investigated. Here a double photonic quantum well het-

erostructure is formed by embedding two layers of Kerr-nonlinear photonic crystals in a linear photonic crystal. When an intense laser field is applied to the heterostructure, two coupled waveguides are induced. Due to the coupling between waveguides, degenerate bound states in each waveguide split into symmetric and antisymmetric pairs. Using the transfer matrix method, expressions for the energy levels of these split bound states were obtained. It is shown that the energy splitting depends on the separation of the waveguides as well as the intensity of the applied laser field. The energy splitting predicted by the analytical expression is found to agree well with the splitting of the resonant states shown in the simulated transmission spectra for the heterostructure along the confinement direction. It is demonstrated that the nonlinear double photonic quantum well heterostructure described here can be optically switched between zero to one or more pairs of resonant states. The results described in this chapter can be applied to the development of all-optical switches, tunable filters, and nonlinear coupled waveguides.

In Chapter 4, a nanocomposite heterostructure consisting of a semiconductor quantum dot and a graphene nanodisk is studied. Here, the dipole-dipole coupling between the quantum dot and the graphene nanodisk under the action of external laser fields is explored. Furthermore, it is considered that the quantum dot-graphene nanodisk hybrid is contained within a Kerr-nonlinear photonic crystal. The nonlinear photonic crystal acts as a tunable electromagnetic reservoir for the quantum dot, and is used to further control the energy transfer process. Here the density matrix method is used to calculate the power absorbed by the quantum dot and the power transferred from the quantum dot to graphene. It is found that the spectrum of power absorption in the quantum dot has two peaks due to the creation of two dressed excitons in the presence of the dipole-dipole interaction. The energy transfer rate spectrum for the graphene nanodisk also has two peaks due to the absorption of these two dressed excitons. Energy transfer between the quantum dot and the graphene nanodisk can also be switched on or off by applying a pump laser field to the photonic crystal, or by adjusting the strength of the dipole-dipole interaction. It is shown that the intensities and frequencies of the peaks in the energy transfer rate spectra can be modified by changing the number of graphene monolayers in the nanodisk or the separation between the quantum dot and graphene. These results agree with existing experiments on a qualitative basis. The principle of this system can be used to fabricate nano-scale biosensors, optical switches, and energy transfer devices.

In Chapter 5, nonlinear two-photon absorption and power absorption in a quantum dot-graphene nanoflake nanocomposite system have been investigated theoretically. It is considered that an external laser field is applied to the nanocomposite to simultaneously observe two-photon processes in the quantum dot and excite localized surface plasmons in the graphene nanodisk. This resonance condition can be achieved by tuning the plasmon resonance frequency in the graphene nanoflake via electrostatic gating. In this chapter, the density matrix method has been used to calculate the two-photon absorption coefficient and power absorption in the quantum dot. It is found that the strong local field of the graphene plasmons can enhance and control nonlinear optical processes in the quantum dot. Specifically, it is shown that two-photon absorption in the quantum dot can be switched between single- or double-peaked spectra by modifying the graphene-quantum dot separation. Two-photon absorption and power absorption in the quantum dot can also be switched on or off by slightly changing the gate voltage applied to graphene. The findings presented in this chapter indicate that the present system can be used for nonlinear optical applications such as all-optical switching, biosensing and signal processing.

In Chapter 6, second harmonic generation and two-photon absorption are investigated for CdS quantum dots near metallic nanoparticles. A secondary control laser field is applied to the hybrid system, which couples with the localized plasmons of the metal nanoparticles. The polarized metal nanoparticles then interact with the quantum dots through the dipole-dipole interaction, which enhances the intensity of the second harmonic signal from the quantum dots. The density matrix method is used to numerically simulate the second harmonic signal emitted by the quantum dots. It is found that the enhancement of the second harmonic signal can be switched on and off by changing the control field intensity. Alternatively, the second harmonic signal enhancement can be turned on or of by changing the frequency of the control field. The theoretical results presented here are found to agree with experimental data obtained for CdS quantum dot-metal nanoparticle hybrid systems. This is an interesting finding which can be used to fabricate nonlinear all-optical nano-switching devices from hybrid systems.

Finally, in Chapter 7, the main results of the thesis are summarized and possible future research directions are discussed.

Bibliography

[1] E. Yablonovitch, *Phys. Rev. Lett.* **58**, 2059 (1987).

[2] S. John, *Phys. Rev. Lett.* **58**, 2486 (1987).

[3] J. D. Joannopoulos, S. G. Johnson, J. N. Winn, and R. D. Meade, *Photonic Crystals: Molding the Flow of Light*, 2nd ed. (Princeton University Press, Princeton, New Jersey, 2008).

[4] E. Yablonovitch, *Photonic Crystals: Semiconductors of Light*, Scientific American (December 2001), p. 46.

[5] M. Woldeyohannes and S. John, *J. Opt. B* **5**, R43 (2003).

[6] E. Istrate and E. H. Sargent, *Rev. Mod. Phys.* **78**, 455 (2006).

[7] J. H. Davies, *The Physics of Low-Dimensional Semiconductors: An Introduction* (Cambridge University Press, 1998).

[8] S. Y. Lin, E. Chow, S. G. Johnson, and J. D. Joannopoulos, *Opt. Lett.* **25**, 1297 (2000).

[9] H. Takano, B. S. Song, T. Asano, and S. Noda, *Opt. Expr.* **14**, 3491 (2006).

[10] S. Y. Lin and G. Arjavalingam, *J. Opt. Soc. Am. B* **11**, 2124 (1994).

[11] S. Y. Lin, V. M. Hietala, S. K. Lyo, and A. Zaslavsky, *Appl. Phys. Lett.* **68**, 3233 (1996).

[12] J. Zi, J. Wan, and C. Zhang, *Appl. Phys. Lett.* **73**, 2084 (1998).

[13] Y. Jiang, C. Niu and D. L. Lin, *Phys. Rev. B* **59**, 9981 (1999).

[14] F. Qiao, C. Zhang, J. Wan, and J. Zi, *Appl. Phys. Lett.* **77**, 3698 (2000).

[15] S. Yano, Y. Segawa, J. S. Bae, K. Mizuno, H. Miyazaki, K. Ohtaka, and S. Yamaguchi, *Phys. Rev. B* **63**, 153316 (2001).

[16] X. Chen, W. Lu, and S. C. Shen, *Solid State Commun.* **127**, 541 (2003).

[17] S. H. Xu, Z. H. Xiong, L. L. Gu, Y. Liu, X. M. Ding, J. Zi, and X. Y. Hou, *Solid State Commun.* **126**, 125 (2003).

[18] C. S. Feng, L.-M. Mei, L. Z. Cai, P. Li, and X. L. Yang, *Solid State Commun.* **135**, 330 (2005).

[19] P. Lambropoulos, G. M. Nikolopoulos, T. R. Nielsen, and S. Bay, *Rep. Prog. Phys.* **63**, 455 (2000).

[20] S. John and M. Florescu, *J. Opt. A: Pure Appl. Opt.* **3**, S103 (2001).

[21] P. Lodahl, A. F. van Driel, I. S. Nikolaev, A. Irman, K. Overgaag, D. Vanmaekelbergh, and W. L. Vos, *Nature* **430**, 654 (2004).

[22] A. J. Shields, *Nat. Photon.* **1**, 215 (2007).

[23] S. Noda, M. Fujita, and T. Asano, *Nat. Photon.* **1**, 449 (2007).

[24] M. R. Singh, *Phys. Stat. Sol. A* **206**, 910 (2009).

[25] M. R. Singh, *J. Phys. B: At. Mol. Opt. Phys.* **42**, 065503 (2009).

[26] X. Ma and S. John, *Phys. Rev. A* **84**, 053848 (2011).

[27] M. Scalora, J. P. Dowling, C. M. Bowden, and M. J. Bloemer, *Phys. Rev. Lett.* **73**, 1368 (1994).

[28] P. R. Villeneuve, D. S. Abrams, S. Fan, and J. D. Joannopoulos, *Opt. Lett.* **21**, 2017 (1996).

[29] P. Tran, *J. Opt. Soc. Am. B* **14**, 2589 (1997).

[30] K. Busch and S. John, *Phys. Rev. Lett.* **83**, 967 (1999).

[31] M. F. Yanik, S. Fan, and M. Soljačić, *Appl. Phys. Lett.* **83**, 2739 (2003).

[32] D. A. Mazurenko, R. Kerst, J. I. Dijkhuis, A.V. Akimov, V.G. Golubev, D. A. Kurdyukov, A. B. Pevtsov, and A.V. Sel'kin, *Phys. Rev. Lett.* **91**, 213903 (2003).

[33] G. Mertens, T. Röder, H. Matthias, H. Marsman, H.-S. R. Kitzerow, S. L. Schweizer, C. Jamois, R. B. Wehrspohn, and M. Neubert, *Appl. Phys. Lett.* **83**, 3036 (2003).

[34] H. Nakamura, Y. Sugimoto, K. Kanamoto, N. Ikeda, Y. Tanaka, Y. Nakamura, S. Ohkouchi, Y. Watanabe, K. Inoue, H. Ishikawa, and K. Asakawa, *Opt. Expr.* **12**, 6606 (2004).

[35] T. Tanabe, M. Notomi, S. Mitsugi, A. Shinya, and E. Kuramochi, *Appl. Phys. Lett.* **87**, 151112 (2005).

[36] X. Hu, Y. Liu, J. Tian, B. Cheng, and D. Zhang, *Appl. Phys. Lett.* **86**, 121102 (2005).

[37] Y. Liu, X. Hu, D. Zhang, B. Cheng, and D. Zhang, *Appl. Phys. Lett.* **86**, 151102 (2005).

[38] N. Yamamoto, T. Ogawa, and K. Komori, *Opt. Expr.* **14**, 1223 (2006).

[39] T. Tanabe, K. Nishiguchi, A. Shinya, E. Kuramochi, H. Inokawa, M. Notomi, K. Yamada, T. Tsuchizawa, T. Watanabe, H. Fukuda, H. Shinojima, and S. Itabashi, *Appl. Phys. Lett.* **90**, 031115 (2007).

[40] M. R. Singh and R. Lipson, *J. Phys. B: At. Mol. Opt. Phys.* **41**, 015401 (2008).

[41] Y. Liu, F. Qin, Z.-Y. Wei, Q.-B. Meng, D.-Z. Zhang, and Z.-Y. Li, *Appl. Phys. Lett.* **95**, 131116 (2009).

[42] Y. Lin, F. Qin, F. Zhou and Z.-Y. Li, *J. Appl. Phys.* **106**, 083102 (2009).

[43] F. Qin, Y. Liu and Z.-Y. Li, *J. Opt.* **12**, 035209 (2010).

[44] *Nonlinear Photonic Crystals*, edited by R. E. Slusher and B. J. Eggleton (Springer-Verlag, Berlin, 2003).

[45] V. G. Golubev (2012), Ultrafast All-Optical Switching in Photonic Crystals. In M. F. Limonov and R. M. De La Rue (Eds.), Optical Properties of Photonic Structures: Interplay of Order and Disorder (pp. 415-428). Boca Raton, FL: Taylor & Francis Group.

[46] R. W. Boyd, *Nonlinear Optics*, 3rd ed. (Academic, New York, 2008).

[47] M. Achermann, *J. Phys. Chem. Lett.* **1**, 2837 (2010).

[48] T. O'Connor and M. Zamkov (2013), Optical Properties of Nanocomposites. In C. Kumar (Ed.), UV-VIS and Photoluminescence Spectroscopy for Nanomaterials Characterization (pp. 485-529). Heidelberg: Springer-Verlag Berlin.

[49] W. Zhang, A. O. Govorov, and G. W. Bryant, *Phys. Rev. Lett.* **97**, 146804 (2006).

[50] H. Mertens, J. S. Biteen, H. A. Atwater, and A. Polman, *Nano Lett.* **6**, 2622 (2006).

[51] T. Pons, I. L. Medintz, K. E. Sapsford, S. Higashiya, A. F. Grimes, D. S. English, and H. Mattoussi, *Nano Lett.* **7**, 3157 (2007).

[52] D. E. Chang, A. S. Sørensen, E. A. Demler, and M. D. Lukin, *Nat. Phys.* **3**, 807 (2007).

[53] P. Vasa, R. Pomraenke, S. Schwieger, Yu. I. Mazur, Vas. Kunets, P. Srinivasan, E. Johnson, J. E. Kihm, D. S. Kim, E. Runge, G. Salamo, and C. Lienau, *Phys. Rev. Lett.* **101**, 116801 (2008).

[54] M. Durach, A. Rusina, V. I. Klimov, and M. I. Stockman, *New J. Phys.* **10**, 105011 (2008).

[55] M.-T. Cheng, S.-D. Liu, and Q.-Q. Wang, *Appl. Phys. Lett.* **92**, 162107 (2008).

[56] S. M. Sadeghi, L. Deng, X. Li, and W.-P. Huang, *Nanotechnology* **20**, 365401 (2009).

[57] R. D. Artuso and G. W. Bryant, *Phys. Rev. B* **82**, 195419 (2010).

[58] J. M. Luther, P. K. Jain, T. Ewers, and A. P. Alivisatos, *Nat. Mater.* **10**, 361 (2011).

[59] M. Singh, D. G. Schindel, and A. Hatef, *Appl. Phys. Lett.* **99**, 181106 (2011).

[60] M. A. Antón, F. Carreño, S. Melle, O. G. Calderón, E. Cabrera-Granado, J. Cox, and M. R. Singh, *Phys. Rev. B* **86**, 155305 (2012).

[61] M. Fu, K. Wang, H. Long, G. Yang, P. Lu, F. Hetsch, A. S. Susha, and A. L. Rogach, *Appl. Phys. Lett.* **100**, 063117 (2012).

[62] B. P. Khanal, A. Pandey, L. Li, Q. Lin, W. K. Bae, H. Luo, V. I. Klimov, and J. M. Pietryga, *ACS Nano* **6**, 3832 (2012).

[63] S. Xiao, H. Gong, X. Su, J. Han, Y. Han, M. Chen, and Q. Wang, *J. Phys. Chem. C* **111**, 10185 (2007).

[64] X. Li, F. -J. Kao, C. -C. Chuang, and S. He, *Opt. Express* **18**, 11335 (2010).

[65] E. Shaviv and U. Banin, *ACS Nano* **4**, 1529 (2010).

[66] P. M. Jais, C. von Bilderling, and A. V. Bragas, *Papers in Physics* **3**, 030002 (2011).

[67] X. Feng, Y. Chen, and D. Hou, *Physica B* **406**, 1702 (2011).

[68] N. J. Durr, T. Larson, D. K. Smith, B. A. Korgel, K. Sokolov, and A. Ben-Yakar, *Nano Lett.* **7** 941 (2007).

[69] Y. Zhang, D. J. S. Birch, and Y. Chen, *Appl. Phys. Lett.* **99** 103701 (2011).

[70] A. Ray, Y.-E. K. Lee, G. Kim, and R. Kopelman, *Small* **8**, 2213 (2012).

[71] M. R. Singh, *Nanotechnology* **24**, 125701 (2013).

[72] M. Zielinski, D. Oron, D. Chauvat, and J. Zyss, *Small* **5**, 2835 (2009).

[73] A. A. Umar, A. H. Reshak, M. Oyama, and K. J. Plucinski, *J. Mater. Sci.: Mater. Electron.* **23**, 546 (2012).

[74] W. P. Dempsey, S. E. Fraser, and P. Pantazis, *Bioessays* **34**, 351 (2012).

[75] H. M. Gong, X. H. Wang, Y. M. Du, and Q. Q. Wang, *J. Chem. Phys.* **125**, 024707 (2006).

Chapter 2

Photon Tunnelling in Photonic Crystal Heterostructures

In the previous chapter, the background material pertaining to the topics and systems studied in this thesis was reviewed. Here, the resonant photonic states in single and double photonic quantum well heterostructures are studied[1]. The resonant tunnelling phenomenon that occurs in these photonic heterostructures is also investigated.

2.1 Introduction

Photonic crystals [1, 2] have attracted a great deal of attention due to their ability to localize and control the flow of light within their structure. Considerable effort has been placed into finding ways to harness their potential for developing new photonic devices. To that end, photonic crystal heterostructures have provided a promising means for turning raw photonic crystals into functional devices [3, 4].

Photonic crystals are materials with a periodically modulating dielectric constant, which may vary in one, two, or three spatial dimensions. Due to this periodic dielectric modulation, a band gap forms in the structure's photonic dispersion relation. Light possessing a frequency within this gap is prevented from propagating in the photonic crystal. Photonic crystal het-

---

[1]The material presented in this chapter has been published in: M. R. Singh and J. D. Cox, *AIP Conf. Proc.* **1147**, 256 (2009) and J. D. Cox and M. R. Singh, *Nanoscale Res. Lett.* **5**, 484 (2010).

erostructures, as their name implies, are formed by joining two or more photonic crystals into a single structure. Combining various photonic crystals with different band gaps into a single heterostructure gives it a more complicated band structure than that of a bulk photonic crystal, which allows for greater customization and control over how light propagates within the overall structure. Photonic crystal heterostructures have been used to develop devices such as high-quality resonant cavities [6, 7], low-loss waveguides [8], and high efficiency add-drop filters [9].

Photonic quantum wells (PQWs) are a class of photonic crystal heterostructure that possess a distinct photonic band structure. A PQW consists of a photonic well embedded between two photonic barriers. The photonic barriers are photonic crystals with band gaps that may be regarded as potential barriers for photons, whereas the photonic well consists of either a uniform dielectric material or another photonic crystal with a different band gap than that of the barrier. Due to the photonic band gap mismatch between the well and the barrier, photons become confined within the well and occupy quantized states along one direction. This so-called photonic confinement effect has been studied in different types of PQWs made using various photonic crystals [10-23].

It has been shown that the phenomenon of resonant photonic tunnelling can occur for a PQW with sufficiently thin photonic barriers [12-14]. Resonant tunnelling occurs when a photon with an energy corresponding to a bound state of the PQW tunnels through one of the barriers, where it occupies this bound state within the well for a finite period of time before escaping by tunnelling back out; thus the photon is said to have occupied a quasi-bound or resonant state within the PQW [5]. As a consequence of this phenomenon, an incident photon with an energy matching a resonant state of the PQW will undergo perfect transmission through both barriers. In the transmission spectrum of a PQW, resonant states appear as sharp peaks approaching unity [10-23].

In this chapter, resonant photonic states in both single PQW and double photonic quantum well (DPQW) heterostructures are investigated. A DPQW heterostructure is formed by simply adding another photonic well and photonic barrier to a single PQW system. Using the transfer matrix method [24] the transmission coefficient of these heterostructures along the direction of photon confinement is calculated as a function of the incident photon energy. For the PQW

heterostructure, photons which would otherwise be prevented from travelling through the heterostructure by the photonic barriers undergo perfect transmission through the entire device at specific, discrete energies. It is shown that by adjusting the width of the photonic well, the number of resonant photon tunnelling states in the transmission spectrum can be controlled. For the DPQW heterostructure, the transmission spectra indicate that resonant photon tunnelling states occur in pairs. The numerical simulations for the transmission spectra of these structures reveals that the number of pairs of resonant tunnelling states depends on the width of the photonic wells. By changing the separation of the photonic wells, the energy splitting between the individual resonant tunnelling states in a transmitted pair can be controlled. It is anticipated that the resonant tunnelling states described here will be useful for developing new types of photonic switching devices, optical filters, and other optoelectronic devices [4, 10-23].

2.2   Theoretical Formalism

A PQW heterostructure can be formed using two different photonic crystals, which are denoted as A and B. Photonic crystal A is used as the photonic well in the heterostructure, while photonic crystal B denotes the photonic barriers which confine light within the well. The PQW heterostructure considered here is constructed by embedding two parallel and separate planar layers (i.e. slabs) of photonic crystal B within photonic crystal A, as illustrated in Figure 2-1. In the present heterostructure there are five regions, i.e., the total system can be denoted as $A_1/B_2/A_3/B_4/A_5$.

Incident transverse electric (TE)-polarized electromagnetic waves propagating along the x-direction in the heterostructure are described as Bloch waves, with wave vectors denoted by K_A and K_B in photonic crystals A and B, respectively. The electric field in the jth region of the heterostructure is then given as

$$E_j(x) = \alpha_j e^{ik_j x} + \beta_j e^{-ik_j x},\tag{2.1}$$

where α_j and β_j are the incident and reflected electric field amplitudes, respectively, in the jth layer of the PQW heterostructure, and k_j is the wave vector for photons propagating in the jth region. For the present PQW heterostructure the wave vectors are $k_1 = k_3 = k_5 = K_A$ and
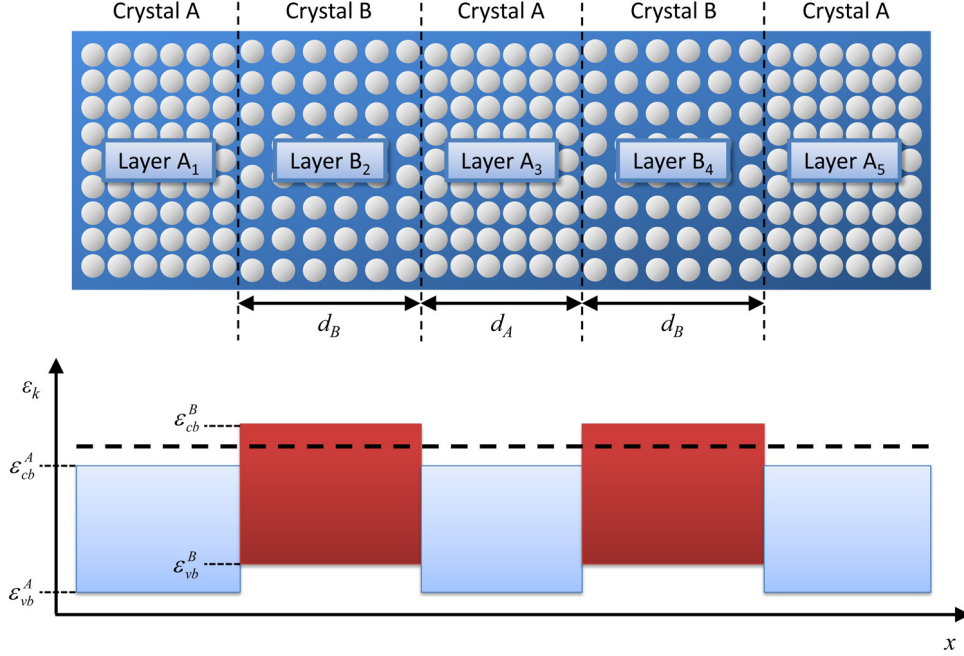
Figure 2-1: (a) Schematic diagram of the single PQW heterostructure. Two layers of photonic crystal B are embedded within a host photonic crystal A. (b) Photonic band structure of the PQW heterostructure, where the shaded regions correspond to photonic band gaps. The "conduction band edge" and "valence band edge" energies (ε_{cb}^i and ε_{vb}^i, respectively, where $i = A$ or B) of photonic crystals A and B are indicated. A photonic well is formed within the central layer of photonic crystal A. The dashed horizontal line corresponds to the energy level of a possible resonant state.

$k_2 = k_4 = K_B$.

The transmission coefficient for TE plane waves propagating along the x-direction is calculated using the transfer matrix method, which relates the incident and reflected electric field amplitudes in each photonic crystal layer of the heterostructure through a transfer matrix equation. The transfer matrix is obtained by using the continuity conditions for the electric field and its first derivative at the interfaces between adjacent photonic crystal layers in the PQW heterostructure [24, 25], which gives

$$E_j(x_j) = E_{j+1}(x_j) \tag{2.2}$$

21

and

$$\left[\frac{\partial E_j(x)}{\partial x}\right]_{x=x_j} = \left[\frac{\partial E_{j+1}(x)}{\partial x}\right]_{x=x_j}. \tag{2.3}$$

In the above expressions, x_j is the coordinate of the jth photonic crystal interface along the x-axis, and hence the index j runs from 1 to 4 (i.e., there are four interfaces between photonic crystal layers in the PQW heterostructure).

Using Eqs. 2.2 and 2.3, it is found that the electric field amplitudes in the outer layers A_1 and A_5 are related via the transfer matrix equation

$$\begin{pmatrix} \alpha_1 \\ \beta_1 \end{pmatrix} = M_{PQW} \begin{pmatrix} \alpha_5 \\ \beta_5 \end{pmatrix}, \tag{2.4}$$

where

$$M_{PQW} = M_{12} M_{23} M_{34} M_{45}. \tag{2.5}$$

In the above expression, M_{PQW} is the transfer matrix for the entire PQW heterostructure relating the incident and reflected electric field amplitudes in layer A_1 to those in layer A_5, while $M_{j,j+1}$ are the transfer matrices relating the incident and reflected electric field amplitudes between adjacent layers j and $j+1$. The transfer matrix at the jth interface is given as [25]

$$M_{j,j+1} = \frac{1}{2k_j} \begin{pmatrix} (k_j + k_{j+1}) \exp\left[i\left(-k_j + k_{j+1}\right) x_j\right] & (k_j - k_{j+1}) \exp\left[i\left(-k_j - k_{j+1}\right) x_j\right] \\ (k_j - k_{j+1}) \exp\left[i\left(k_j + k_{j+1}\right) x_j\right] & (k_j + k_{j+1}) \exp\left[i\left(k_j - k_{j+1}\right) x_j\right] \end{pmatrix}. \tag{2.6}$$

The transmission coefficient for the PQW T_{PQW} is defined as the ratio of the transmitted electric field to the incident electric field, and can be obtained from the $(1,1)$ entry of the total transfer matrix M_{PQW} as [5, 25]

$$T_{PQW} = \left|\frac{\alpha_5}{\alpha_1}\right| = \left|\frac{1}{[M_{PQW}]_{11}}\right|^2 \tag{2.7}$$

The resulting expression for T_{PQW} depends on the wave vectors K_i in each of the regions of the PQW heterostructure, which in turn depend on the photon energy ε_k through the photonic dispersion relation for a given region.

Here it is considered that the component photonic crystals in the PQW heterostructure each

consist of dielectric spheres with refractive index n_{1i} and radius a_i embedded in a dielectric background medium with refractive index n_{2i}, where the subscripts $i = A$ or B denote the photonic well or barrier, respectively. The dielectric spheres in photonic crystals A and B are arranged periodically in three dimensions with lattice constants L_A and L_B, respectively. The dispersion relations for photonic crystals A and B are obtained by using the photonic crystal band structure model proposed by John and Wang [26], where it is assumed that each crystal possesses a three-dimensional photonic band gap that is equal for all propagation directions. This assumption provides a simplified model that exhibits many of the observed qualitative features of three-dimensional photonic crystals [27]. In this model, the propagation of an electromagnetic wave in a photonic crystal can be described by the scalar Maxwell wave equation as

$$\nabla^2 E = -n^2(r)\frac{\omega^2}{c^2}E, \tag{2.8}$$

where the periodically-varying refractive index function $n(r)$ satisfies

$$n(r) = n(r + L), \tag{2.9}$$

L being the lattice constant of the photonic crystal. From Bloch's theorem for a wave propagating in a periodic structure, the solutions to the scalar Maxwell wave equation satisfy

$$E(r + L) = E(r)e^{iKL}, \tag{2.10}$$

where K is the Bloch wave vector. Using the electromagnetic boundary conditions within a photonic crystal's unit cell and applying Bloch's theorem, the dispersion relations for photonic crystals A and B are obtained as

$$\cos\left(K_i L_i\right) = \sum_{\pm} \pm \frac{(n_{1i} \pm n_{2i})^2}{4n_{1i}n_{2i}} \cos\left\{\frac{\varepsilon_k}{\hbar c}\left[2n_{1i}a_i \pm n_{2i}\left(L_i - 2a_i\right)\right]\right\}, \ i = A \text{ or } B \tag{2.11}$$

For a given set of photonic crystal parameters n_{1i}, n_{2i}, a_i, and L_i, the above expression leads to a photonic band gap in the photonic dispersion relation for energies $\varepsilon_{vb}^i < \varepsilon_k < \varepsilon_{cb}^i$, where ε_{vb}^i and ε_{cb}^i are the lower (i.e., "valence band") and upper (i.e., "conduction band") energies at which the photonic band gap appears. To form a PQW, parameters are chosen for photonic

23
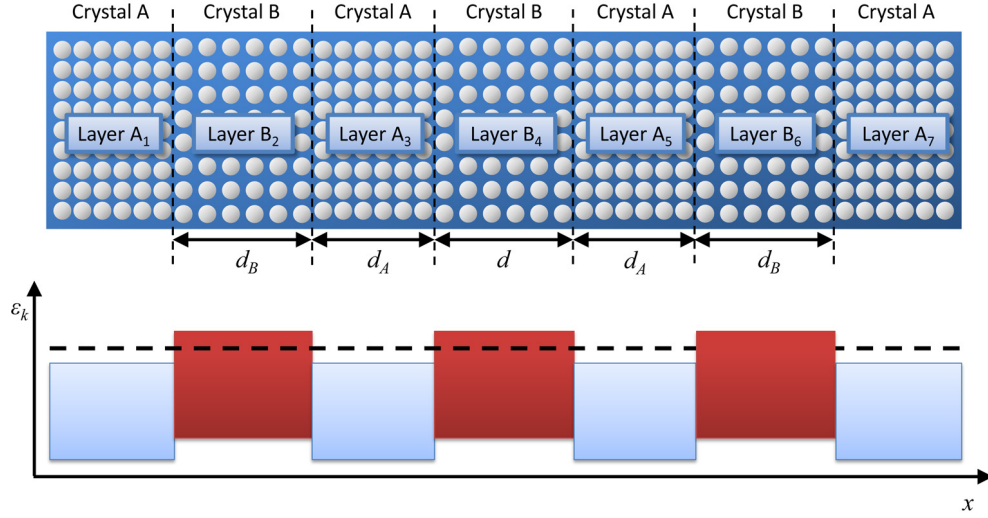
Figure 2-2: (above) Schematic diagram of the double photonic quantum well heterostructure. Three layers of photonic crystal B are embedded within a host photonic crystal A. (below) Photonic band structure of the double photonic quantum well heterostructure, where the shaded regions correspond to photonic band gaps. Two photonic wells are formed within the central layer of photonic crystal A. The dashed horizontal line corresponds to the energy level of a possible resonant state.

crystals A and B such that the condition $\varepsilon_{vb}^B < \varepsilon_{cb}^A < \varepsilon_{cb}^B$ is satisfied.

A DPQW heterostructure can be formed by adding another photonic well and photonic barrier to the system. In this case the heterostructure is denoted as $A_1/B_2/A_3/B_4/A_5/B_6/A_7$, as illustrated in Figure 2-2. The transmission coefficient for the DPQW heterostructure is obtained as

$$T_{DPQW} = \left| \frac{1}{[M_{DPQW}]_{11}} \right|^2, \tag{2.12}$$

where

$$M_{DPQW} = \prod_{j=1}^{6} M_{j,j+1} \tag{2.13}$$

and the wave vectors used in the matrices $M_{j,j+1}$ are $k_1 = k_3 = k_5 = k_7 = K_A$ and $k_2 = k_4 = k_6 = K_B$. In the following section, numerical simulations for the transmission coefficient of both PQW and DPQW heterostructures are performed.

24
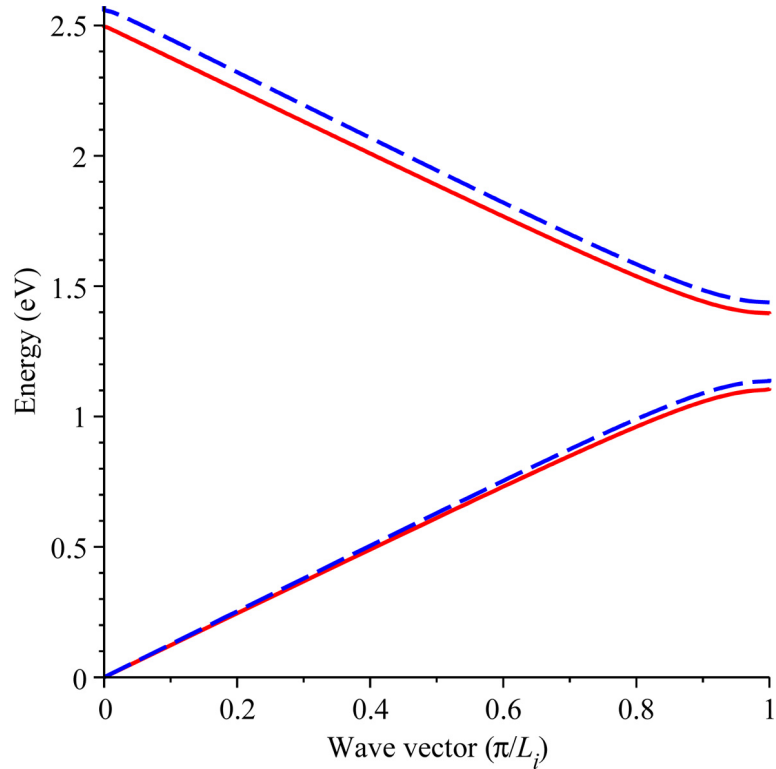
Figure 2-3: Reduced band diagram for photonic crystal A (solid curve) and B (dashed curve).

2.3 Results and Discussion

It is considered that photonic crystals A and B each consist of a silica background material $(n_{1A} = n_{1B} = 1.45)$ embedded with air spheres $(n_{2A} = n_{2B} = 1)$. The radii of the air spheres in each crystal are taken as $a_A = a_B = 125$ nm, and the lattice constants of the two crystals are taken as $L_A = 420$ nm and $L_B = 410$ nm. Using Eq. 2.11, the photonic dispersion relations are plotted in Figure 2-3. The lower "valence" and upper "conduction" photonic band edges of photonic crystal A were calculated as $\varepsilon_{vb}^A = 1.1026$ eV and $\varepsilon_{cb}^A = 1.3965$ eV, respectively, while the lower "valence" and upper "conduction" photonic band edges of photonic crystal B were calculated as $\varepsilon_{vb}^B = 1.1360$ eV and $\varepsilon_{cb}^B = 1.4382$ eV, respectively. Note that the condition $\varepsilon_{vb}^B < \varepsilon_{cb}^A < \varepsilon_{cb}^B$ is satisfied, and so a PQW can be formed using these photonic crystals.

The single PQW heterostructure is denoted in terms of the constituent photonic crystal layers as $A_1/B_2/A_3/B_4/A_5$. The thicknesses of the outer photonic barrier layers B_2 and B_4
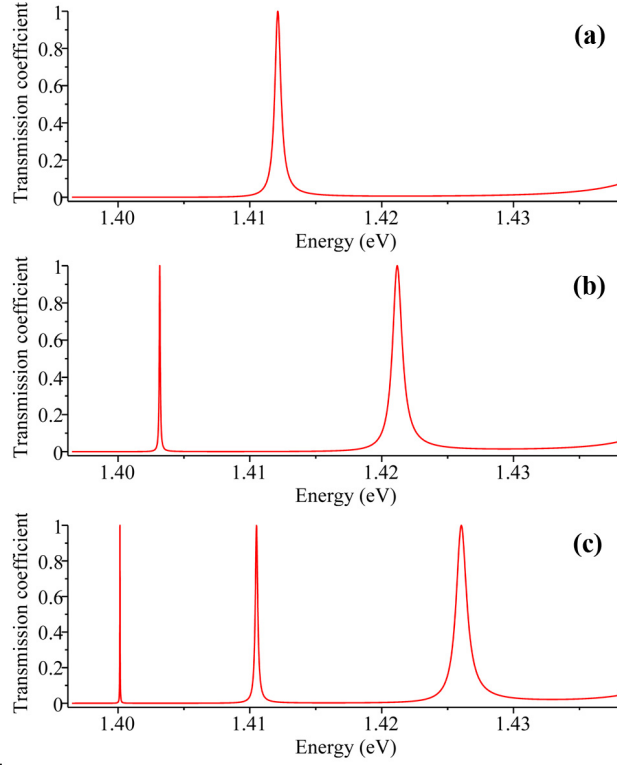
Figure 2-4: Photon transmission coefficient for a PQW heterostructure versus incident photon energy. Here the width of the photonic barriers is $d_B = 10L_B$ and the photonic well width is taken as (a) $d_A = 10L_A$, (b) $d_A = 20L_A$, and (c) $d_A = 30L_A$.

is denoted by d_B and the width of the central photonic well layer is given by d_A (see Figure 2-1). The transmission coefficient of a PQW heterostructure is plotted in Figure 2-4 for photon energies ε_k within the photonic well such that $\varepsilon_{cb}^A < \varepsilon_k < \varepsilon_{cb}^B$. Here the width of the photonic barriers is taken as $d_B = 10L_B$ while the width of the photonic well is varied. The transmission spectra shown in Figure 2-4 show pronounced peaks for which perfect photon transmission may occur through the heterostructure. These peaks correspond to the resonant quasi-bound states of the PQW heterostructure, for which a photon tunnels through a layer of crystal B and occupies a bound state within crystal A before tunnelling out again [5]. Note that as the photonic well width is increased, the number of resonant tunnelling states also increases [12-14]. Similar behaviour is also observed for electronic quantum well heterostructures [5].

In Figure 2-5 a two-dimensional plot of the transmission coefficient of the PQW heterostruc-
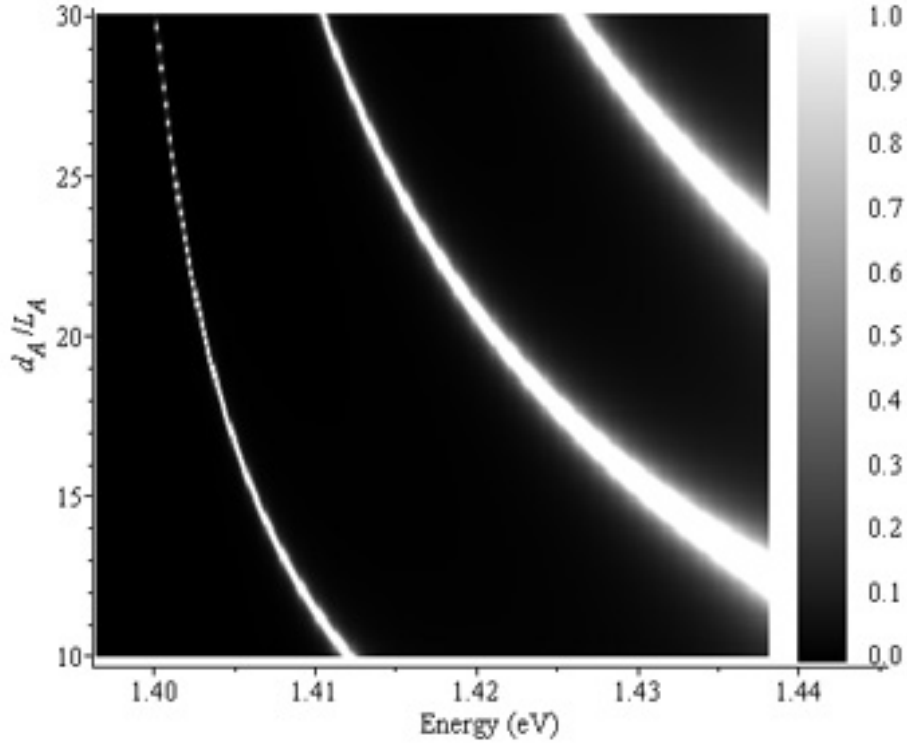
Figure 2-5: Two-dimensional plot of the transmission coefficient for the PQW heterostructure. The incident photon energy ε_k is given along the horizontal axis while the width of the photonic well d_A is given along the vertical axis. Other parameters are the same as those used in Figure 2-4.

ture is presented for which the photon energy is varied along the horizontal axis and the width of the photonic well is increased along the vertical axis. The two-dimensional plot can be used to determine the width of the photonic well necessary to support a particular number of resonant states, or to determine the energy of a resonant state as a function of the photonic well width. Note that the actual width of a fabricated PQW should be an integer number of lattice constants L_A.

Thus far, the transmission spectra for single PQW heterostructures have been investigated. In the following numerical simulations, DPQW heterostructures are addressed by considering additional layers of photonic crystals A and B so that the total heterostructure is denoted as $A_1/B_2/A_3/B_4/A_5/B_6/A_7$. For the DPQW heterostructure, the parameter d_B corresponds to the thicknesses of the outer photonic barrier layers B_2 and B_6, the parameter d_A denotes the
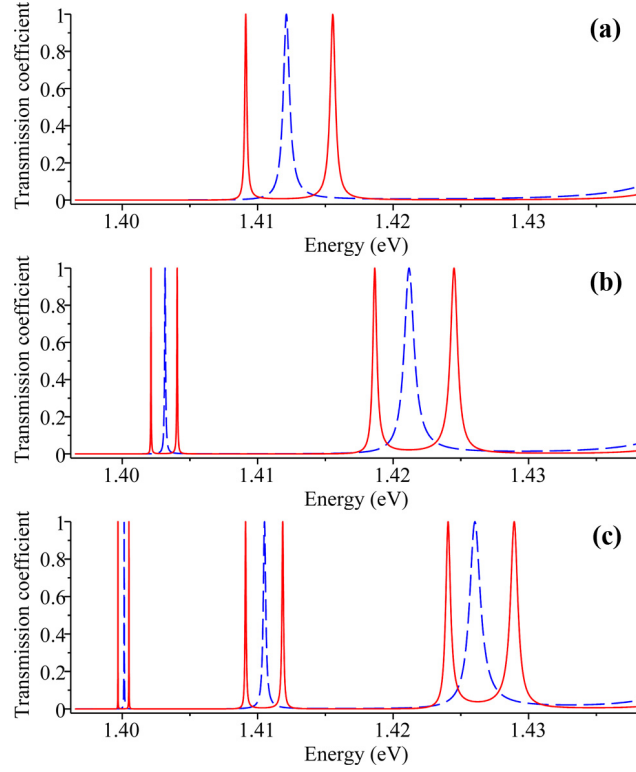
Figure 2-6: Transmission coefficient for the DPQW (solid curves) versus incident photon energy ε_k. Here the outer photonic barrier widths are $d_B = 10L_B$ while the central photonic barrier width is $d = 5L_B$. The photonic well widths are varied as (a) $d_A = 10L_A$, (b) $d_A = 20L_A$, and (c) $d_A = 30L_A$. The dashed curves correspond to the transmission coefficients of single PQWs with the same d_A and d_B.

width of the photonic well layers A_3 and A_5 and the parameter d represents the width of the central photonic barrier B_4 (see Figure 2-2).

The transmission spectra of a DPQW heterostructure as well as those of an equivalent single PQW heterostructure are presented in Figure 2-6 while varying the photonic well width d_A. In these spectra, resonant tunnelling states occur as single peaks for the PQW and as split pairs of peaks for the DPQW heterostructure. Note that the split pairs of resonant peaks in the DPQW heterostructure are centered on the single peaks from the single PQW heterostructure. This illustrates the origin of the spectral splitting that occurs in the DPQW heterostructure, as each isolated PQW would contain single, degenerate bound states. However, since the thickness of the central photonic barrier is small, the electromagnetic fields of these degenerate states
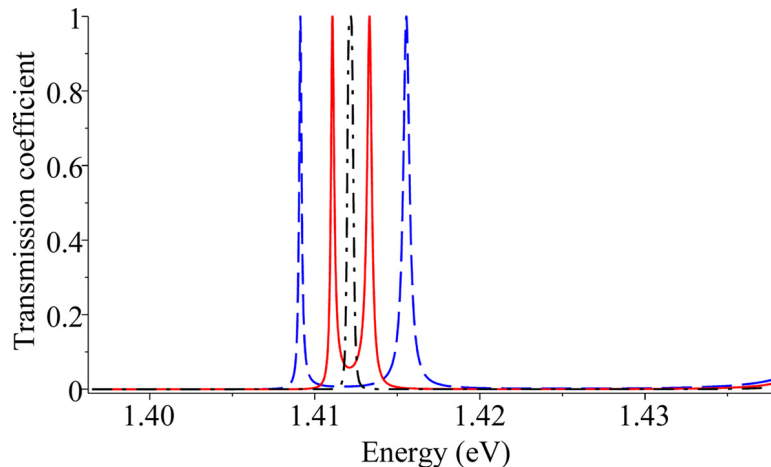
Figure 2-7: Transmission spectra from a DPQW heterostructure where the inter-well separation is $d = 5L_B$ (solid curve), $10L_B$ (dashed curve) and $20L_B$ (dash-dotted curve). The photonic well widths are $d_A = 10L_A$ and the outer photonic barrier widths are $d_B = 10L_B$.

overlap with one another, causing the bound states to split into symmetric and antisymmetric pairs [19]. From Figure 2-6, it is observed that varying the thickness of the photonic wells in the DPQW heterostructure causes the number of bound state pairs to change, as was observed for the single bound states in the PQW. It is also found that the energy-splitting effect is stronger for the degenerate states with higher energies. This is due to a larger electric field overlap between bound photonic states at higher energies [19].

Transmission spectra for the DPQW heterostructure are presented in Figure 2-7 while varying only the inter-well separation d. Here it is found that as the inter-well separation is increased, the energy splitting of the resonant peaks in the transmission spectrum decreases. This finding can be explained in terms of the coupling strength between the degenerate bound states in the two PQWs. When the photonic wells are close to one another (or equivalently when the width of the central photonic barrier is small), the overlap between the electromagnetic fields of the degenerate bound states is stronger. This leads to a greater amount of energy splitting for the degenerate bound states. On the other hand, when the photonic wells are far away from one another, the coupling between the degenerate bound states is weak and the energy splitting effect decreases. For a great enough inter-well separation, the splitting of the degenerate states cannot be resolved. At this point the transmission spectrum of the DPQW heterostructure ap-

29
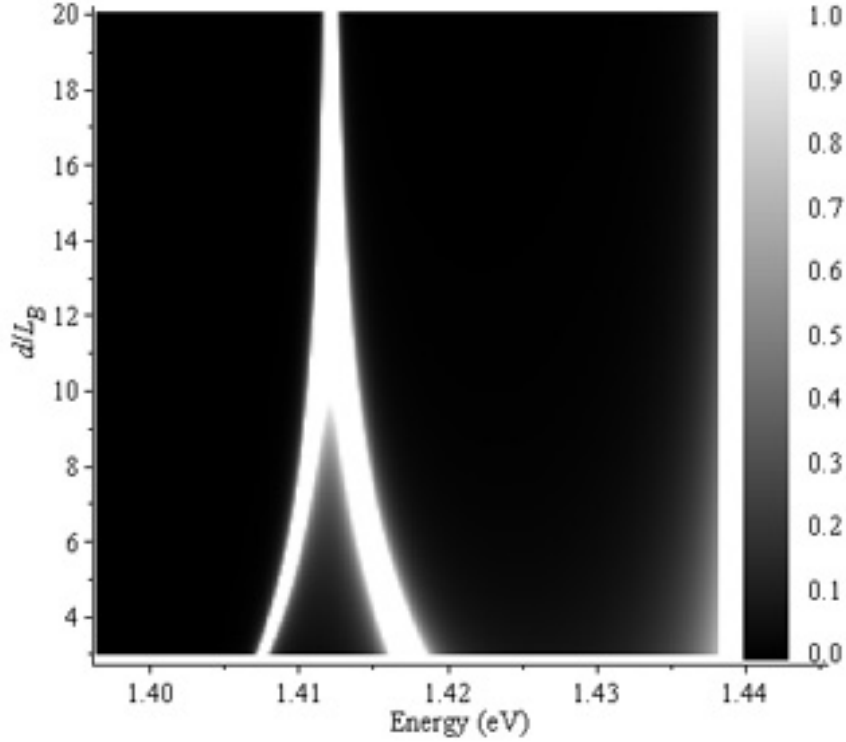
Figure 2-8: Two-dimensional plot of the transmission coefficient for the double photonic quantum well heterostructure. The incident photon energy ε_k is given along the horizontal axis while the width of the central photonic barrier d is given along the vertical axis. Other parameters are the same as those used in Figure 2-7.

proaches that of an equivalent single PQW, and the bound photons can be regarded as confined to identical but separate and isolated wells [22].

In Figure 2-8 a two-dimensional plot of the transmission coefficient for the DPQW heterostructure is presented. Here the horizontal axis indicates the photon energy while the value of the inter-well separation d is given along the vertical axis. This result illustrates how the spectral splitting of the resonant tunnelling states in the DPQW can be finely tuned by varying the width of the photonic barrier separating the wells.

Finally, the effect of the thicknesses of the outer photonic barriers is investigated in Figure 2-9, where the transmission coefficient of the DPQW heterostructure is plotted for different values of d_B. For the transmission spectra presented in this chapter, there is some degree of spectral broadening associated with each resonant peak. This broadening is attributed to the finite
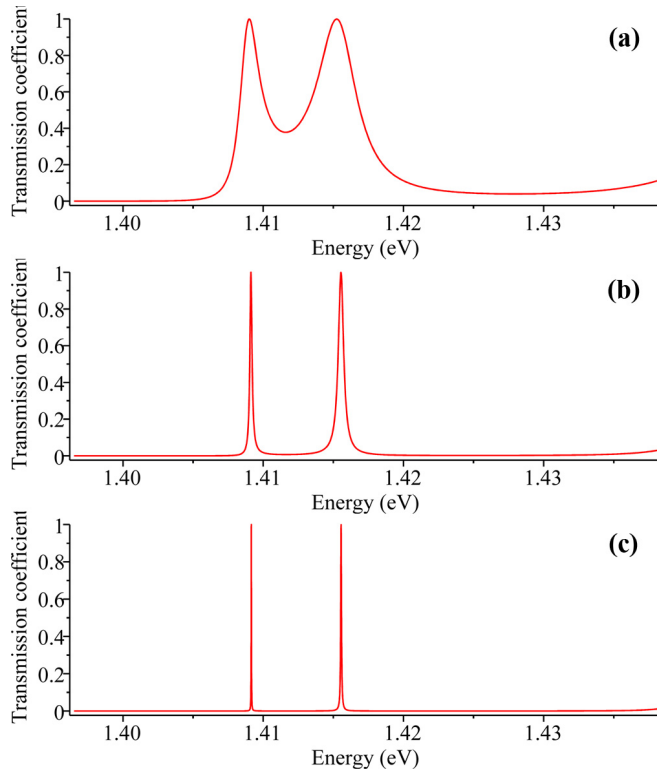
Figure 2-9: Transmission spectra for the DPQW heterostructure where the outer photonic barrier widths are (a) $d_B = 5L_B$, (b) $d_B = 10L_B$, and (c) $d_B = 15L_B$. Here the photonic well width is $d_A = 10L_A$ and the central photonic barrier width is $d = 5L_B$.

widths of the photonic barriers [17], and results in a lower quality factor for the transmitted resonant states. Figure 2-9 shows that by changing the width of the outer photonic barriers, the spectral broadening of the resonant tunnelling peaks can be increased or decreased. The spectra broadening is associated with the lifetime of a resonant photon which is contained within the photonic quantum wells. This is because the energy of a bound state confined between photonic barriers with finite widths is not precisely defined, but instead has a linewidth $\hbar/\tau$, where τ is the lifetime of a photon in the photonic well [5]. By increasing the thickness of the photonic barriers, the photon remains trapped for a longer period of time before it escapes by tunnelling through the barriers.

The increased spectral broadening of the resonant tunnelling peaks at higher energies can also be explained in terms of the lifetime of a confined photon. Photons with higher energies

have a higher probability of tunnelling through the photonic barriers, and so they escape the photonic wells more quickly than photons with lower energies. It is found that if the thickness of the outer photonic barriers d_B becomes too large, the transmission coefficient is zero for the range of energies between ε_{cb}^A and ε_{cb}^B. In this situation, an incident photon cannot penetrate the outer photonic barrier because it is too wide.

2.4 Conclusions

In this chapter, photon transmission for both single PQW and DPQW heterostructures has been investigated using the transfer matrix method. For the PQW heterostructure, numerical simulations of the transmission coefficient reveal that resonant photon tunnelling states appear as discrete, sharp peaks in the transmission spectra along the confinement direction of the structure. The number of resonant tunnelling states can be controlled by changing the width of the photonic well.

In the DPQW heterostructure, resonant tunnelling states appear in the transmission spectra as split pairs, where the spectral splitting is centered on the energy corresponding to the resonant states in the degenerate single PQWs within the heterostructure. The energy splitting is attributed to the coupling of the degenerate states within each of the single PQWs through the photonic barrier separating them. When the width of the separating barrier is small, the electric fields for the degenerate states overlap one another in each of the photonic wells, which leads to the coupling effect and spectral splitting. By varying the thickness of the barrier separating the photonic wells, the spectral splitting can be controlled. The energy-splitting phenomenon described here is in qualitative agreement with reported experimental results for a DPQW heterostructure consisting of one-dimensional photonic crystals [19]. It is anticipated that the resonant tunnelling phenomenon described here can be used to develop photonic switching devices, high-quality optical filters and other optoelectronic devices [4, 10-23].

Bibliography

[1] E. Yablonovitch, *Phys. Rev. Lett.* **58**, 2059 (1987).

[2] S. John, *Phys. Rev. Lett.* **58**, 2486 (1987).

[3] J. D. Joannopoulos, S. G. Johnson, J. N. Winn, and R. D. Meade, *Photonic Crystals: Molding the Flow of Light*, 2nd ed. (Princeton University Press, Princeton, New Jersey, 2008).

[4] E. Istrate and E. H. Sargent, *Rev. Mod. Phys.* **78**, 455 (2006).

[5] J. H. Davies, The Physics of Low-Dimensional Semiconductors: An Introduction

[6] B. S. Song, S. Noda, T. Asano, and Y. Akahane, *Nat. Mater.* **4**, 207 (2005).

[7] S. Noda, M. Fujita, and T. Asano, *Nat. Photon.* **1**, 449 (2007).

[8] S. Y. Lin, E. Chow, S. G. Johnson, and J. D. Joannopoulos, *Opt. Lett.* **25**, 1297 (2000).

[9] H. Takano, B. S. Song, T. Asano, and S. Noda, *Opt. Expr.* **14**, 3491 (2006).

[10] S. Y. Lin and G. Arjavalingam, *J. Opt. Soc. Am. B* **11**, 2124 (1994).

[11] S. Y. Lin, V. M. Hietala, S. K. Lyo, and A. Zaslavsky, *Appl. Phys. Lett.* **68**, 3233 (1996).

[12] J. Zi, J. Wan, and C. Zhang, *Appl. Phys. Lett.* **73**, 2084 (1998).

[13] F. Qiao, C. Zhang, J. Wan, and J. Zi, *Appl. Phys. Lett.* **77**, 3698 (2000).

[14] Y. Jiang, C. Niu and D. L. Lin, *Phys. Rev. B* **59**, 9981 (1999).

[15] H. M. Fei, Y. Jiang, J. Q. Liang, and D. L. Lin, *J. Phys. B* **42**, 055401 (2009).

[16] S. Yano, Y. Segawa, J. S. Bae, K. Mizuno, H. Miyazaki, K. Ohtaka, and S. Yamaguchi, *Phys. Rev. B* **63**, 153316 (2001).

[17] X. Chen, W. Lu, and S. C. Shen, *Solid State Commun.* **127**, 541 (2003).

[18] S. H. Xu, Z. H. Xiong, L. L. Gu, Y. Liu, X. M. Ding, J. Zi, and X. Y. Hou, *Solid State Commun.* **126**, 125 (2003).

[19] S. H. Xu, X. M. Ding, Z. H. Xiong, Y. Liu, Y. Liu, Z. J. Wang, J. Zi, and X. Y. Hou, *Photonics Nanostruct. Fundam. Appl.* **4**, 17 (2006).

[20] C. S. Feng, L.-M. Mei, L. Z. Cai, P. Li, and X. L. Yang, *Solid State Commun.* **135**, 330 (2005).

[21] R. Liu and B. Gai, *J. Opt. Soc. Am. B* **24**, 2369 (2007).

[22] J. Liu, J. Sun, C. Huang, W. Hu, and M. Chen, *IET Optoelectron.* **2**, 122 (2008).

[23] S. M. Sadeghi and W. Li, *Phys. Rev. B* **81**, 155317 (2010).

[24] A. Yariv and P. Yeh, *Photonics: Optical Electronics in Modern Communications* (Oxford University Press, New York, 2007).

[25] H. Yamamoto, *Appl. Phys. A* **42**, 245 (1987).

[26] S. John and J. Wang, Phys. Rev. B 43, 12772 (1991).

[27] P. Lambropoulos, G. M. Nikolopoulos, T. R. Nielsen, and S. Bay, *Rep. Prog. Phys.* **63**, 455 (2000).

Chapter 3

Photonic States in a Nonlinear Photonic Crystal Waveguide Heterostructure

In the previous chapter, resonant photonic tunnelling in photonic quantum well (PQW) heterostructures was investigated. PQWs were formed by embedding one type of photonic crystal within another photonic crystal, resulting in a photonic band structure that confines photons along one direction. This type of photonic band gap engineering relies on the photonic band gaps of the constituent photonic crystals within the heterostructure. In turn, the photonic band gaps in these photonic crystals depend on the lattice spacings and sizes of the constituent dielectric materials, as well as their refractive indices [1-3]. For PQW heterostructure device applications, the ability to dynamically alter the photonic band structure of the PQW(s) is highly desirable. In this chapter, practical switching mechanisms in a double photonic quantum well (DPQW) heterostructure are investigated[1]. These switching mechanisms rely on optical modification of the refractive index of the constituent dielectric materials in a photonic crystal, or physical modification of a photonic crystal's geometry.

---

[1]The material presented in this chapter has been published in: J. D. Cox and M. R. Singh, *J. Appl. Phys.* **108**, 083102 (2010).

3.1 Introduction

Recently, considerable effort has been placed into finding classes of materials that can be used to make smaller and faster optoelectronic devices. Towards this end, photonic crystals [1-3] and their heterostructures have been widely studied due to their ability to localize light and control its propagation in a manner analogous to a semiconductor material's control of electrons. Photonic crystals are artifical nanomaterials possessing a dielectric constant that varies periodically in one, two, or three spatial dimensions, due to which a photonic band gap forms in the structure's photonic dispersion relation [3]. The photonic band gap is a range of energies of light which are completely reflected by the periodic dielectric structure, and are thus prohibited from propagating through the photonic crystal. Due to this phenomenon, photonic crystals have been intensively studied for the purpose of developing ultrafast and efficient nanophotonic devices.

Here the bound states of a nonlinear double photonic waveguide heterostructure are investigated, where the heterostructure is formed by combining two identical PQWs. The double photonic waveguide heterostructure can also be referred to as a double photonic quantum well (DPQW) heterostructure, and in this chapter these terms will be used interchangeably. PQWs are a class of photonic crystal device which have been widely studied, and have many applications such as waveguides, high-quality filters, and as components of photonic integrated circuits [4-17]. They are formed by imbedding a photonic well between photonic barriers, where the well and barrier materials are chosen so that for a range of frequencies, photon propagation is permitted within the well but not the barriers. Photonic barriers are thus photonic crystals with photonic band gaps that may be regarded as potential barriers for photons, while the photonic well may consist of either a uniform dielectric material or a different photonic crystal. The overall photonic band structure of a PQW heterostructure causes photons to become confined within the well and occupy quantized states along one direction. This effect has been demonstrated in both theoretical and experimental studies, where it has been shown that incident light with an energy corresponding to one of the confined states of a PQW undergoes perfect transmission through the structure due to the resonant tunnelling effect, provided that the photonic barriers are thin enough to allow photon tunnelling to occur [4-17].

In addition to single PQW heterostructures but to a lesser extent, multiple photonic quan-

tum well heterostructures formed by combining two or more PQWs into a single structure have been investigated [9, 13, 15-17]. In these studies, the coupling of individual PQWs along the photonic confinement direction has been observed. Xu et al. [13], for example, fabricated a double photonic quantum well (DPQW) heterostructure from one-dimensional photonic crystals made from multilayered refractive-index-modulated porous silicon. From the measured transmission spectra of the system, they found that bound states of the DPQW heterostructure underwent a twofold energy splitting, where the separation between split states increased as the distance between the two PQWs was decreased. This inter-well coupling effect in multiple PQW heterostructures occurs when the PQWs in the structure are identical, so that in each photonic well the bound states are degenerate. When the distance between the wells is decreased, the degenerate states interact and undergo an N-fold splitting, where N is the number of photonic wells in the heterostructure [9, 15, 16]. Recently, Sadeghi and Li [17] proposed a type of DPQW system induced in a photonic superstructure made up of an array of semiconductor quantum wells. By applying laser light to specific regions of the photonic superstructure, two photonic quantum wells were formed due to the change in the effective refractive index in those areas. In their study, it was also shown that the bound photonic states in the laser-induced double photonic quantum well system underwent a twofold splitting into symmetric (bonding) and anti-symmetric (anti-bonding) pairs.

The double photonic waveguide system considered here is in essence a DPQW heterostructure composed of two types of photonic crystals, which are denoted as A and B. Crystals A and B are each composed of dielectric spheres embedded in a dielectric background material. It is considered that the dielectric spheres of crystal A are made from a material with a high Kerr nonlinearity, so that their refractive index can be changed upon application of an intense pulsed laser field (pump field). Nonlinear photonic crystals are ideal candidates for developing ultrafast all-optical switching devices, and thus have been widely studied in the literature [18-25]. In the present study, it is considered that the dielectric spheres in photonic crystal A are composed of polystyrene, following a recent experimental demonstration by Liu et al. [18] of ultrafast all-optical switching in a three-dimensional polystyrene photonic crystal. On the other hand, the dielectric spheres in photonic crystal B are made of silica, which has a negligible Kerr nonlinearity compared to that of polystyrene, and so their refractive index remains unaffected
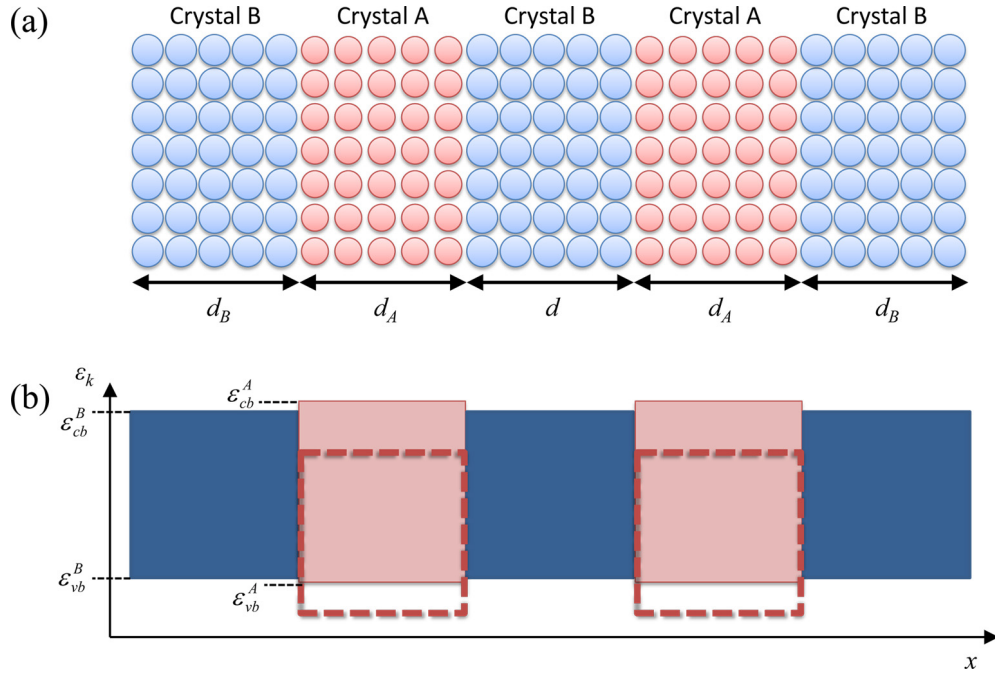
Figure 3-1: (a) Schematic representation of the nonlinear double photonic waveguide heterostructure. Photonic crystals A and B each consist of periodically-arranged dielectric spheres, and are arranged in the sequence B/A/B/A/B along the x-direction. The differently sized and shaded circles represent the different types of dielectric spheres in each photonic crystal. The thicknesses of each photonic crystal layer are indicated just below the diagram. (b) Photonic band diagram of the double photonic waveguide heterostructure corresponding to the schematic diagram in (a). The differently-shaded regions indicate the photonic band gaps of the different photonic crystals. The dashed boxes indicate a new location for the photonic band gap of photonic crystals A when an external pump laser field is applied.

by the pump field. Parameters for photonic crystals A and B are chosen so that in the absence of the pump laser, the upper edges of their photonic band gaps are very near one another. To form the DPQW heterostructure, these crystals are arranged in the sequence B/A/B/A/B along one direction, as shown in Figure 3-1(a). When the pump field is applied to the system, the photonic band gap of photonic crystal A shifts in such a way that two photonic quantum wells are induced in crystals A, thus forming the double waveguide heterostructure (see Figure 3-1(b)).

The effect of stress or strain fields applied to photonic crystal B is also investigated in this chapter. To incorporate the effect of an applied stress or strain field, it is considered that

38

the application of such a field causes the radii of the silica spheres in photonic crystal B and their spacing to change slightly. In absence of the stress or strain field, the upper edges of the photonic band gaps of crystals A and B are almost identical, so that there are essentially no photonic wells in the structure. Here it is shown that the deformation of photonic crystal B due to an applied stress field can raise the upper edge of photonic crystal B's photonic band gap (i.e., increase the height of the photonic barriers), thereby inducing photonic waveguides in the heterostructure.

Using the transfer matrix method [26, 27], transcendental equations which give the energy levels of the induced bound states of the system are obtained. By using a Taylor series expansion, analytical expressions for the energy splitting of these states are derived. The transmission spectra for the double photonic waveguide heterostructure are simulated using code developed in MAPLE, from which the resonant tunnelling peaks corresponding to the bound states of the system are found. The energy splitting of the resonant tunnelling peaks is then compared with the analytical expressions obtained for the energy splitting.

In the absence of any external fields (pump laser or stress/strain), the upper photonic band edges of photonic crystals A and B have nearly the same value, and it is found that there are no bound states supported by the system. Here, the depth of the photonic wells can be increased by applying a sufficiently intense external field, allowing one or more bound states to appear when the photonic wells become sufficiently deep. It is shown that the system may be switched from zero to one or more bound photonic states by changing the intensity of the pump laser field or by applying a sufficiently intense stress or strain field to photonic crystals B.

In the present study, the bound photonic states in the double photonic waveguide system are shown to split into symmetric and anti-symmetric pairs when the two photonic wells are in close proximity. This splitting effect is due to the inter-well coupling between the degenerate states in each of the two identical PQWs of the system [9, 13, 15-17]. It is predicted that the energy splitting of a bound state decreases exponentially with increasing distance between the two PQWs. For a bound state in the laser-induced photonic wells, it is found that the energy splitting decreases as the intensity of the pump field increases. From the theoretical calculations and simulated transmission spectra of the system it is shown that the number of resonant states, their energy levels and degree of splitting all depend on the intensity of the

pump field. Furthermore, the results from the analytical expressions of the energy splitting have been shown to agree with those observed from the simulated transmission spectra. Within the range of pump field intensities considered in these simulations, it is found that the laser-induced double waveguide system may be optically switched from zero to one or two pairs of bound states. It is anticipated that the results presented here can be used to develop all-optical switching devices, tunable filters and coupled waveguides.

3.2   Theoretical Formalism

The double photonic waveguide heterostructure is formed using two photonic crystals A (photonic well) and B (photonic barrier), which are arranged in the sequence B/A/B/A/B along the x-axis as shown in Figure 3-1. The thicknesses of the outer photonic barrier layers and the photonic well layers are denoted by d_B and d_A, respectively, while the thickness of the central photonic barrier layer is denoted as d. Photonic crystals A and B are each composed of dielectric spheres embedded in a dielectric background material. It is considered that each crystal shares the same background dielectric material, which has refractive index n. The dielectric spheres in crystal A (B) have radii denoted as r_A (r_B), and refractive index n_A (n_B). Lattice constants of photonic crystals A and B are denoted by L_A and L_B, respectively.

The spheres in photonic crystal A consist of a nonlinear dielectric material, such that their refractive index in the presence of a strong laser field is given as [25, 28]

$$n_A = n_0 + n_{nL}I_p, \tag{3.1}$$

where n_0 is the weak-field refractive index, n_{nL} is the third-order nonlinearity susceptibility, which can be positive or negative depending on the dielectric material, and I_p is the laser (pump) field intensity. Here the effect of the pump laser field on the bound states in the double waveguide system is investigated. Note that in the following simulations, the refractive indices of the background dielectric (n) and dielectric spheres in photonic crystal B (n_B) have a significantly weaker nonlinear optical response, and so remain unaffected by the pump laser field.

Transverse electric, linearly polarized electromagnetic waves travelling in the x-direction

propagate in the form of Bloch waves in photonic crystals A and B due to their periodic, spatially-modulating dielectric constants. Here K_A and K_B denote the components of the Bloch waves propagating along the x-direction in crystals A and B, respectively. Using the continuity conditions for a propagating electromagnetic wave at the interfaces between photonic crystals A and B in the heterostructure, the following expressions were derived for the energies of the bound photons within the double waveguide structure. The energy levels of the mth ($m = 0$, 1, 2, ...) symmetric and anti-symmetric bound states are denoted as ε_m^+ and ε_m^-, respectively, and are obtained from

$$\frac{K_B\left(\varepsilon_m^\pm\right)}{K_A\left(\varepsilon_m^\pm\right)}\Omega_\pm = \tan\left\{K_A\left(\varepsilon_m^\pm\right)d_A + m\pi - \arctan\left[\frac{K_B\left(\varepsilon_m^\pm\right)}{K_A\left(\varepsilon_m^\pm\right)}\right]\right\}, \qquad (3.2)$$

where

$$\Omega_+ = \tanh\left[\frac{1}{2}K_B\left(\varepsilon_m^+\right)d\right] \qquad (3.3)$$

$$\Omega_- = \coth\left[\frac{1}{2}K_B\left(\varepsilon_m^-\right)d\right].$$

Expressions for the Bloch wave vectors K_A and K_B in photonic crystals A and B are obtained using the band structure model proposed by John and Wang [29], which has been widely used to model the optical properties of photonic crystals [25, 27, 29-31]. From this model, the Bloch wave vectors in photonic crystals A and B along the x-direction are given by

$$K_A\left(\varepsilon_k\right) = \sqrt{F_A^2\left(\varepsilon_k\right) - K_\perp^2} \qquad (3.4)$$

$$K_B\left(\varepsilon_k\right) = \sqrt{K_\perp^2 - F_B^2\left(\varepsilon_k\right)},$$

where ε_k is the photon energy, $K_\perp$ is the component of the Bloch wave vector perpendicular to the x-direction and

$$F_i\left(\varepsilon_k\right) = \frac{1}{L_i}\arccos\left[\sum_\pm \pm\frac{\left(n_i \pm n\right)^2}{4n_in}\cos\left\{\frac{\varepsilon_k}{\hbar c}\left[2n_ir_i \pm n\left(L_i - 2r_i\right)\right]\right\}\right], \quad i = A \text{ or } B. \qquad (3.5)$$

The bound state energies of the double waveguide system are calculated by using Eqs. 3.2 and 3.4 while taking $K_\perp = 0$. When the two photonic quantum wells are far apart from one another

41

(i.e. the thickness of the central photonic barrier layer d is large), Eqs. 3.2 reduce to the single transcendental equation obtained in reference [26]:

$$\tan\left[K_A\left(\varepsilon_m\right)d_A + \frac{m\pi}{2}\right] = \frac{\sqrt{F_A^2\left(\varepsilon_m\right) - F_B^2\left(\varepsilon_m\right) - K_A^2}}{K_A\left(\varepsilon_m\right)} \tag{3.6}$$

In the above equation, ε_m corresponds to the degenerate bound states in the two single, isolated photonic quantum wells.

For a given quantum number m, the transcendental equations for the symmetric and anti-symmetric bound states in Eqs. 3.2 have different solutions for the energies ε_m^+ and ε_m^-. Here an analytical expression is derived for the energy splitting $\Delta\varepsilon_m$ of the mth degenerate bound state, which is defined as $\Delta\varepsilon_m \equiv \varepsilon_m^- - \varepsilon_m^+$. The change in a degenerate bound state's energy due to the coupling between PQWs can be written as $\varepsilon_m^+ = \varepsilon_m + \delta\varepsilon_m^+$ for the symmetric states and $\varepsilon_m^- = \varepsilon_m + \delta\varepsilon_m^-$ for the anti-symmetric states. The energy splitting can then be calculated from Eqs. 3.2 by solving these two equations self-consistently. This is done by Taylor expanding near the degenerate state ε_m. After rigorous mathematical manipulations, the expression for $\Delta\varepsilon_m$ is obtained as

$$\Delta\varepsilon_m = \sum_{\pm}\left\{\pm\frac{\arctan\left[\frac{K_B\left(\varepsilon_m^{\pm}\right)}{K_A\left(\varepsilon_m^{\pm}\right)}\Omega_{\pm}\right] - \frac{1}{2}K_A\left(\varepsilon_m\right)d_A + \frac{m\pi}{2}}{\alpha_A d_A - \frac{\alpha_B K_A\left(\varepsilon_m\right) - \alpha_A K_B\left(\varepsilon_m\right)}{K_A\left(\varepsilon_m\right)^2 + K_B\left(\varepsilon_m\right)^2} - \eta_{\pm}}\right\}, \tag{3.7}$$

where
$$\eta_{\pm} = \frac{\left[\alpha_B K_A\left(\varepsilon_m\right) - \alpha_A K_B\left(\varepsilon_m\right)\right]\Omega_{\pm} \pm \alpha_B K_A\left(\varepsilon_m\right)K_B\left(\varepsilon_m\right)\Lambda_{\pm}^2 d/2}{K_A\left(\varepsilon_m\right)^2 + K_B\left(\varepsilon_m\right)^2\Omega_{\pm}^2}, \tag{3.8}$$

$$\Lambda_+ = \sec h\left[\frac{1}{2}K_B\left(\varepsilon_m\right)d\right] \tag{3.9}$$
$$\Lambda_- = \csc h\left[\frac{1}{2}K_B\left(\varepsilon_m\right)d\right],$$

42

and

$$\alpha_i = \sum_{\pm} \pm \frac{(n_i \pm n)^2}{4 n_i n L_i \sin\left[K_i\left(\varepsilon_m\right) L_i\right]} \left[\frac{2 n_i r_i + n\left(L_i - 2 r_i\right)}{\hbar c}\right] \sin\left\{\frac{\varepsilon_k}{\hbar c}\left[2 n_i r_i \pm n\left(L_i - 2 r_i\right)\right]\right\}.$$

(3.10)

To calculate the energy splitting from Eq. 3.7, the Bloch wave vectors K_A and K_B are used. Expressions for these wave vectors are defined by Eqs. 3.4 and 3.5, which show that they are functions of the refractive indices of the dielectric spheres and background materials, lattice constants, and sphere radii of photonic crystals A and B. When $d \gg 1/K_B\left(\varepsilon_m\right)$, the expression for the energy splitting given in Eq. 3.7 is reduced to

$$\Delta\varepsilon_m = \frac{2 K_A\left(\varepsilon_m\right) K_B\left(\varepsilon_m\right) \exp\left[-K_B\left(\varepsilon_m\right) d\right]}{\left[\alpha_A d_A - \frac{\alpha_B K_A(\varepsilon_m) - \alpha_A K_B(\varepsilon_m)}{K_A(\varepsilon_m)^2 + K_B(\varepsilon_m)^2}\right]\left[K_A\left(\varepsilon_m\right)^2 - K_B\left(\varepsilon_m\right)^2\right]}.$$

(3.11)

The above expression clearly indicates that $\Delta\varepsilon_m$ decreases exponentially with the well separation d, which means that when the well separation becomes large enough, the energy splitting will no longer be resolved.

3.3   Results and Discussion

In the following simulations it is considered that photonic crystals A and B are each composed of periodically arranged dielectric spheres embedded in a dielectric background material. The dielectric background material for both crystals is taken as air so that $n = 1$. For photonic crystal A, the dielectric spheres are made of polystyrene, a material which has a strong and fast Kerr nonlinear optical response. Photonic crystals consisting of polystyrene have been used in recent studies for developing ultrafast all-optical switches [18-20]. The refractive index of the polystyrene spheres in photonic crystal A, n_A, is obtained as a function of the applied pump laser field intensity, I_p, using Eq. 3.1, with parameters $n_0 = 1.59$ and $n_{nL} = 1.15 \times 10^{-12}$ cm^2/W [20]. The dielectric spheres in photonic crystal B are taken to be silica, with $n_B = 1.45$. Since the third-order nonlinear susceptibility of silica is on the order of 10^{-16} cm^2/W [28], n_B remains unaffected by the pump laser field.

The energies of the upper ("conduction band") and lower ("valence band") edges of the photonic band gaps for photonic crystals A and B are denoted as ε_{cb}^A and ε_{vb}^A for crystal A

and as ε_{cb}^B and ε_{vb}^B for crystal B, and are obtained numerically by solving the transcendental equations given in Eq. 3.5. For photonic crystal A, the radius of the polystyrene spheres is $r_A = 175$ nm and the lattice constant is $L_A = 473$ nm, for which it is found that $\varepsilon_{vb}^A = 0.83187$ eV and $\varepsilon_{cb}^A = 0.97656$ eV. For photonic crystal B, the radius of the silica spheres is $r_B = 188$ nm and the lattice constant is $L_B = 508$ nm, from which $\varepsilon_{vb}^B = 0.84819$ eV and $\varepsilon_{cb}^B = 0.97241$ eV are obtained. Note that with the chosen parameters, the upper photonic band edges of crystals A and B are approximately equal, i.e. $\varepsilon_{cb}^A \approx \varepsilon_{cb}^B$. This means that virtually no photonic well exists in the DPQW heterostructure until a sufficiently intense laser field is applied, and hence the present structure is actually a laser-induced double waveguide. The photonic well depth of the system is defined as $\Delta\varepsilon_{BA} \equiv \varepsilon_{cb}^B - \varepsilon_{cb}^A$, and in the absence of any external fields it takes the value $\Delta\varepsilon_{BA} = -0.00415$ eV. Note that with the chosen parameters, the upper photonic band edge of photonic crystal A is close to and slightly above that of B. This means that in the absence of any external fields, no bound states can exist within the double photonic waveguide system.

The energy levels of the bound photonic states formed in the double photonic waveguide heterostructure are calculated by numerically solving Eq. 3.2 for various quantum numbers m. The results are plotted in Figure 3-2, where the symmetric (ε_m^+) and anti-symmetric (ε_m^-) bound state energy levels of the double waveguide system are shown for the quantum numbers $m = 0$ and $m = 1$ as functions of the pump laser field intensity I_p. Here the lower and upper pairs of solid curves correspond to the $m = 0$ and $m = 1$ states, respectively, and for each pair the low- and high-energy curves correspond to the symmetric and anti-symmetric states, respectively. The diagonal dashed curve in Figure 3-2 indicates the value of ε_{cb}^A as a function of I_p, which shows the change in the depth of the photonic wells as the pump laser field intensity is increased. On the other hand, the horizontal dashed curve, corresponding to the value of ε_{cb}^B, remains unaffected by the pump laser field intensities considered here due to the negligible Kerr nonlinearity of photonic crystal B.

In the calculation of the bound state energies shown in Figure 3-2, the intensity of the pump laser field ranges from zero to 80 GW/cm^2, corresponding to a change in the effective refractive index of polystyrene from 1.59 to 1.68. Note that although these intensities are somewhat large, experimental studies on polystyrene photonic crystals have been conducted using comparable
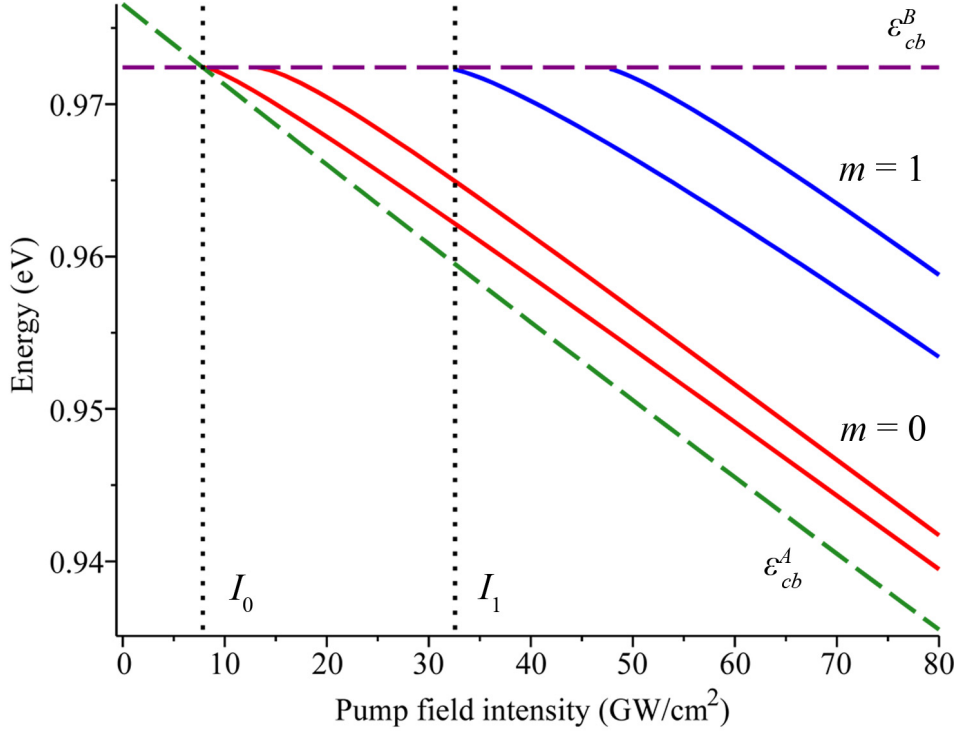
Figure 3-2: Bound state energy levels in the double waveguide heterostructure vs. pump field intensity I_p. The low-energy and high-energy pairs of solid curves correspond to the $m = 0$ and $m = 1$ symmetric and anti-symmetric states, respectively. The horizontal and diagonal dashed lines indicate the upper edges of the photonic band gaps in photonic crystals B and A, respectively, as functions of I_p. Dotted vertical lines indicate threshold intensities I_0 and I_1 for the formation of $m = 0$ and $m = 1$ states, respectively. The dimensions of the heterostructure were taken to be $d_B = 10L_B$, $d = 5L_B$, and $d_A = 20L_A$.

laser field intensities without damaging the samples [18-20]. Figure 3-2 shows that in the absence of the pump laser field (i.e., when $I_p = 0$), the system cannot support bound states. The minimum pump field intensity required to form a bound photonic state in the system (i.e., to induce PQWs) is indicated by the dotted vertical line on the left, for which $I_p = I_0$ where $I_0 = 7.85$ GW/cm^2 is the threshold intensity for the $m = 0$ bound state to exist in the double photonic waveguide heterostructure. Between this threshold intensity and the second, which occurs at $I_1 = 32.58$ GW/cm^2 and is represented by the dotted vertical line on the right, the system contains only one degenerate state and thus two split states. By further increasing the pump field so that $I_p > I_1$, an additional pair of split resonant states appears, corresponding to

the $m = 1$ degenerate state supported by the photonic wells. The results presented in Figure 3-2 clearly show that the number of resonant states formed in the nonlinear double waveguide system can be changed by varying the pump field intensity. This effect occurs due to the increase in photonic well depth ($\Delta\varepsilon_{BA}$) as the pump field becomes more intense, which allows more bound states to form within the photonic wells. To summarize, these results show that the nonlinear double waveguide system described here may be optically switched between zero, one or two pairs of bound states by changing the intensity of the pump laser field.

The transmission spectra of the DPQW heterostructure for an incident transverse electric, linearly polarized electromagnetic field propagating along the x-axis are numerically simulated using the transfer matrix method as outlined in Chapter 2. In Figure 3-3, the transmission coefficient for the heterostructure is shown as a function of incident photon energy for pump laser field intensities of 30 and 60 GW/cm^2. In each case, the transmission coefficient is calculated for the range of energies in which photon propagation is permitted in photonic crystal A but not photonic crystal B. This ensures that the transmitted peaks correspond to bound photonic states of the laser-induced DPQW system. In Figure 3-3(a), the transmission spectrum is shown for $I_p = 30$ GW/cm^2, which is between the critical intensities I_0 and I_1. Here the transmission coefficient is plotted for energies between $\varepsilon_{cb}^A = 0.96084$ eV and $\varepsilon_{cb}^B = 0.97241$ eV, and the photonic well depth is $\Delta\varepsilon_{BA} = 0.01157$ eV. For the pump laser field intensity considered in Figure 3-3(a), the DPQW heterostructure only supports the $m = 0$ symmetric and anti-symmetric states. In Figure 3-3(b) the transmission coefficient is plotted for $I_p = 60$ GW/cm^2, which is greater than the threshold intensity I_1. In this case the transmission coefficient is plotted from $\varepsilon_{cb}^A = 0.94552$ eV to $\varepsilon_{cb}^B = 0.97241$ eV, and the photonic well depth is $\Delta\varepsilon_{BA} = 0.02689$ eV. For the pump field intensity considered in Figure 3-3(b), both the $m = 0$ and $m = 1$ states are supported by the laser-induced double photonic waveguide.

The peaks in the transmission spectra shown in Figure 3-3 correspond to the resonant tunnelling states the system, which in turn indicate the energies of the bound states along the direction of confinement in the double photonic waveguide heterostructure. The resonant tunnelling states occur in split pairs due to the coupling of the degenerate bound states in the two photonic waveguides. Note that as shown in Figure 3-2, the spectral splitting of the degenerate states is larger for the states with higher energies. This is attributed to an increased
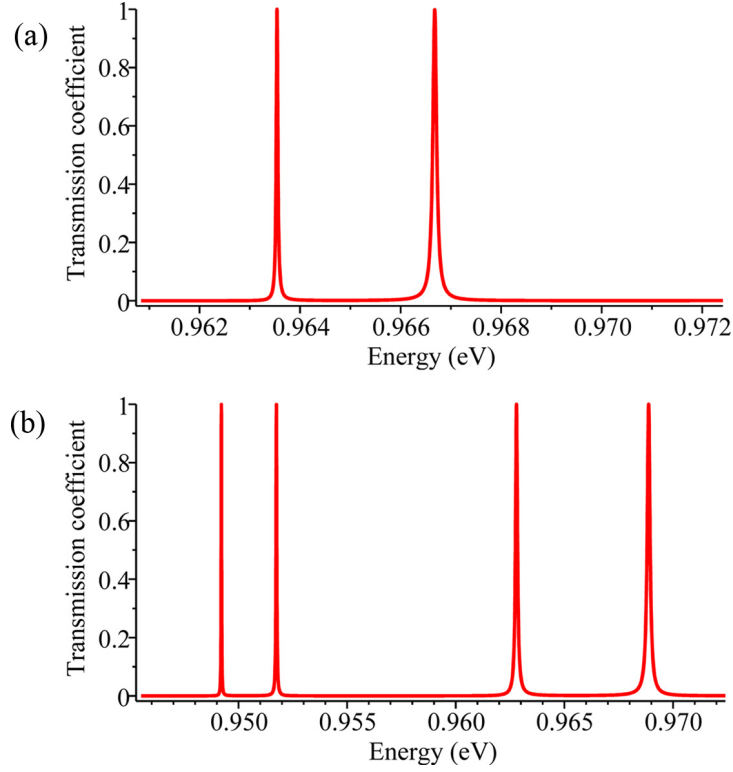
Figure 3-3: Transmission spectra for the double waveguide system for pump field intensities of (a) $I_p = 30$ and (b) 60 GW/cm^2. In each case the transmission spectrum is plotted for energies between the upper photonic band edges of photonic crystals A and B for the given intensity. Dimensions of the heterostructure were taken as $d_A = 20L_A$, $d_B = 10L_B$, and $d = 5L_B$.

photonic barrier tunnelling rate for those photons with energies near the upper edge of the photonic barriers, resulting in a stronger electric field coupling between the degenerate states [8, 13, 16]. The tunnelling rate enhancement near the barrier edge is also responsible for the increased bandwidth of transmitted resonant peaks at higher energies [8]. Note that for pump field intensities $I_p < I_0$, no resonant tunnelling peaks were observed in the numerical simulations of the transmission coefficient. For these intensities, the photonic wells are not deep enough to support any confined states.

In Figure 3-4 a two-dimensional plot of the transmission coefficient for the DPQW heterostructure is presented in which the photon energy is varied along the horizontal axis and the pump field intensity increases along the vertical axis. For pump field intensities such that $I_0 < I_p < I_1$, only one degenerate state is shared by the coupled photonic wells, which splits
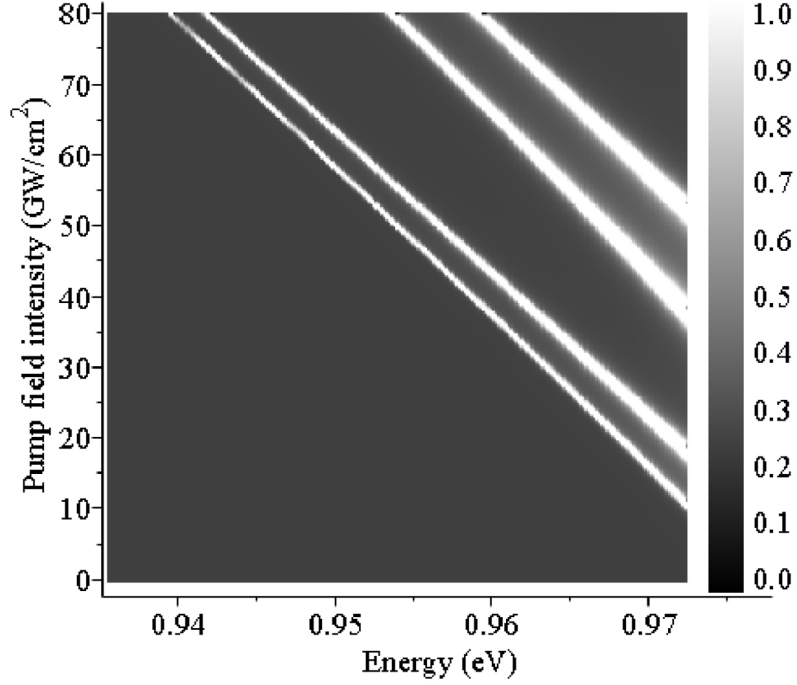
Figure 3-4: Two-dimensional plot of the transmission coefficient for the double photonic quantum well heterostructure. The incident photon energy ε_k (in eV) is given along the horizontal axis while the pump laser field intensity I_p (in GW/cm^2) is indicated by the vertical axis. Here the dimensions of the heterostructure are $d_A = 20L_A$, $d_B = 10L_B$ and $d = 5L_B$.

into two transmission peaks corresponding to the symmetric (low-energy) and anti-symmetric (high-energy) states. In the range of pump field intensities considered, $I_p > I_1$ gives two resonant tunnelling peaks in the transmission spectrum. Note that in both regimes, the number and locations of the resonant tunnelling peaks corresponds to the energy levels predicted in Figure 3-2. These results clearly indicate that the double photonic waveguide system can be switched between having zero, one, or several resonant states by changing the intensity of the pump field below, between or above the critical intensities I_0 and I_1.

At this point, the bound state energies and resonant tunnelling peaks of the double waveguide heterostructure have been investigated, but the degree of energy splitting between symmetric and anti-symmetric states in the coupled waveguides has not yet been studied quantitatively. The derived expression for the energy splitting of a degenerate bound state with quantum number m is given by Eq. 3.7. Here, the expression for $\Delta\varepsilon_m$ is compared with the spectral splitting

observed in the numerically simulated transmission spectra. The effect of the inter-well coupling in the double photonic waveguide system is investigated by changing the thickness of the photonic barrier d, which separates the two layers of photonic crystal A in the heterostructure (see Figure 3-1(a)). In Figure 3-5, the energy splittings for the $m = 0$ (solid curve) and $m = 1$ (dashed curve) states have been plotted as functions of the waveguide separation d. Here the thicknesses of the outer photonic barriers and photonic wells are $d_B = 10L_B$ and $d_A = 20L_A$, while the pump field intensity is $I_p = 60$ GW/cm^2. Note that this pump field intensity is well above the critical intensity I_1, and therefore results in two pairs of confined states in the double waveguide structure. The energy splitting measured from the resonant peaks in the corresponding simulated transmission spectra are also shown in Figure 3-5, where the circles and diamonds indicate the $m = 0$ and $m = 1$ states, respectively.

The results presented in Figure 3-5 show that the energy splitting $\Delta\varepsilon_m$ decreases as the separation between the PQWs d increases. When the photonic wells are further apart, their coupling strength decreases, and hence so does the energy splitting effect. It is also found that the energy splitting for the $m = 1$ state is larger than that for the $m = 0$ state, as higher-energy states penetrate further into central photonic barrier and thus couple more strongly with their degenerate counterpart in the neighboring photonic well. Figure 3-5 shows that there is good agreement between the energy splitting measured from the transmission spectra of the double photonic waveguide structure and that predicted by Eq. 3.7. Since the analytical expression for $\Delta\varepsilon_m$ is based on a Taylor expansion, its accuracy increases as the energy perturbation becomes smaller. Thus for a double waveguide system with a greater well separation, the expression for $\Delta\varepsilon_m$ is more accurate because the coupling between photonic wells is weaker. For this reason, Figure 3-5 shows better agreement between the $\Delta\varepsilon_m$ measured from the simulated transmission spectra and from Eq. 3.7 for the $m = 0$ state than the $m = 1$ state. Note that as the two photonic wells in the heterostructure become increasingly far away from one another, the energy splitting decreases exponentially. For a large enough separation, the two waveguides can be considered separate and isolated, and the energy splitting effect is negligible.

The energy splitting of bound states in the double waveguide heterostructure arises due to the finite width of the central photonic barrier separating the photonic wells, which allows the electromagnetic fields of degenerate bound states in each well to spatially overlap one another.
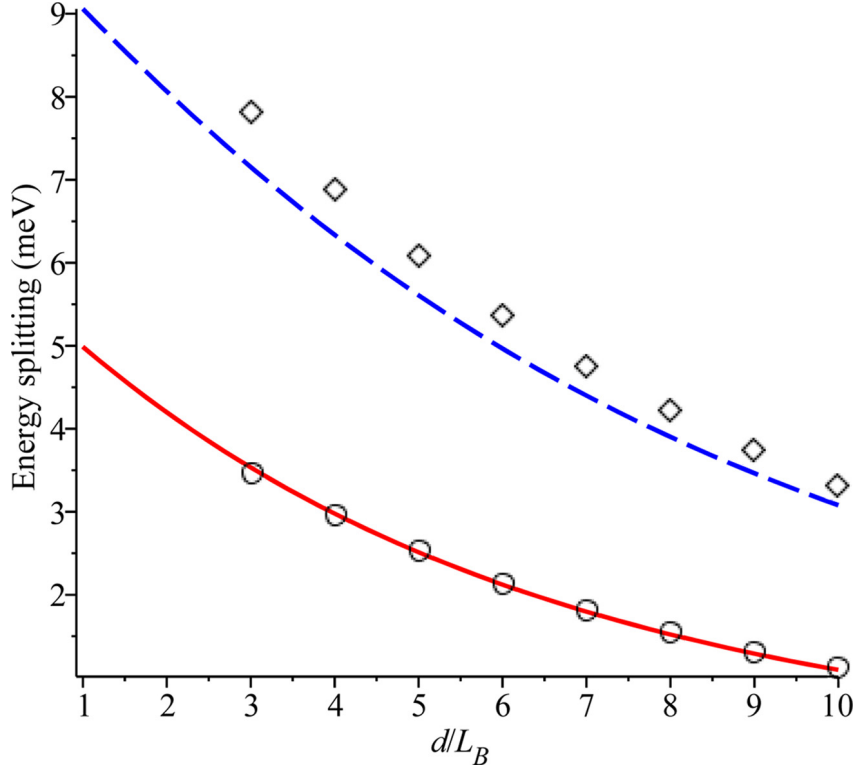
Figure 3-5: Energy splitting $\Delta\varepsilon_m$ vs. photonic quantum well separation d in the double waveguide heterostructure. The solid and dashed curves correspond to the energy splitting of the $m = 0$ and $m = 1$ states, respectively, as given from Eq. 3.7. The circles and diamonds correspond to the splitting of the $m = 0$ and 1 states, respectively, as measured from the resonant tunnelling peaks in the simulated transmission spectra. In these calculations the dimensions of the heterostructure are taken as $d_A = 20L_A$ and $d_B = 10L_B$, and the pump field intensity is $I_p = 60 \text{ GW/cm}^2$.

This overlap causes the degenerate states to split into pairs of symmetric and anti-symmetric states. Figure 3-2 shows that at higher pump field intensities, more bound states exist in the heterostructure. Here, the depth of the photonic wells is proportional to the pump field intensity, and deeper photonic wells contain more bound photonic states [7-11]. The present theoretical predictions agree qualitatively with the results observed for various types of DPQW structures [13, 16, 17].

According to Eq. 3.7, the energy splitting of the mth bound state is a function of the degenerate bound state energy ε_m, which in turn depends on the intensity of the pump laser field. Hence, the energy splitting of the bound states in the double photonic waveguide heterostruc-
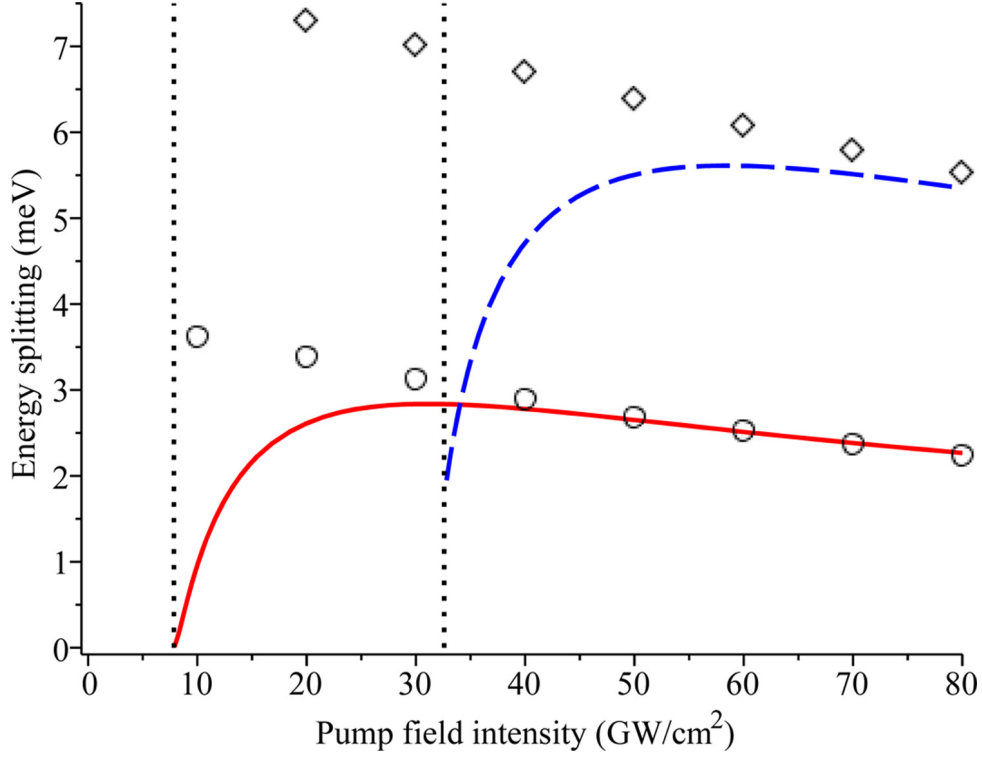
Figure 3-6: Energy splitting of bound states in the double waveguide system vs. pump laser field intensity I_p. The solid and dashed curves correspond to the energy splitting of the $m = 0$ and $m = 1$ states, respectively, as given from Eq. 3.7. The circles and diamonds indicate the energy splitting of the $m = 0$ and $m = 1$ resonant peaks as measured from the simulated transmission spectra for the heterostructure. Here the dimensions of the heterostructure are $d_A = 20L_A$, $d_B = 10L_B$ and $d = 5L_B$.

ture can be controlled by the pump laser field. In Figure 3-6, the energy splittings of the $m = 0$ and $m = 1$ states are plotted as functions of the pump laser field intensity I_p. The solid and dashed curves correspond to the energy splitting of the $m = 0$ and $m = 1$ states, respectively, as calculated using Eq. 3.7. These results are compared with the energy splitting measured from the simulated transmission spectra, where the circles and diamonds in Figure 3-6 correspond to the energy splitting of the $m = 0$ and $m = 1$ resonant tunnelling peaks, respectively.

The results presented in Figure 3-6 show that generally, the energy splitting of each degenerate state in the double waveguide structure decreases with increasing pump field intensity. As the intensity of the pump field increases, the upper photonic band edge of photonic crystal A (ε_{cb}^A) and the energies of the degenerate bound states in the photonic well (ε_m) decrease. In turn,

the inter-well coupling between degenerate states is diminished, resulting in a decrease in their energy splitting. The results from the analytical expression for $\Delta\varepsilon_m$ given by Eq. 3.7 shown in Figure 3-6 (see solid and dashed curves) rise sharply as I_p increases at the appearance of a new bound state, and then converge with the results measured from the simulated transmission spectra. The deviation in the energy splitting predicted by the analytical expression for $\Delta\varepsilon_m$ and that measured from the simulated transmission spectra for the double waveguide system occurs when the lower-energy symmetric state lies within the photonic barrier, but the higher-energy anti-symmetric state lies above the upper edge of the barrier. This situation occurs for pump field intensities just above I_0 or just above I_1. In these cases, the transcendental equation for ε_m^+ given in Eq. 3.2 is valid, while that for ε_m^- given in Eq. 3.2 is not. Therefore, Eq. 3.7 does not apply in these cases because it is derived from Eqs. 3.2. However when the pump field intensity is sufficiently high, both the symmetric and anti-symmetric split states lie below the photonic barriers of the system. In this case, Eq. 3.2 is valid and the analytical expression for $\Delta\varepsilon_m$ converges with that measured from the simulated transmission spectra. Note that there is still some deviation in these results due to the inherent inaccuracy of the Taylor expansion used to derive Eq. 3.7, an effect which is enhanced when the bound states have energies lying close to the top of the photonic barrier.

Finally, the effect of an external stress field applied to photonic crystals B on the bound states in the double waveguide heterostructure is investigated. The radius of the dielectric spheres r_B and the lattice constant L_B along the x-direction in crystal B can be modified slightly by applying external stress and strain fields. Simply put, the aim here is to study the effect of the variation in the dielectric sphere radii in photonic crystal B on the bound states and their energy splitting. In Figure 3-7, the bound state energy levels ε_m^+ and ε_m^- and the photonic band edges ε_{cb}^A and ε_{cb}^B are plotted as functions of the dielectric sphere radius r_B. Here the external pump laser field is absent, i.e., $I_p = 0$. The physical parameters for photonic crystal A remain the same as those used elsewhere in this chapter, while for crystal B the relation $L_B = 2r_B/0.74$ has been used as r_B is varied between 180 and 188 nm. This corresponds to at most a 8 nm decrease from the value of r_B used in previous calculations. The symmetric and anti-symmetric energy levels of the $m = 0$ and $m = 1$ states are plotted in Figure 3-7 as solid curves, whereas the upper photonic band edges of crystals A and B are plotted as dashed
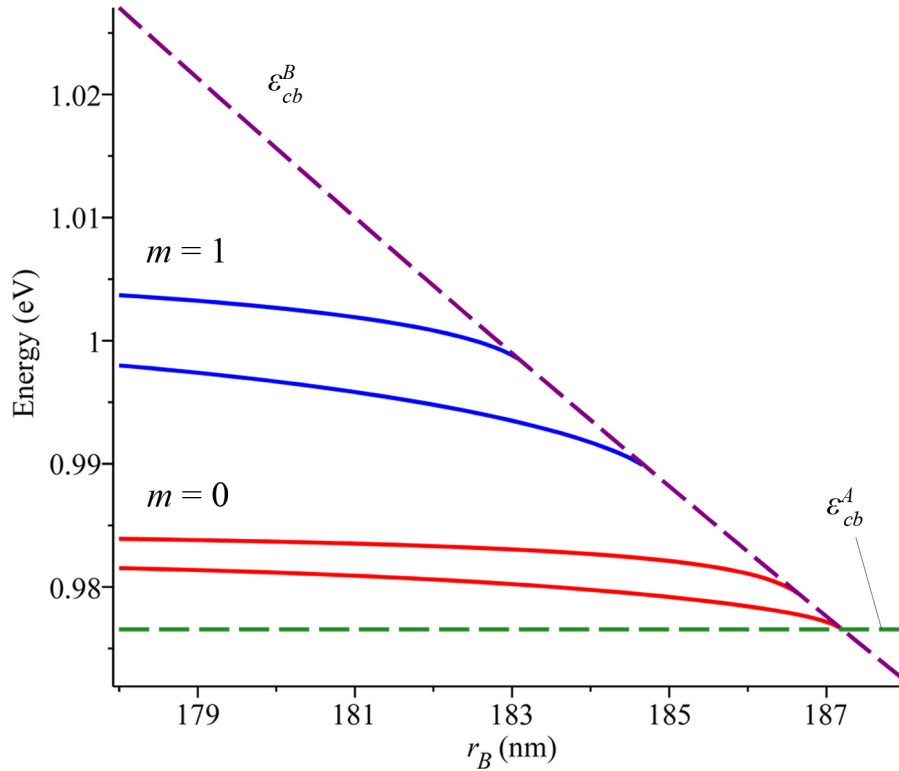
Figure 3-7: Energy levels of the $m = 0$ (low-energy pair of solid curves) and $m = 1$ (high-energy pair of solid curves) symmetric and anti-symmetric split states in the double waveguide heterostructure as a function of the dielectric sphere radius in photonic crystal B. The upper photonic band edges of photonic crystals A and B are indicated by the horizontal and diagonal dashed curves, respectively. Dimensions of the heterostructure are $d_A = 20L_A$, $d_B = 10L_B$, and $d = 5L_B$, and the relation $L_B = 2r_B/0.74$ has been used.

curves. Note that here the photonic band gap of crystal A is independent of the value r_B and thus remains constant.

The results presented in Figure 3-7 indicate that for $r_B > 187$ nm (r_0), the system contains no bound states. When $r_1 < r_B < r_0$, the double photonic waveguide heterostructure supports only the $m = 0$ pair of bound states, where $r_1 = 185$ nm. The symmetric and anti-symmetric $m = 0$ states are indicated by the lower energy pair of solid curves in Figure 3-7. The system contains two pairs of split states when $r_B < r_1$, where the next pair of resonant states corresponds to the $m = 1$ degenerate state in the PQWs. These pairs of resonant states appear due to the increase in depth of the photonic wells of the double waveguide system ($\Delta \varepsilon_{BA}$) as

r_B is decreased. In this case, however, the photonic wells become deeper due to an increase in the height of the photonic barriers (ε_{cb}^B) as r_B decreases, as opposed to decreasing ε_{cb}^A with the applied laser field as done in the previous calculations. Figure 3-7 shows that the double waveguide system can be switched from zero to one or two pairs of resonant states by changing the radius of the dielectric spheres in photonic crystal B.

3.4   Conclusions

In this chapter, the energy splitting of bound photonic states in a Kerr-nonlinear double photonic waveguide (quantum well) heterostructure has been investigated. The present photonic heterostructure is fabricated using two photonic crystals A and B arranged in the sequence B/A/B/A/B along one direction. It is considered that photonic crystals A and B are each composed of periodically-arranged dielectric spheres in a dielectric background material. For photonic crystal A, the dielectric spheres are made of polystyrene, which has a strong and fast Kerr nonlinear optical response. Photonic crystal B contains dielectric spheres made of silica, which has a negligible Kerr nonlinearity compared to that of polystyrene.

Parameters for photonic crystals A and B are chosen so that in the absence of external fields, the photonic band gaps of crystals A and B are nearly equal. In this situation, there are no photonic wells in the system. It is shown that the application of an external pump laser field changes the refractive index of the polystyrene spheres in photonic crystal A due to the Kerr effect. This change in refractive index decreases the upper edge of photonic crystal A's photonic band gap, inducing two coupled photonic wells in the heterostructure which each support one or more bound photonic states. Similarly the application of external stress or strain fields to photonic crystal B can cause a change in the radius of its constituent dielectric spheres. This causes the upper edge of photonic crystal B's photonic band gap to increase, which also induces photonic wells in the heterostructure that can each support one or more bound states.

Here it is shown that the bound photonic states in each of the two photonic wells couple to one another through the central photonic barrier in the heterostructure. This coupling causes the degenerate bound states to split into symmetric and anti-symmetric states. Analytical expressions for the energy levels of the symmetric and anti-symmetric bound states in the

heterostructure and their energy splitting have been derived. Transmission spectra for the heterostructure along the direction of confinement have been numerically simulated, from which resonant tunnelling peaks are observed. These peaks match the energy levels of the split bound states in the double waveguide heterostructure.

The results presented in this chapter demonstrate that the nonlinear double photonic waveguide system can be optically switched between supporting zero, one or more bound states. Numerical simulations for this system have shown that the energy levels of these bound states and their splitting can be controlled by varying the distance between the two waveguides, adjusting the intensity of the applied pump laser field or by applying stress and strain fields. It is shown that the phenomenon of resonant photonic tunnelling can occur when incident light is applied to the system along the direction of photon confinement. The system described here can be used as an all-optical switch for a probe laser applied along the direction of confinement, whereby resonant transmission of the probe field at a specific frequency can be switched on or off by the pump laser field. A similar type of switched mechanism was proposed by Tran [23] for a Kerr-nonlinear photonic crystal with a defect state. The present system may also be used as a tunable optical filter, and by combining several such devices with photonic waveguides, tunable multichannel filters may be fabricated. The results presented here may be used to develop ultrafast all-optical switching devices, tunable filters and coupled waveguides.

Bibliography

[1] E. Yablonovitch, *Phys. Rev. Lett.* **58**, 2059 (1987).

[2] S. John, *Phys. Rev. Lett.* **58**, 2486 (1987).

[3] J. D. Joannopoulos, S. G. Johnson, J. N. Winn, and R. D. Meade, *Photonic Crystals: Molding the Flow of Light*, 2nd ed. (Princeton University Press, Princeton, New Jersey, 2008).

[4] S. Y. Lin and G. Arjavalingam, *J. Opt. Soc. Am. B* **11**, 2124 (1994).

[5] S. Y. Lin, V. M. Hietala, S. K. Lyo, and A. Zaslavsky, *Appl. Phys. Lett.* **68**, 3233 (1996).

[6] J. Zi, J. Wan, and C. Zhang, *Appl. Phys. Lett.* **73**, 2084 (1998).

[7] F. Qiao, C. Zhang, J. Wan, and J. Zi, *Appl. Phys. Lett.* **77**, 3698 (2000).

[8] Y. Jiang, C. Niu and D. L. Lin, *Phys. Rev. B* **59**, 9981 (1999).

[9] H. M. Fei, Y. Jiang, J. Q. Liang, and D. L. Lin, *J. Phys. B* **42**, 055401 (2009).

[10] S. Yano, Y. Segawa, J. S. Bae, K. Mizuno, H. Miyazaki, K. Ohtaka, and S. Yamaguchi, *Phys. Rev. B* **63**, 153316 (2001).

[11] X. Chen, W. Lu, and S. C. Shen, *Solid State Commun.* **127**, 541 (2003).

[12] S. H. Xu, Z. H. Xiong, L. L. Gu, Y. Liu, X. M. Ding, J. Zi, and X. Y. Hou, *Solid State Commun.* **126**, 125 (2003).

[13] S. H. Xu, X. M. Ding, Z. H. Xiong, Y. Liu, Y. Liu, Z. J. Wang, J. Zi, and X. Y. Hou, *Photonics Nanostruct. Fundam. Appl.* **4**, 17 (2006).

[14] C. S. Feng et al., *Solid State Commun.* **135**, 330 (2005).

[15] R. Liu and B. Gai, *J. Opt. Soc. Am. B* **24**, 2369 (2007).

[16] J. Liu, J. Sun, C. Huang, W. Hu, and M. Chen, *IET Optoelectron.* **2**, 122 (2008).

[17] S. M. Sadeghi and W. Li, *Phys. Rev. B* **81**, 155317 (2010).

[18] Y. Liu, F. Qin, Z.-Y. Wei, Q.-B. Meng, D.-Z. Zhang, and Z.-Y. Li, *Appl. Phys. Lett.* **95**, 131116 (2009).

[19] Y. Lin, F. Qin, F. Zhou and Z.-Y. Li, *J. Appl. Phys.* **106**, 083102 (2009).

[20] F. Qin, Y. Liu and Z.-Y. Li, *J. Opt.* **12**, 035209 (2010).

[21] *Nonlinear Photonic Crystals*, edited by R. E. Slusher and B. J. Eggleton (Springer-Verlag, Berlin, 2003).

[22] M. Scalora, J. P. Dowling, C. M. Bowden, and M. J. Bloemer, *Phys. Rev. Lett.* **73**, 1368 (1994).

[23] P. Tran, *J. Opt. Soc. Am. B* **14**, 2589 (1997).

[24] D. A. Mazurenko, R. Kerst, J. I. Dijkhuis, A.V. Akimov, V.G. Golubev, D. A. Kurdyukov, A. B. Pevtsov, and A.V. Sel'kin, *Phys. Rev. Lett.* **91**, 213903 (2003).

[25] M. R. Singh and R. Lipson, *J. Phys. B* **41**, 015401 (2008).

[26] A. Yariv and P. Yeh, *Photonics: Optical Electronics in Modern Communications* (Oxford University Press, New York, 2007).

[27] M. R. Singh and J. D. Cox, *AIP Conf. Proc.* **1147**, 256 (2009).

[28] R. W. Boyd, *Nonlinear Optics*, 3rd ed. (Academic, New York, 2008).

[29] S. John and J. Wang, *Phys. Rev. B* **43**, 12772 (1991).

[30] P. Lambropoulos, G. M. Nikolopoulos, T. R. Nielsen, and S. Bay, *Rep. Prog. Phys.* **63**, 455 (2000).

[31] D. Petrosyan and G. Kurizki, *Phys. Rev. A* **64**, 023810 (2001).

Chapter 4

Nanophotonic Phenomena in Graphene Heterostructures

In the previous two chapters, photonic heterostructures containing photonic crystals as optically active components were studied and shown to exhibit optical properties which exceed the capabilities of the sum of the individual components. For example, in Chapter 2, photonic quantum well heterostructures were fabricated by combining two photonic crystals with different photonic band gaps. One might expect that in this case, the resulting heterostructure would simply possess a larger photonic band gap which is the combination of the two band gaps from the individual photonic crystals. However, the photonic heterostructure was shown to have far more interesting properties, such as the ability to support bound photonic states which allow resonant photonic tunnelling to occur through a photonic band gap. In this chapter, heterostructures consisting of nano-scale graphene and semiconducting components are investigated[1]. Here, as well, the resulting heterostructure (or nanocomposite) is found to exhibit optoelectronic properties that are not merely the sum of those for the individual components.

---

[1]The material presented in this chapter has been published in: J. D. Cox, M. R. Singh, G. Gumbs, M. A. Antón, and Fernando Carreño, *Phys. Rev. B* **86**, 125452 (2012).

4.1   Introduction

There has been growing interest in developing nanoscale optoelectronic devices by combining nanomaterials with complementary optical properties into composite (hybrid) structures. The number of possible composite systems that can be built from already existing nanostructures is simply enormous. A significant amount of research on nanocomposites has been devoted to the study of exciton-plasmon interactions in metal-semiconductor nanostructures, which offer a wide range of opportunities to control light-matter interactions and electromagnetic energy flows on nanometer length scales [1-6]. Strong exciton-surface plasmon coupling in semiconductor quantum dot (QD)-metal nanoparticle systems could lead to efficient transmission of quantum information between qubits for applications in quantum computing and communication [2]. These nanostructures also have applications in biophotonics and sensing, where nonradiative energy transfer between a QD and metal nanoparticle can be used to detect biological molecules [3].

In this chapter, the dipole-dipole interaction and energy transfer between a quantum emitter and a graphene nanodisk is investigated theoretically. The quantum emitter can be a QD, nanocrystal or a chemical or biological molecule. In the present study, the quantum emitter-graphene system is embedded in a nonlinear photonic crystal, which acts as a tunable photonic reservoir for the emitter. Photonic crystals are engineered, periodically-ordered microstructures that facilitate the trapping and control of light on the microscopic level. Applications for photonic crystals include all-optical microchips for optical information processing, optical communication networks, sensors and solar energy harvesting [7-12]. The nonlinear photonic crystal considered here has a refractive index distribution that can be tuned optically, and is used to manipulate the interaction between the quantum emitter and graphene nanodisk.

For the present nanocomposite system, surface plasmons are created in the graphene nanodisk when an external electromagnetic is applied. Surface plasmons are the collective oscillations of conduction band electrons at the interface between conducting and dielectric media. Plasmonics is widely studied due to applications in ultrasensitive optical biosensing [13], photonic metamaterials [14], light harvesting [15], optical nanoantennas [16] and quantum information processing [17]. Generally, noble metals are considered to be the best available materials for the study of surface plasmon polaritons [18]. However, noble metals are hardly tunable

and exhibit large Ohmic losses which limit their applicability to optical processing devices. Graphene plasmons provide an attractive alternative to noble-metal plasmons as they exhibit much tighter confinement and relatively long propagation distances. Furthermore, surface plasmons in graphene have the advantage of being highly tunable via electrostatic gating. Compared to noble metals, graphene also has superior electronic and mechanical properties, which originate in part from its charge carriers of zero effective mass [19]. For example, charge carriers in graphene can travel for micrometers without scattering at room temperature. Graphene has also been recognized as a useful optical material for novel photonic and optoelectronic applications [20-25]. For these reasons, the study of plasmonics in graphene has received significant attention both experimentally and theoretically [21, 22, 26-29].

Recently, experimental research on graphene has been extended to the fabrication and study of QD-graphene nanostructures [30-34]. For example, a CdS QD-graphene hybrid system has been synthesized by Cao et al. [30], in which a picosecond ultrafast electron transfer process from the excited QD to the graphene matrix was observed using time-resolved fluorescence spectroscopy. Chen et al. [31] have fabricated CdSe/ZnS-QDs in contact with single- and few-layer graphene sheets. By measuring the strong quenching of the QD fluorescence, they determined the rate of energy transfer from the QD to graphene. A similar study by Dong et al. [32] was performed on a CdTe-QD and graphene oxide system, but in their case the QDs were modified with molecular beacons in order to demonstrate that the hybrid system can be used for sensing biological molecules. Wang et al. [33] have synthesized graphene–CdS and graphene–ZnS QD hybrid systems directly from graphene oxide, with CdS and ZnS QDs very well dispersed on the graphene nanosheets. They also measured the QD photoluminescence and observed the energy transfer between the QDs and graphene. Metal nanoparticle-graphene hybrid systems have also been fabricated by several groups [21, 35-37].

In the present chapter a QD-graphene hybrid system is investigated, for which energy transfer occurs due to the interaction between optical excitations in the QD and graphene nanodisk. The optical excitations in the QD are excitons, which are electron-hole pairs, while those in the graphene nanodisk are surface plasmon polaritons, which are created due to the collective oscillations of conduction band electrons. The QD is taken as a three-level system in which two distinct excitonic transitions occur. Three-level quantum emitters in the ladder- [3] and

V-type [38] configurations interacting with a metallic nanoparticle in the presence of two external laser fields have been studied. Here a probe laser field is applied to the system, which is coupled with one excitonic transition and measures the energy transfer spectra of the QD and graphene. Additionally, it is considered that a control laser field is applied to monitor and control the energy transfer. Besides creating excitons in the QD, these fields also generate surface plasmon polaritons in graphene. The dipoles created by excitons in the QD and plasmons in the graphene nanodisk then interact via the dipole-dipole interaction (DDI). This interaction is strong when the QD and graphene are in close proximity and their optical excitation frequencies are resonant.

It is found that the power absorption spectrum of the QD has two peaks when the QD and graphene nanodisk are in close proximity, indicating the creation of two dressed excitons in the QD due to the DDI. These dressed excitons are transported to graphene, and produce two peaks in the spectrum of the energy transfer rate to graphene. The energy transfer between the QD and graphene can be switched on and off by changing the strength of the dipole-dipole coupling or by applying an intense laser field to the nonlinear photonic crystal. The intensities of peaks in the energy transfer rate spectra can be controlled by changing the number of graphene monolayers or by changing the distance between the QD and graphene. It is also predicted that the intensity of these peaks can be modified in the presence of biological materials. The findings presented in this chapter agree with the experimental results of Refs. [30-34] on a qualitative basis. The present system can be used to fabricate nano-biosensors, all-optical nano-switches and energy transfer devices.

4.2   Theoretical Formalism

The dipole-dipole interaction and energy transfer between a quantum dot (QD) and graphene nanodisk are investigated theoretically for a graphene-QD heterostructure embedded in a nonlinear photonic crystal. The combined QD-graphene nanodisk system can also be referred to as a QD-graphene nanocomposite or hybrid system. A schematic diagram for the present system is shown in Figure 4-1(a). A graphene nanodisk (or nanoflake) lies in the x-y plane, on top of which a QD is deposited. The center-to-center distance between the QD and graphene nanodisk
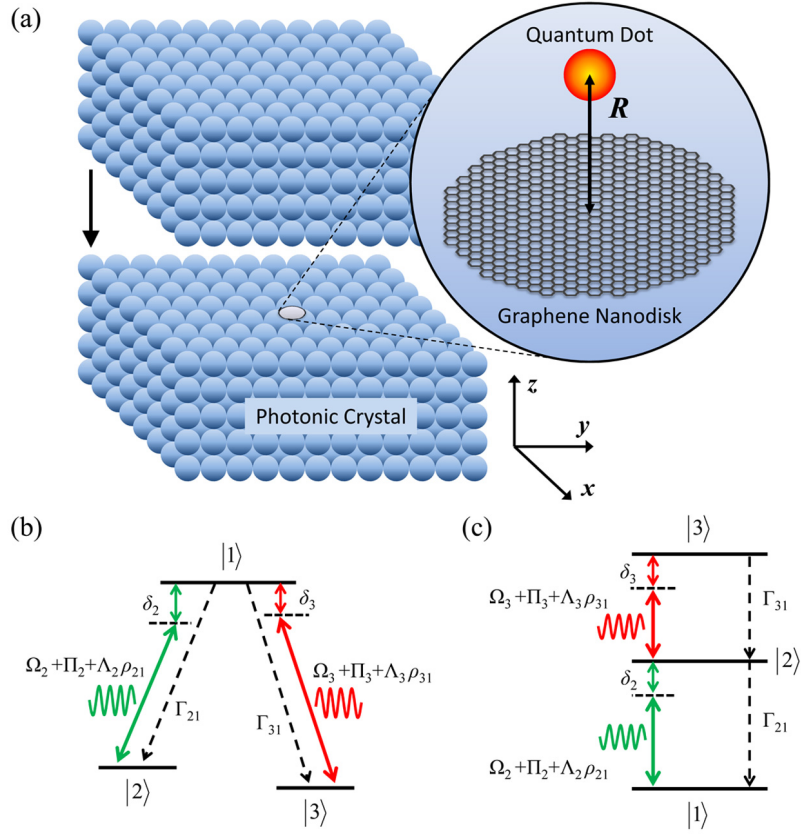
Figure 4-1: (a) Schematic diagram of the QD-graphene nanocomposite embedded in a photonic crystal. (b) Energy level diagram for the lambda-type QD, where $|2\rangle$ and $|3\rangle$ denote the lower-energy states which are both coupled to the common optically excited state $|1\rangle$. (c) Energy level diagram for the ladder-type QD, where $|1\rangle$, $|2\rangle$, and $|3\rangle$ denote the ground, first excited, and second excited states.

is denoted by R. The distance between the quantum dot and graphene R can be controlled by using the following methods: (a) by using a passive dielectric spacer between the quantum dot and graphene, (b) using quantum dots with different diameters, (c) by applying an external stress or strain fields to the system, and (d) by changing the concentration of quantum dots or graphene nanodisks.

Here it is considered that the QD has three discrete energy states, denoted as $|1\rangle$, $|2\rangle$ and $|3\rangle$. In this chapter, two types of three-level quantum dots are considered. These are the so-called lambda- and ladder-type energy level configurations. In the lambda-type energy level configuration, states $|2\rangle$ and $|3\rangle$ are the lower-energy states and $|1\rangle$ is the higher-energy

excited state. Optical excitation occurs via the transitions $|2\rangle \leftrightarrow |1\rangle$ and $|3\rangle \leftrightarrow |1\rangle$, which have resonance frequencies (dipole moments) ω_{12} ($\boldsymbol{\mu}_{12}$) and ω_{13} ($\boldsymbol{\mu}_{13}$), respectively (see Figure 4-1(b)). In the ladder-type energy level configuration, $|1\rangle$, $|2\rangle$ and $|3\rangle$ denote the ground, first excited and second excited states, respectively. Optical excitation the occurs via the transitions $|1\rangle \leftrightarrow |2\rangle$ and $|2\rangle \leftrightarrow |3\rangle$, which have resonance frequencies (dipole moments) ω_{12} ($\boldsymbol{\mu}_{12}$) and ω_{23} ($\boldsymbol{\mu}_{23}$), respectively (see Figure 4-1(c)). In this section, the lambda-type energy level configuration is used to present the theoretical formalism for the dipole-dipole interaction and energy transfer between a three-level quantum emitter (i.e., QD) and graphene nanodisk. This energy level configuration has been widely studied in atoms, where quantum optical effects such as electromagnetically induced transparency and coherent population trapping have been demonstrated [39, 40]. More recently, the lambda-type energy level configuration has been achieved in semiconductor QDs [41-43]. The extension of the following theoretical formalism to the ladder-type system is very straightforward, and is presented at the end of the section.

In the present model, it is considered that two external laser field are applied to the nanocomposite system. The first field is designated as the probe laser field, and is assumed to couple with the $|1\rangle \leftrightarrow |2\rangle$ transition in the QD. The probe laser field has frequency ω_2 and electric field $\mathbf{E}_2$ given by

$$\mathbf{E}_2 = \mathbf{e}_2 E_2^0 \cos\left(\omega_2 t\right), \tag{4.1}$$

where $\mathbf{e}_2$ is the polarization unit vector and E_2^0 is the electric field amplitude. The frequency of the probe field (ω_2) is close to resonance with the transition frequency between states $|1\rangle$ and $|2\rangle$ in the quantum dot (ω_{12}) such that $\omega_2 = \omega_{12} + \delta_2$, where δ_2 is the probe field detuning parameter and is a small quantity (i.e., $\delta_2 \ll \omega_{12}$). The second field applied to the nanocomposite system is called the control laser field, and is assumed to couple with the $|1\rangle \leftrightarrow |3\rangle$ transition in the QD. The control laser field has frequency ω_3 and electric field $\mathbf{E}_3$ given by

$$\mathbf{E}_3 = \mathbf{e}_3 E_3^0 \cos\left(\omega_3 t\right). \tag{4.2}$$

Here $\mathbf{e}_3$ and E_3^0 are the polarization unit vector and electric field amplitude of the control field, respectively, and the control field is close to resonance with the $|1\rangle \leftrightarrow |3\rangle$ transition frequency (ω_{13}) in the quantum dot such that $\omega_3 = \omega_{13} + \delta_3$, where $\delta_3 \ll \omega_{13}$.

The probe and control laser fields excite both the QD and graphene nanodisk. In the QD, these fields create excitons (electron-hole pairs) which produce dipole electric fields that interact with the nearby graphene nanodisk. Similarly in the graphene nanodisk, the probe and control laser fields generate surface plasmon polaritons, which produce dipole electric fields that interact with the QD. The dipole electric field produced by the QD at the location of the graphene nanodisk is

$$\mathbf{E}_{DDI}^{QD} = \frac{g_l \mathbf{P}_{QD}}{4\pi\epsilon_b\epsilon_0 R^3}, \tag{4.3}$$

while the dipole electric field produced by graphene at the location of the QD is

$$\mathbf{E}_{DDI}^{G} = \frac{g_l \mathbf{P}_{G}}{4\pi\epsilon_b\epsilon_0 R^3}. \tag{4.4}$$

In the above expressions, $\mathbf{P}_{QD}$ and $\mathbf{P}_G$ are the polarization of the QD and graphene, respectively, while ϵ_b is the dielectric constant of the background medium surrounding the QD-graphene hybrid and g_l ($l = x$, y, or z) is the polarization parameter, with $g_x = g_y = -1$ and $g_z = 2$ for electric fields polarized in the x-y plane or in the z-direction, respectively [44]. In Eq. 4.3, the polarization of the three-level QD $\mathbf{P}_{QD}$ is obtained using the density matrix ρ, which is defined as

$$\rho = \sum_{i=1}^{3} p_i \ket{i}\bra{i}. \tag{4.5}$$

In the above expression, the quantity p_i is the statistical probability that the QD is in the state $\ket{i}$. The density matrix can be used to calculate the expectation value of any observable quantity A using the following relation:

$$\langle A \rangle = Tr\left(\rho A\right). \tag{4.6}$$

Here the polarization (dipole moment) of the QD is calculated as

$$\mathbf{P}_{QD} = \langle \boldsymbol{\mu} \rangle = Tr\left(\rho \boldsymbol{\mu}\right), \tag{4.7}$$

which gives

$$\mathbf{P}_{QD} = \boldsymbol{\mu}_{12}\left(\rho_{12} + \rho_{21}\right) + \boldsymbol{\mu}_{13}\left(\rho_{13} + \rho_{31}\right). \tag{4.8}$$

In the above expression, $\boldsymbol{\mu}_{ij} = \langle i | \boldsymbol{\mu} | j \rangle$ and $\rho_{ij} = \langle i | \rho | j \rangle$ are the transition dipole moment and density matrix element, respectively, for the transition $|i\rangle \leftrightarrow |j\rangle$ in the QD.

The total electric field experienced by the graphene nanodisk is expressed as

$$\mathbf{E}_G = \mathbf{E}_2 + \mathbf{E}_3 + \mathbf{E}_{DDI}^{QD}, \tag{4.9}$$

where the first, second and third terms represent the contributions from the probe laser field, control laser field and the QD dipole field, respectively. Using the quasistatic dipole approximation [44], the polarization of the graphene nanodisk is obtained as

$$\mathbf{P}_G = \epsilon_b \epsilon_0 \alpha \left(\mathbf{E}_2 + \mathbf{E}_3 + \mathbf{E}_{DDI}^{QD} \right), \tag{4.10}$$

where α is the polarizability tensor for the graphene nanodisk given by

$$\alpha = \begin{pmatrix} \alpha_x & 0 & 0 \\ 0 & \alpha_y & 0 \\ 0 & 0 & \alpha_z \end{pmatrix}. \tag{4.11}$$

The elements in the polarizability tensor are obtained as

$$\alpha_l(\omega) = \frac{4\pi d_x d_y d_z \left[\epsilon_g(\omega) - \epsilon_b \right]}{3\epsilon_b + 3L_l \left[\epsilon_g(\omega) - \epsilon_b \right]}, \, l = x, \, y, \, \text{or } z, \tag{4.12}$$

where $\epsilon_g(\omega)$ is the dielectric function of graphene and L_l is called the depolarization factor, which determines the optical response of the graphene nanodisk based on its shape [44]. Here the graphene nanodisk is approximated as a thin oblate spheroid such that $d_x = d_y$ and $d_x > d_z$. In this situation, the depolarization factors for the nanodisk are obtained as

$$L_z = \frac{1 - e_g^2}{e_g^2} \left[\frac{1}{2e_g} \log \left(\frac{1 + e_g}{1 - e_g} \right) - 1 \right] \tag{4.13}$$

and

$$L_x = L_y = \frac{1}{2} \left(1 - L_z \right), \tag{4.14}$$

where $e_g = \sqrt{1 - (d_x/d_z)^2}$ is the eccentricity of the graphene nanodisk. The expression for

65

the polarizability given in Eq. 4.12 has been widely used in the literature to study the optical properties of metallic nanodisks, and has been found to give good agreement with experimental results [45, 46]. The quasistatic approximation may be used when the dimensions of the graphene nanodisk are much smaller than the wavelength of the incident electromagnetic field, which allows one to assume that the nanodisk experiences a spatially uniform but time-varying electric field. Here the wavelengths of light considered are on the order of several hundred nanometers, and thus the size of the graphene nanodisk must be less than 100 nm. It is important to note that the present model is only valid for nano-sized graphene samples and not for bulk materials. Furthermore, higher-order multipole moments (i.e., quadrupole, octopole, etc.) are neglected in the present approximation as they have a neglibile contribution for nano-sized graphene. For a very flat and thin nanodisk such that $L_x \gg L_z$, Eqs. 4.13 and 4.14 reduce to [47, 48]

$$
\begin{aligned}
L_z &\cong 1 - \frac{\pi}{2}\frac{d_z}{d_x} \\
L_x &= L_y \cong \frac{\pi}{4}\frac{d_z}{d_x}
\end{aligned}
\tag{4.15}
$$

The above method has been used to model the optical response of a graphene flake in Ref. [49].

The total electric field felt by the QD is written as

$$
\mathbf{E}_{QD} = \frac{\mathbf{E}_2}{\epsilon_{bd}} + \frac{\mathbf{E}_3}{\epsilon_{bd}} + \frac{g_l\alpha\left(\mathbf{E}_2 + \mathbf{E}_3 + \mathbf{E}_{DDI}^{QD}\right)}{4\pi\epsilon_{bd}R^3},
\tag{4.16}
$$

where the first, second, and third terms represent the contributions from the probe laser field, control laser field, and graphene dipole field, respectively. In the above expression, $\epsilon_{bd} = (2\epsilon_b + \epsilon_d)/3\epsilon_b$, ϵ_d being the dielectric constant of the QD. Using the expression for $\mathbf{E}_{DDI}^{QD}$ from Eq. 4.3, Eq. 4.16 becomes

$$
\begin{aligned}
\mathbf{E}_{QD} &= \frac{\mathbf{E}_2}{\epsilon_{bd}} + \frac{g_l\alpha\mathbf{E}_2}{4\pi\epsilon_{bd}R^3} + \frac{g_l^2\alpha\boldsymbol{\mu}_{12}}{(4\pi)^2\epsilon_b\epsilon_0\epsilon_{bd}R^6}\left(\rho_{12} + \rho_{21}\right) \\
&+ \frac{\mathbf{E}_3}{\epsilon_{bd}} + \frac{g_l\alpha\mathbf{E}_3}{4\pi\epsilon_{bd}R^3} + \frac{g_l^2\alpha\boldsymbol{\mu}_{13}}{(4\pi)^2\epsilon_b\epsilon_0\epsilon_{bd}R^6}\left(\rho_{13} + \rho_{31}\right)
\end{aligned}
\tag{4.17}
$$

Here it is considered that only the probe laser field and its induced dipole fields couple with

the $|1\rangle \leftrightarrow |2\rangle$ transition in the QD, while only the control laser field and its induced dipole fields couple with the $|1\rangle \leftrightarrow |3\rangle$ transition in the QD. This scenario can be realized in the following ways: (a) The probe field $\mathbf{E}_2$ is perpendicular to the dipole moment $\boldsymbol{\mu}_{13}$ and simultaneously the control field $\mathbf{E}_3$ is perpendicular to the dipole moment $\boldsymbol{\mu}_{12}$. (b) The transition frequencies ω_{12} and ω_{13} are very different from each other, meaning that ω_2 is far away from ω_{13} and ω_3 is far away from ω_{12}. Using Eq. 4.17, the interaction Hamiltonian for the QD interacting with the total incident electric field is expressed in the rotating wave approximation as

$$
\begin{aligned}
H_{QD} \;=\; & -\left[\frac{\boldsymbol{\mu}_{12} \cdot \mathbf{e}_2 E_2^0}{2\epsilon_{bd}} + \frac{g_l \boldsymbol{\mu}_{12} \cdot (\alpha \mathbf{e}_2) E_2^0}{8\pi \epsilon_{bd} R^3} + \frac{g_l^2 \boldsymbol{\mu}_{12} \cdot (\alpha \boldsymbol{\mu}_{12})}{(4\pi)^2 \epsilon_b \epsilon_0 \epsilon_{bd} R^6} \rho_{12}\right] \sigma_{12}^+ e^{-i\omega_2 t} + h.c. \quad (4.18) \\
& -\left[\frac{\boldsymbol{\mu}_{13} \cdot \mathbf{e}_3 E_3^0}{2\epsilon_{bd}} + \frac{g_l \boldsymbol{\mu}_{13} \cdot (\alpha \mathbf{e}_2) E_3^0}{8\pi \epsilon_{bd} R^3} + \frac{g_l^2 \boldsymbol{\mu}_{12} \cdot (\alpha \boldsymbol{\mu}_{13})}{(4\pi)^2 \epsilon_b \epsilon_0 \epsilon_{bd} R^6} \rho_{13}\right] \sigma_{13}^+ e^{-i\omega_3 t} + h.c.,
\end{aligned}
$$

where $\sigma_{ij}^+ = |i\rangle \langle j| \; (\sigma_{ij} = |j\rangle \langle i|)$ is the exciton creation (annihilation) operator. The above expression contains terms which describe the dipoles of the QD interacting with the dipole electric field produced by the graphene nanodisk, and vice versa. This interaction is known as the dipole-dipole interaction. The interaction Hamiltonian in Eq. 4.18 is now written in interaction representation in terms of the contributions from the external laser fields and the dipole-dipole interaction as

$$
H_{QD} = H_{QD-F} + H_{QD-DDI}, \tag{4.19}
$$

where

$$
H_{QD-F} = -\hbar\Omega_2 \sigma_{12}^+ e^{-i(\omega_2 - \omega_{12})t} - \hbar\Omega_3 \sigma_{13}^+ e^{-i(\omega_3 - \omega_{13})t} + h.c. \tag{4.20}
$$

and

$$
H_{QD-DDI} = -\hbar\left(\Pi_2 + \Lambda_2 \rho_{12}\right) \sigma_{12}^+ e^{-i(\omega_2 - \omega_{12})t} - \hbar\left(\Pi_3 + \Lambda_3 \rho_{13}\right) \sigma_{13}^+ e^{-i(\omega_3 - \omega_{13})t} + h.c. \tag{4.21}
$$

In the above expressions, parameters are defined as

$$
\Omega_i = \frac{\mu_{1i} E_i^0}{2\hbar\epsilon_{bd}}, \tag{4.22}
$$

$$
\Pi_i = \frac{g_l \alpha_l\left(\omega_i\right) \Omega_i}{4\pi R^3}, \tag{4.23}
$$

and

$$\Lambda_i = \frac{g_l^2 \alpha_l (\omega_i) \mu_{1i}^2}{(4\pi)^2 \hbar \epsilon_b \epsilon_0 \epsilon_{bd} R^6},\tag{4.24}$$

where $i = 2$ or 3.

The interaction Hamiltonian term H_{QD-F} given in Eq. 4.19 represents the direct contribution from the external probe ($i = 2$) and control ($i = 3$) laser fields incident on the QD, and is written in terms of the Rabi frequencies Ω_i which characterize the coupling of these fields with their respective dipole moments in the QD. The second contribution H_{QD-DDI} includes the electric fields incident on the QD due to the dipole-dipole interaction between the QD and the graphene nanodisk, and contains two terms. The first term Π_i is due to the interaction of the QD with the dipole electric fields from the dipoles in the graphene nanodisk induced directly by the probe and control laser fields, and therefore is called the *direct dipole-dipole interaction* term. The second term Λ_i arises from the interaction of the QD with a dipole field from the graphene nanodisk that is created when the polarization of the QD polarizes the graphene nanodisk. In other words, these contributions are the self-interaction of the QD, as they depend on the polarization of the QD. For this reason this term is called the *self-induced dipole-dipole interaction* parameter.

The surface plasmon polariton resonance frequency ω_{sp}^l in the graphene nanodisk is obtained by setting the real part of the denominator in $\alpha_l (\omega)$ equal to zero and solving for ω. When the optical excitation frequencies of the QD lie near the surface plasmon polariton resonance frequencies of the graphene nanodisk (i.e. when $\omega_{1i} \approx \omega_{sp}^l$), the dipole-dipole interaction terms Π_i and Λ_i become very strong due to the enhanced local fields in the vicinity of the graphene nanodisk. This interaction leads to excitation and energy transfer between the QD and graphene.

The combined QD-graphene system is embedded in a photonic crystal consisting of dielectric spheres arranged periodically in three dimensions, which acts as a reservoir for the QD. The excited state $|1\rangle$ spontaneously decays to the lower-energy states $|2\rangle$ and $|3\rangle$ due to excitons coupling with Bloch photons in the photonic crystal (see Figure 4-1). The interaction Hamiltonian for the QD-photonic crystal reservoir coupling is written in the rotating wave approximation

and interaction representation as:

$$H_{QD-PC} = -\sum_{i=2}^{3}\sum_{k}\sqrt{\frac{\hbar\omega_k}{2\epsilon_0\epsilon_b V_{PC}}}\left(\mathbf{e}_k\cdot\boldsymbol{\mu}_{1i}\right)a_k\sigma_{1i}^{+}e^{-i(\omega_k-\omega_{1i})t} + h.c., \tag{4.25}$$

where $\mathbf{e}_k$ is the polarization unit vector of the Bloch photons in the photonic crystal and V_{PC} is the volume of the photonic crystal. The operator a_k^{+} (a_k) is the photon creation (annihilation) operator, while ω_k and k are the Bloch photon frequency and wave vector, respectively.

Using Eqs. 4.19 and 4.25, total interaction Hamiltonian of the system is written as

$$\begin{aligned} H_{int} &= H_{QD-F} + H_{QD-DDI} + H_{QD-PC} \tag{4.26}\\ &= -\sum_{i=2}^{3}\hbar\left(R_i e^{i\theta_i} + \Lambda_i\rho_{1i}\right)\sigma_{1i}^{+}e^{-i(\omega_i-\omega_{1i})t} + h.c.\\ &\quad -\sum_{i=2}^{3}\sum_{k}\sqrt{\frac{\hbar\omega_k}{2\epsilon_0\epsilon_b V_{PC}}}\left(\mathbf{e}_k\cdot\boldsymbol{\mu}_{1i}\right)a_k\sigma_{1i}^{+}e^{-i(\omega_k-\omega_{1i})t} + h.c., \tag{4.27} \end{aligned}$$

where

$$R_i = \sqrt{[\Omega_i + \mathrm{Re}(\Pi_i)]^2 + [\mathrm{Im}(\Pi_i)]^2} \tag{4.28}$$

and

$$\theta_i = \arctan\left[\frac{\mathrm{Im}(\Pi_i)}{\Omega_i + \mathrm{Re}(\Pi_i)}\right]. \tag{4.29}$$

The density matrix method is used to evaluate the energy transfer between the QD and the graphene. Using the interaction Hamiltonian given in Eq. 4.26 and the master equation method [39], the equation of motion for the density matrix is written as

$$\frac{d\rho}{dt} = -\frac{i}{\hbar}[H_{QD-F} + H_{QD-DDI}, \rho] + \mathcal{L}\rho, \tag{4.30}$$

where

$$\mathcal{L}\rho = -\Gamma_{21}\left(\sigma_{11}\rho + \rho\sigma_{11} - 2\rho_{11}\sigma_{22}\right) - \Gamma_{31}\left(\sigma_{11}\rho + \rho\sigma_{11} - 2\rho_{11}\sigma_{33}\right). \tag{4.31}$$

The equations of motion for the QD density matrix elements ρ_{ij} are then obtained using Eq.

4.30 as

$$\frac{d\rho_{22}}{dt} = 2\Gamma_{21}\rho_{11} - iR_2 e^{i\theta_2}\rho_{21} - i\Lambda_2\rho_{12}\rho_{21} + iR_2 e^{-i\theta_2}\rho_{12} + i\Lambda_2^*\rho_{21}\rho_{12} \tag{4.32}$$

$$\frac{d\rho_{33}}{dt} = 2\Gamma_{31}\rho_{11} - iR_3 e^{i\theta_3}\rho_{31} - i\Lambda_3\rho_{13}\rho_{31} + iR_3 e^{-i\theta_3}\rho_{13} + i\Lambda_3^*\rho_{31}\rho_{13} \tag{4.33}$$

$$\frac{d\rho_{12}}{dt} = -d_{12}\rho_{12} + iR_3 e^{i\theta_3}\rho_{32} + i\Lambda_3\rho_{13}\rho_{32} - iR_2 e^{-i\theta_2}(\rho_{11} - \rho_{22}) \tag{4.34}$$

$$\frac{d\rho_{13}}{dt} = -d_{13}\rho_{13} + iR_2 e^{i\theta_2}\rho_{23} + i\Lambda_2\rho_{12}\rho_{23} - iR_3 e^{i\theta_3}(\rho_{11} - \rho_{33}) \tag{4.35}$$

$$\frac{d\rho_{23}}{dt} = -i(\delta_2 - \delta_3)\rho_{23} + iR_2 e^{-i\theta_2}\rho_{13} + i\Lambda_2^*\rho_{21}\rho_{31} - iR_3 e^{i\theta_3}\rho_{21} - i\Lambda_3\rho_{13}\rho_{21} \tag{4.36}$$

where

$$d_{1i} = \Gamma_{21} + \Gamma_{31} - \Gamma_{id} - i\Delta_{id} - i\delta_i, \tag{4.37}$$

$$\delta_i = \omega_i - \omega_{1i}.$$

Here δ_i are the detuning of the probe $(i = 2)$ and control $(i = 3)$ fields. Note that the diagonal elements of the density matrix satisfy the relation $\rho_{11} + \rho_{22} + \rho_{33} = 1$. The quantities Γ_{id} and Δ_{id} are the *non-radiative decay rate* and *energy shift*, respectively, due to self-induced dipole-dipole interaction parameters Λ_i. They are found as

$$\Gamma_{id} = \text{Im}(\Lambda_i)(\rho_{ii} - \rho_{11}), \tag{4.38}$$

$$\Delta_{id} = \text{Re}(\Lambda_i)(\rho_{ii} - \rho_{11}).$$

The parameters Γ_{i1} represent the spontaneous decay rates of excited state $|1\rangle$ to state $|i\rangle$ due to the Bloch photons in the photonic crystal, and are given as

$$\Gamma_{i1} = \Gamma_{i1}^0 \frac{\pi^2 c^3}{V_{PC}\omega_{1i}^2} D(\omega_{1i}), \tag{4.39}$$

where

$$D(\omega) = \sum_{\pm} \sin\left[\frac{2\omega}{c}(n_a a \pm n_b b)\right] \frac{(n_a \pm n_b)^2 (n_a a \pm n_b b) V_{PC} \arccos^2[F(\omega)]}{2\pi^2 L^3 c n_a n_b \sqrt{1 - F^2(\omega)}}, \tag{4.40}$$

70

and

$$F(\omega) = \sum_{\pm} \pm \frac{(n_a \pm n_b)^2}{4 n_a n_b} \cos\left[\frac{2\omega}{c} \left(n_a a \pm n_b b\right)\right]. \tag{4.41}$$

In the above expression, Γ_{i1}^0 is the exciton decay rate due to the background radiation field in free space. Here $L = 2a + 2b$ is the photonic crystal lattice constant, $2b$ is the spacing between dielectric spheres and a is the radius of the spheres. Parameters n_a and n_b denote the refractive index of the dielectric spheres and background material in the photonic crystal, respectively. The expression for the photonic density of states $D(\omega)$ has been derived in Ref. [50]. Here the Markovian approximation has been used in order to derive the decay rates for the QD in the presence of the photonic crystal. This approximation ignores memory effects in the electromagnetic reservoir due to the presence of the QD, and is valid when the photonic density of states can be considered smooth and slowly-varying compared to the energy difference between the edge of the photonic band gap and the resonance frequency of the QD [51]. Note that the present calculations fall within the regime for which the Markovian approximation is valid. Therefore the effect of the photonic crystal serves only to alter the decay rates of the excitonic transitions compared to those in free space. The density matrix equations of motion given in Eqs. 4.32–4.36 are solved numerically by first substituting $\rho_{12} = \widetilde{\rho}_{12} e^{i\theta_2}$, $\rho_{13} = \widetilde{\rho}_{13} e^{i\theta_3}$ and $\rho_{23} = \widetilde{\rho}_{23} e^{-i(\theta_2 - \theta_3)}$.

Following the method of Ref. [44] and using Eq. 4.26, the energy absorption rate of the QD (W_{QD}) and the energy transfer rate from the QD to graphene (W_G) are found as

$$W_{QD} = \sum_{i=2}^{3} \hbar \omega_{1i} \rho_{11} \Gamma_{i1} \tag{4.42}$$

$$W_G = \sum_{i=2}^{3} \frac{g_l^2 \mu_{1i}^2 \omega_i \, \text{Im}(\alpha_l) \, |\widetilde{\rho}_{1i}|^2}{8\pi^2 \epsilon_b \epsilon_0 \epsilon_{bd}^2 \, |\epsilon_{bg}|^2 \, R^6} \tag{4.43}$$

where $\epsilon_{bg} = (2\epsilon_b + \epsilon_g)/3\epsilon_b$. The expression for W_{QD} is obtained by assuming that the power radiated from the QD is equal to its energy absorption rate. Similar expressions have been widely used in the literature on hybrid systems [2, 3]. Note that the energy transfer to graphene depends on the coherences $\widetilde{\rho}_{1i}$ of the QD density matrix, which change depending on the center-to-center distance between the QD and graphene, R. Therefore Eq. 4.43 does not simply depend on R^6, but rather is a much more complicated function of R.

If a ladder-type three-level quantum emitter is considered, the density matrix equations of motion take a different form. In this case, states $|1\rangle$, $|2\rangle$ and $|3\rangle$ denote the ground, first excited and second excited states, respectively. The probe field with amplitude E_2^0 and frequency ω_2 is coupled between states $|1\rangle$ and $|2\rangle$, while the control field with amplitude E_3^0 and frequency ω_3 is coupled between states $|2\rangle$ and $|3\rangle$. The decay of level $|2\rangle$ to level $|1\rangle$ (level $|3\rangle$ to level $|2\rangle$) is given as Γ_{21} (Γ_{32}). Using the same methods as for the lambda-type system, the density matrix equations of motion for the ladder-type energy level configuration are obtained as

$$
\begin{aligned}
\frac{d\rho_{22}}{dt} &= -\Gamma_{21}\rho_{22} + \Gamma_{32}\rho_{33} + iR_2 e^{-i\theta_2}\rho_{21} + i\Lambda_2^*\rho_{12}\rho_{21} - iR_2 e^{i\theta_2}\rho_{12} - i\Lambda_2\rho_{21}\rho_{12} \quad (4.44)\\
&\quad -iR_3 e^{-i\theta_3}\rho_{32} - i\Lambda_3^*\rho_{23}\widetilde{\rho}_{32} + iR_3 e^{i\theta_3}\rho_{23} + i\Lambda_3\rho_{32}\rho_{23}\\
\frac{d\rho_{33}}{dt} &= -\Gamma_{32}\rho_{33} + iR_3 e^{-i\theta_3}\rho_{32} + i\Lambda_3^*\rho_{23}\rho_{32} - iR_3 e^{i\theta_3}\rho_{23} - i\Lambda_3\rho_{32}\rho_{23} \quad (4.45)\\
\frac{d\rho_{21}}{dt} &= d_{21}\rho_{21} + iR_2 e^{i\theta_2}\left(\rho_{22} - \rho_{11}\right) - iR_3 e^{-i\theta_3}\rho_{31} - i\Lambda_3^*\rho_{23}\rho_{31} \quad (4.46)\\
\frac{d\rho_{32}}{dt} &= d_{32}\rho_{32} + iR_3 e^{i\theta_3}\left(\rho_{33} - \rho_{22}\right) + iR_2 e^{-i\theta_2}\rho_{31} + i\Lambda_2^*\rho_{12}\rho_{31} \quad (4.47)\\
\frac{d\rho_{31}}{dt} &= \left(i\delta_2 + i\delta_3 - \Gamma_{32}\right)\rho_{31} - iR_3 e^{i\theta_3}\rho_{21} - i\Lambda_3\rho_{32}\rho_{21} + iR_2 e^{i\theta_2}\rho_{32} + i\Lambda_2\rho_{21}\rho_{32} \quad (4.48)
\end{aligned}
$$

where

$$
\begin{aligned}
d_{21} &= i\delta_2 + i\Delta_{2d} - \Gamma_{21} - \Gamma_{2d} \quad (4.49)\\
d_{32} &= i\delta_3 + i\Delta_{3d} - \Gamma_{32} - \Gamma_{3d}
\end{aligned}
$$

and

$$
\begin{aligned}
\Delta_{2d} &= \mathrm{Re}\left(\Lambda_2\right)\left(\rho_{22} - \rho_{11}\right) \quad (4.50)\\
\Gamma_{2d} &= \mathrm{Im}\left(\Lambda_2\right)\left(\rho_{22} - \rho_{11}\right)\\
\Delta_{3d} &= \mathrm{Re}\left(\Lambda_3\right)\left(\rho_{33} - \rho_{22}\right)\\
\Gamma_{3d} &= \mathrm{Im}\left(\Lambda_3\right)\left(\rho_{33} - \rho_{22}\right)
\end{aligned}
$$

In the above expressions, all quantities are the same as given previously for the lambda-type system but with the substitutions $\omega_{13} \to \omega_{23}$, $\mu_{13} \to \mu_{23}$ and $\Gamma_{31} \to \Gamma_{32}$. The QD energy

absorption rate and the power transfer in this system are calculated using Eqs. 4.42 and 4.43 with the substitutions $\rho_{11} \rightarrow \rho_{ii}$, $\rho_{13} \rightarrow \rho_{23}$.

4.3   Results and Discussion

In the literature, it is reported that the size of the graphene nanodisk should not be less than 10 nm in diameter in order for edge effects to be neglected [52]. Here a graphene nanodisk with a diameter of 14 nm is considered. The thickness of the nanodisk is taken as $d_z = 0.35$ nm, corresponding to a single graphene layer, and its size ratio is $d_x/d_z = 20$. The plasmon frequency and background dielectric constant of graphene are taken from experiments as 6.02 eV and 1.964, respectively [21]. The decay rate in graphene is taken as $\gamma_G = 5$ THz, which is consistent with the relaxation rates reported in Refs. [22] and [26]. With these parameters, the surface plasmon resonance frequencies in the graphene nanodisk are calculated as $\hbar\omega_{sp}^x = 0.8026$ eV and $\hbar\omega_{sp}^z = 4.1250$ eV.

The QD dielectric constant and dipole moments are taken as $\epsilon_d = 12$ and $\mu_{12} = \mu_{13} = 0.1$ $e \times$ nm, respectively, while the free space decay rates for the QD are taken as $\Gamma_{21}^0 = \Gamma_{31}^0 = 0.2$ μeV. These parameters are comparable to those commonly found in the literature for QDs [2-4]. Here the transition energies in the QD are taken to lie near the plasmon resonance $\hbar\omega_{sp}^x$ as $\hbar\omega_{12} = 0.8046$ eV and $\hbar\omega_{13} = 0.8036$ eV.

The combined QD-graphene nanodisk hybrid is contained within a photonic crystal made of polystyrene spheres arranged periodically in air. Similar photonic crystals have been fabricated by Liu et al. [9], in which ultrafast all-optical switching was experimentally demonstrated. Photonic crystal parameters are taken as $a = 170$ nm, $L = 480$ nm, $n_a = 1.59$ and $n_b = 1$. With these parameters, the photonic band gap of the photonic crystal appears between frequencies 0.8225 eV and 0.9843 eV. Note that the lower edge of the band gap lies near ω_{sp}^x and the QD transition frequencies ω_{12} and ω_{13}. The vacuum decay rates for the QD are taken as $\Gamma_2^0 = \Gamma_3^0 = 0.2$ μeV, and in the presence of the photonic crystal it is found that $\Gamma_{21} = 1.1370$ μeV and $\Gamma_{31} = 1.1127$ μeV. Here the background dielectric constant was taken as $\epsilon_b = 2.081$. Throughout the following calculations, it is considered that the intensity of the probe and control fields are 1.0 and 3.0 W/cm^2, respectively.
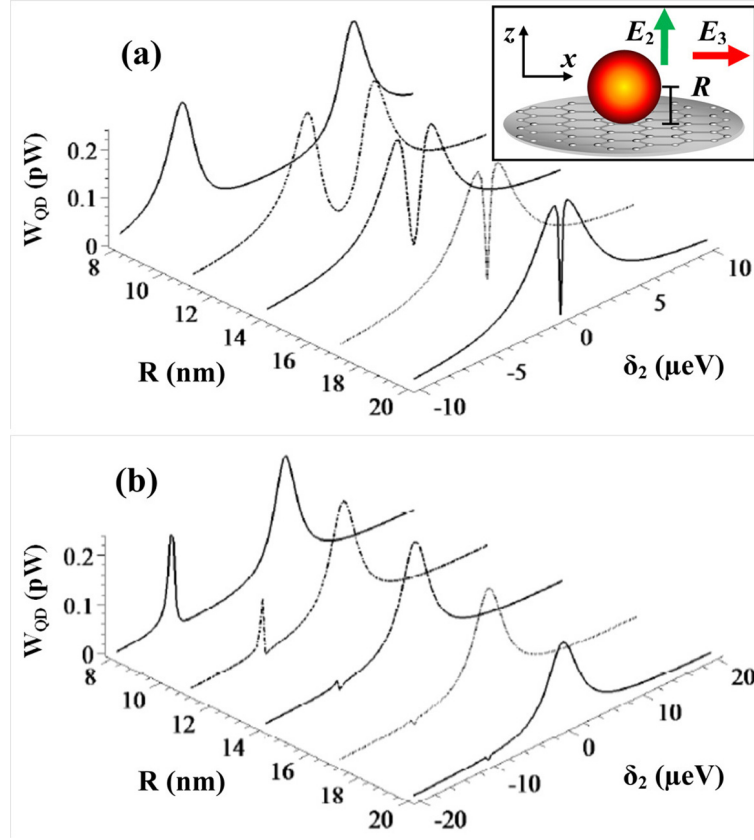
Figure 4-2: Energy absorption rate of the QD as a function of probe field detuning δ_2 when the QD-graphene nanodisk separation R is varied. (a) $\delta_3 = 0$; (b) $\delta_3 = 10$ μeV. Inset: Polarization of the probe and control fields.

Initially it is considered that the excitonic transition $|3\rangle \leftrightarrow |1\rangle$ is coupled with the surface plasmon resonance of the graphene nanodisk. In this configuration, the transition frequency ω_{13} is near ω_{sp}^x while both the control field $\mathbf{E}_3$ and the transition dipole moment $\boldsymbol{\mu}_{13}$ are polarized in the x-y plane. Conversely, the transition $|2\rangle \leftrightarrow |1\rangle$ is not coupled with the graphene nanodisk. This situation occurs when the probe field $\mathbf{E}_2$ and transition dipole moment $\boldsymbol{\mu}_{12}$ are polarized in the z-direction and ω_{12} is far away from ω_{sp}^z (see Figure 4-2 inset). The energy absorption rate in the QD is evaluated from Eq. 4.42 and the results are presented in Figure 4-2(a) when the QD-graphene separation R is varied and the control field is resonant with the $|3\rangle \leftrightarrow |1\rangle$ transition such that $\delta_3 = 0$. It is found that the power absorption spectrum has a single peak with an extremely narrow transparent window at $\delta_2 = 0$ when the QD and graphene are further

away with each other (i.e., $R = 20$ nm). This narrow minimum is due to electromagnetically induced transparency in the system. When the QD is close to graphene (i.e., $R = 8$ nm) the power absorption peak splits into two peaks and a clear minimum appears at $\delta_2 = 0$. The observed splitting is due to the dipole-dipole interaction and surface plasmon coupling.

The splitting of the power absorption spectrum can be explained using the theory of dressed states. When the QD is close to the graphene nanodisk there is strong coupling due to the dipole-dipole interaction for the transition $|3\rangle \leftrightarrow |1\rangle$. This causes the excited state $|1\rangle$ to split into two dressed states, namely $|1_+\rangle$ and $|1_-\rangle$. Therefore, there are now two transitions $|2\rangle \leftrightarrow |1_+\rangle$ and $|2\rangle \leftrightarrow |1_-\rangle$ which give two peaks and a minimum in the spectrum. In other words, a single exciton splits into two dressed excitons, and their energy difference is found to be proportional to the dipole-dipole interaction. As the distance between the QD and graphene increases, the splitting decreases since the direct dipole-dipole interaction term Π_i is inversely proportional to R^3. In Figure 4-2(b) the energy absorption rate is plotted for various values of R when the control field is detuned such that $\delta_3 = 10$ μeV. Here the power absorption spectrum has one peak and negligible electromagnetically-induced transparency when R is large. When R decreases, the single peak splits into two peaks due to the dipole-dipole interaction. These results show that the dipole-dipole interaction can be used to split one exciton into two excitons, and also to control the electromagnetically-induced transparency phenomenon.

In Figure 4-3 the effect of the photonic crystal has been investigated on the energy absorption rate in the lambda-type QD. Initially, the lower band edge of the photonic crystal lies far away from the resonance energies of the QD (see solid curve), and there is weak coupling between the QD and photonic crystal. When the lower photonic band edge is moved closer to the resonance frequency ω_{13} of the QD, the two peaks in the power absorption spectrum merge into a broad peak with a narrow electromagnetically-induced transparency window at $\delta_2 = 0$ (see dashed curve). Note also that the height of the peaks decreases. The merging of the split peaks in the QD power absorption spectrum occurs because the spontaneous decay rates become larger than the dipole-dipole interaction splitting for the two peaks. The value of the decay rate is large because the photonic density of states is large when the resonance energy of the QD lies near the band edges. For example, it is found that $\Gamma_{21} = 6.40$ μeV and $\Gamma_{31} = 3.81$ μeV whereas the energy splitting is about 2.80 μeV. Here, the location of the photonic crystal band edges can be
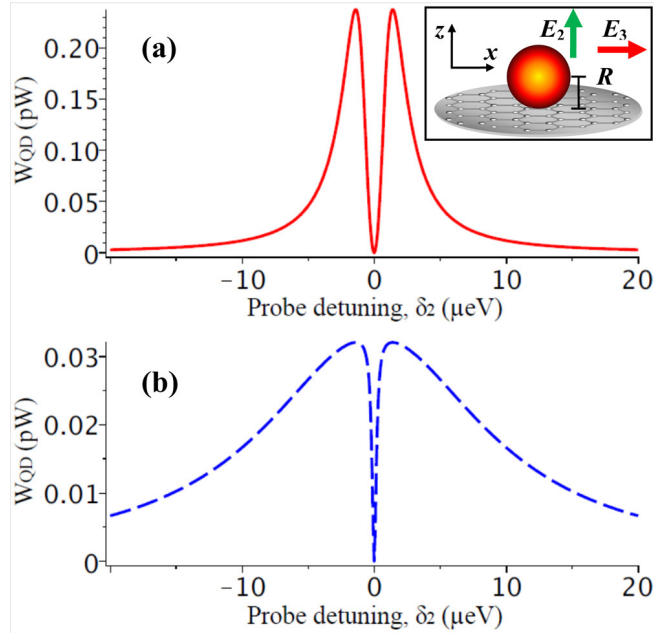
Figure 4-3: Energy absorption rate in the QD as a function of probe field detuning δ_2 when the lower band edge of the photonic crystal is taken as $\varepsilon_v = \hbar\omega_{12} + 17.88$ meV (a) and $\varepsilon_v = \hbar\omega_{12} + 0.56$ meV (b). Here $R = 13$ nm and $\delta_3 = 0$. Inset: Polarization of the probe and control fields.

changed by applying an intense pulsed laser field. The intense laser field causes the refractive index of polystyrene, a material with a strong and fast nonlinear optical response, to change due to the Kerr effect. This change is quantified by the expression $n'_a = n_a + n_3 I_{pump}$ where n_3 is the Kerr nonlinearity constant and has the value $n_3 = 1.15 \times 10^{-12}$ cm^2/W for polystyrene [10]. For the pump field intensity $I_{pump} = 31.0$ GW/cm^2 it is found that the photonic crystal band edge shifts such that $\Delta\varepsilon_v = -17.32$ meV. This means that the hybrid system can be used to study the nonlinear properties of photonic crystals. Using an external pump field to induce a large Kerr nonlinearity in the polystyrene photonic crystal is also an effective way to switch the energy transfer between two states; from high to low energy transfer peaks. Alternatively, the refractive index of the background material in the photonic crystal can also be modified by immersing the photonic crystal in another material. Therefore the present QD-graphene system can also be used as a nano-sensor.

The energy transfer rate from the QD to graphene is plotted in Figure 4-4 as a function of the
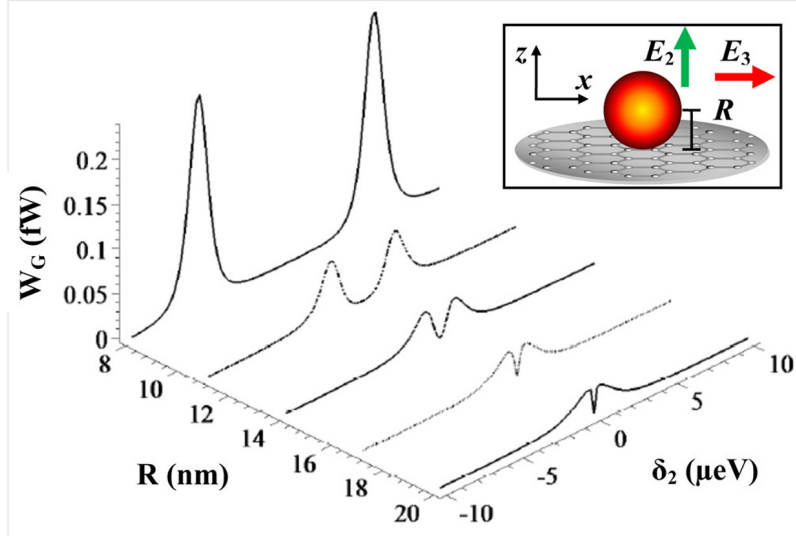
Figure 4-4: Energy transfer rate from the QD to graphene as a function of probe field detuning δ_2 when the QD-graphene nanodisk separation R is varied and $\delta_3 = 0$. Inset: Polarization of the probe and control fields.

probe field detuning when the QD-graphene separation R is varied. It is found that the power transfer spectrum has a single peak with a narrow electromagnetically-induced transparency window when R is large (i.e., $R = 20$ nm). When the QD is brought closer to graphene (i.e., $R = 8$ nm), the power transfer spectrum has one large minimum and two peaks with separation proportional to the DDI. This indicates that energy is transferred from the QD to the graphene when the two dressed excitons created in the QD are absorbed by graphene. This is an interesting finding, and can be used to transfer energy absorbed by the QD from a light source (i.e., the sun) to graphene where it can be stored. Therefore, one can fabricate energy transfer and storage devices (i.e., solar cells) from the present hybrid system.

It is also found that the height of the energy transfer peaks increases as the QD-graphene separation decreases (see Figure 4-4). This effect has been observed experimentally by Chen et al. [31] and Dong et al. [32]. They found that as the distance between CdTe-QDs and a graphene oxide sheet decreases there is a strong quenching of the QD fluorescence. They concluded that the fluorescence quenching could be due the energy transfer from the QD to the graphene sheet. For example, Chen et al. [31] deposited graphene on quartz substrates and then CdSe/ZnS-QDs

were deposited on graphene. The fluorescence measurements were performed on the individual QDs located both on the bare quartz substrate and on a graphene layer. They observed strong fluorescence quenching for QDs deposited on the graphene sheet, which was attributed to the energy transfer between QD and graphene and not due to photoinduced electron transfer from the QD to graphene. Similarly Wang et al. [33] performed photoluminescence measurements on CdS–QDs and ZnS–QDs on graphene and observed a strong quenching of photoluminescence for these QDs due to the presence of the graphene sheet. They also performed transient photovoltaic experiments on their hybrid systems and found a very unexpected strong positive photovoltaic response due to the dipole-dipole interaction. Conversely, it was found that separate samples of graphene and CdS-QDs of a similar size do not show any photovoltaic response. They concluded their experimental findings can be explained due to the energy transfer between the QD and the graphene sheet. Similar energy transfer between a QD and carbon nanotube has also been found experimentally by Shafran et al. [34].

When a QD is in contact with biomolecules, molecular beacons, DNA or aptamers, its dielectric constant can be modified. Therefore, the role of the dielectric constant of the QD on the energy transfer to graphene has been investigated. The results are plotted in Figure 4-5(a) for three values of ϵ_d. It is found that by changing the dielectric constant of the QD, the height of the energy transfer peaks can be modified. For example by increasing or decreasing the dielectric constant, the height of the energy transfer spectra decreases or increases, respectively. This is because the the energy transfer is inversely proportional to the square of the dielectric constant, as shown by Eq. 4.43. This effect has also been verified experimentally by Dong et al. [32], where upon integrating a molecular beacon to a CdTe-QD it was found that the fluorescence quenching due to graphene is modified. Note also that at certain values of probe detuning, say for example $\delta_2 \approx \pm 1.5$ μeV, the sensitivity of the energy transfer rate to the change in dielectric constant is quite high. This is an interesting finding, particularly if one considers that the present hybrid system can be used to fabricate nano-biosensors.

In Figure 4-5(b) the energy transfer rate to graphene is plotted when a single graphene layer or two layers are considered. Here the ratio $d_x/d_z = 20$ is preserved in order to keep the surface plasmon polariton resonance frequency constant. Note that for two layers of graphene the height of the energy transfer peak increases. As additional layers of graphene are added, its volume
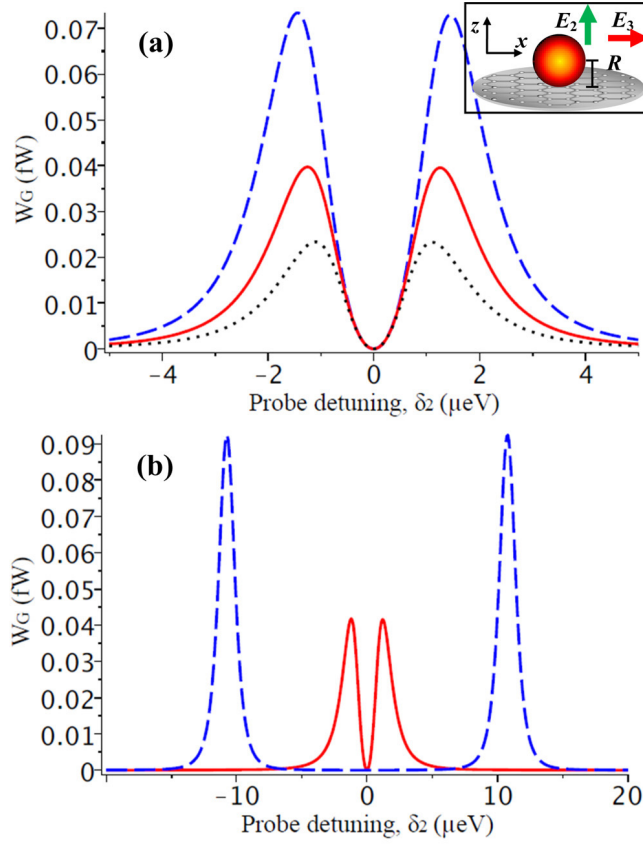
Figure 4-5: (a) Energy transfer rate from the QD to graphene when the dielectric function of the QD is taken as $\epsilon_d = 10$ (dotted curve), 12 (solid curve) and 14 (dashed curve). Here $R = 13$ nm and $\delta_3 = 0$. (b) Energy transfer rate from the QD to graphene when the thickness of graphene is varied between one layer (solid curve) or two (dashed curve). Here $R = 13$ nm and $\delta_3 = 0$. Inset: Polarization of the probe and control fields.

increases. In turn, the dipole-dipole interaction between the QD and graphene is enhanced. Therefore, both the height of the peaks in the energy transfer spectrum and their splitting are increased. This effect has also been verified experimentally by Chen et al. [31], where it was found that increasing the number of graphene layers in a CdSe/ZnS nanocrystal-graphene composite system enhanced the QD fluorescence quenching effect.

An alternative configuration for the QD-graphene nanocomposite system is also considered, where both transitions $|2\rangle \leftrightarrow |1\rangle$ and $|3\rangle \leftrightarrow |1\rangle$ couple with the surface plasmons in the graphene nanodisk. In this configuration, both ω_{12} and ω_{13} are close to ω_{sp}^x and the transition dipole
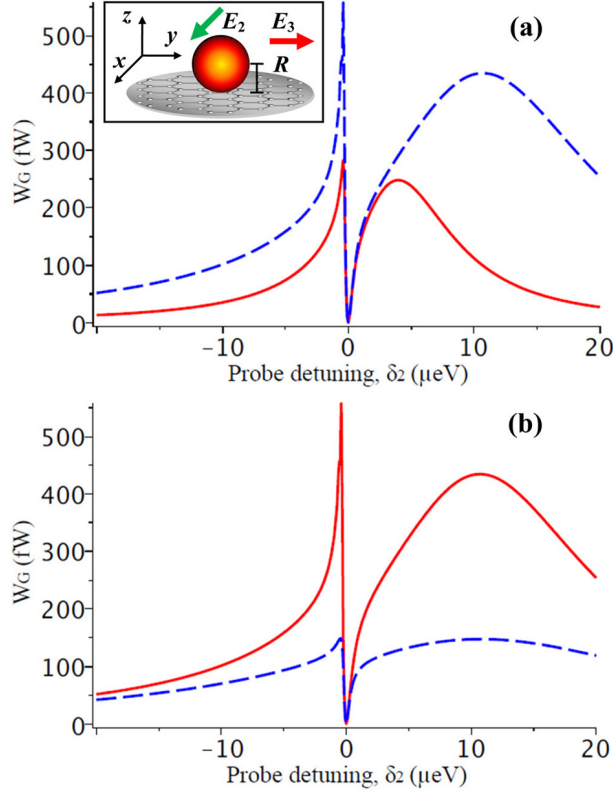
Figure 4-6: Energy transfer rate from the QD to graphene as a function of probe detuning δ_2 for the second configuration of dipole moments and fields (see inset). (a) The QD-graphene separation is varied from $R = 13$ nm (solid curve) to $R = 11$ nm (dashed curve). (b) $R = 11$ nm and the lower band edge of the photonic crystal is taken as $\varepsilon_v = \hbar\omega_{12} + 17.88$ meV (solid curve) and $\varepsilon_v = \hbar\omega_{12} + 0.56$ meV (dashed curve). Here $\delta_3 = 0$. Inset: Polarization of the probe and control fields.

moments (electric fields) $\boldsymbol{\mu}_{12}$ ($\mathbf{E}_2$) and $\boldsymbol{\mu}_{13}$ ($\mathbf{E}_3$) are aligned along the x- and y-directions, respectively. In Figure 4-6(a), the energy transfer rate from the QD to graphene is plotted as a function of the probe field detuning while varying R. Here the physical parameters are the same as those considered in previous calculations. Note that two peaks appear due to the dipole-dipole interaction as in the first configuration considered. Previously the two peaks were symmetric, but in this case they are asymmetric. This is due to the self-induced dipole-dipole interaction parameter Λ_2, which causes both peaks to shift towards positive detuning due to the change in the effective probe field detuning from δ_2 to $\delta_2 + \Delta_{2d}$, as shown in Eq. 4.34. Here also the width of both peaks increases due to the non-radiative decay Γ_{2d}. In the previous

80
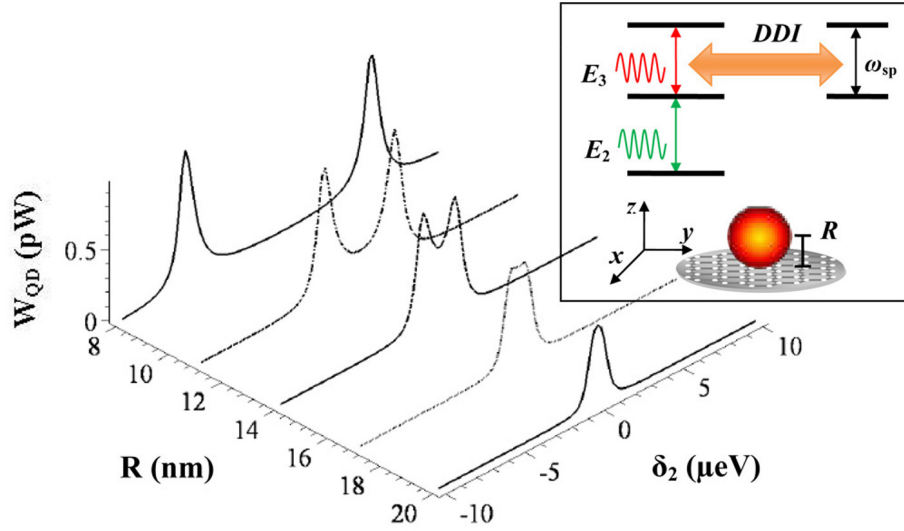
Figure 4-7: Energy absorption rate of to the ladder-type QD as a function of probe field detuning δ_2 when the QD-graphene nanodisk separation R is varied. Here $\hbar\omega_{23} = 0.8036$ eV and the intensities of the probe and control fields are 1.0 and 3.0 W/cm^2, respectively. Other parameters are the same as considered previously. Inset: Schematic of the QD-graphene hybrid system with ladder-type energy level structure. Here DDI coupling occurs only for the $|2\rangle \leftrightarrow |3\rangle$ transition.

configuration the self-induced dipole-dipole interaction parameter Λ_2 was zero because there was no coupling between the QD transition $|2\rangle \leftrightarrow |1\rangle$ and graphene. These effects are enhanced by decreasing R.

In Figure 4-6(b) the effect of the photonic crystal is investigated in the same way as in Figure 4-3, and similar results are found as for the previous configuration. By applying an external pump laser field to the polystyrene photonic crystal, the power transfer to graphene can be switched from high to low values. Note that due to the asymmetry of the power transfer spectrum in this configuration, the sensitivity of this switching effect can change drastically depending on the value of probe field detuning. For example, negative detunings close to $\delta_2 = 0$ show a sharp peak in the energy transfer spectrum when the pump field is absent, and this peak is suppressed when the pump field is applied.

Finally, the energy absorption rate in a ladder-type QD coupled with the graphene nanodisk is investigated. Here it is considered that the control field is coupled with the QD transition $|2\rangle \leftrightarrow |3\rangle$ and the graphene nanodisk, while the probe field is only coupled to the QD transition
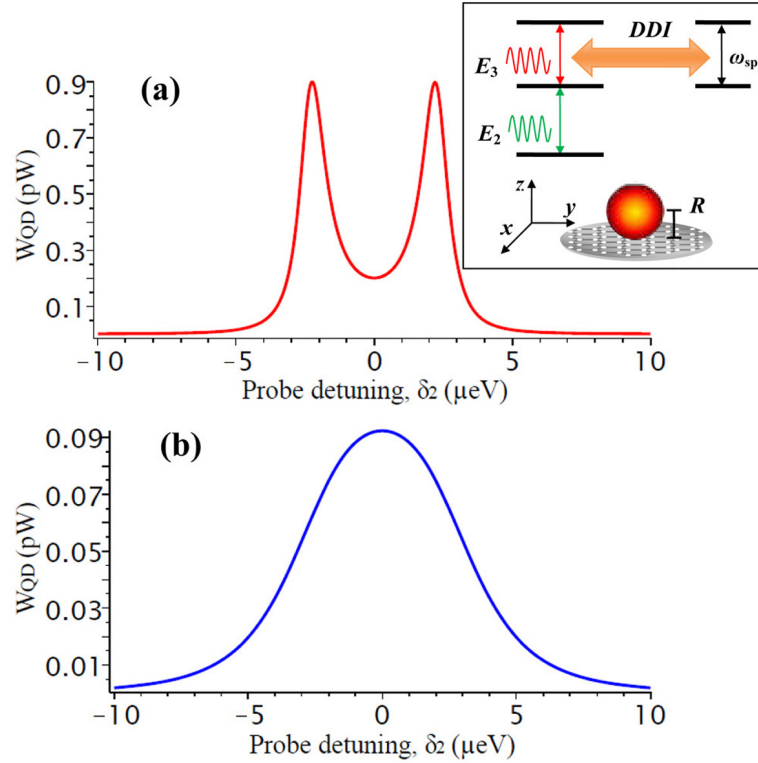
Figure 4-8: Energy absorption rate of the ladder-type QD as a function of the probe field detuning δ_2 when the lower band edge of the photonic crystal is taken as (a) $\varepsilon_v = \hbar\omega_{23} + 17.88$ meV and (b) $\varepsilon_v = \hbar\omega_{23} + 0.10$ meV. Here $R = 10$ nm, $\delta_3 = 0$ and other parameters are the same in Figure 4-7. Inset: Schematic diagram of the QD-graphene hybrid system with ladder-type energy level structure. Here the dipole-dipole coupling occurs only for the $|2\rangle \leftrightarrow |3\rangle$ transition.

$|1\rangle \leftrightarrow |2\rangle$. This situation can occur when the resonance frequency ω_{23} lies near ω_{sp}^x, while ω_{12} is uncoupled from both ω_{sp}^x and ω_{sp}^z. Note that this configuration is analogous to that explored in Figure 4-2 for the lambda-type QD.

In Figure 4-7 the energy absorption rate in the ladder-type QD is plotted when the QD-graphene nanodisk separation R is varied. It is found that the power absorption spectrum gives two peaks and a minimum when R is small (i.e., $R = 8$ nm), as was found in Figure 4-2. Note that for the ladder-type QD, the narrow minimum due to electromagnetically induced transparency does not appear. This is because the same electromagnetically induced transparency effect does not appear in ladder-type systems [39].

The effect of the photonic crystal on the energy absorption rate in the ladder-type QD has

also been investigated, and the results are shown in Figure 4-8. Once again a pump field of intensity 31.0 GW/cm^2 is applied, which causes the photonic crystal band edge to shift and increases the decay rate of the QD. Note that the power absorption spectrum merges into a broad peak in the same way as it did for the lambda-type QD (see Figure 4-3(b)). Here, however, the narrow minimum present in the lambda-type QD is absent and two peaks merge into one.

4.4 Conclusions

In this chapter, the dipole-dipole interaction and energy transfer have been investigated in a quantum dot (QD)-graphene nanodisk system embedded within a photonic crystal. The results indicate that in this system, multiple excitonic states (dressed states) can be created in the quantum dot and then transferred to graphene with different frequencies. This phenomenon occurs purely due to the dipole-dipole interaction between the QD and graphene, and results in energy transfer.

It is demonstrated that the energy absorption of the QD and/or the energy transfer from the QD to graphene can be switched on and off by changing the strength of the dipole-dipole interaction or by applying an intense external laser field to the photonic crystal. The findings presented in this chapter also agree qualitatively with recent experimental observations on the energy transfer in QD-graphene nanocomposite systems.

The results of the numerical simulations presented here provide motivation for future experimental and theoretical investigations on nanocomposites made from graphene, carbon nanotubes, quantum dots and photonic crystals. The present theory can be applied to hybrid systems consisting of graphene with quantum emitters such as quantum dots, nanocrystals, atoms and chemical or biological molecules; the only requirement is the quantum emitter should have at least three states. The proposed nanocomposite system can be used to fabricate nano-sensors, all optical nano-switches, energy transfer devices and energy storage devices.

Bibliography

[1] M. Achermann, *J. Phys. Chem. Lett.* **1**, 2837 (2010).

[2] R. D. Artuso and G. W. Bryant, *Phys. Rev. B* **82**, 195419 (2010).

[3] S. M. Sadeghi, L. Deng, X. Li, and W.-P. Huang, *Nanotechnology* **20**, 365401 (2009).

[4] M.-T. Cheng, S.-D. Liu, H.-J. Zhou, Z.-H. Hao, and Q.-Q. Wang, *Opt. Lett.* **32**, 2125 (2007).

[5] M. Durach, A. Rusina, V. I. Klimov, and M. I. Stockman, *New J. Phys.* **10**, 105011 (2008).

[6] J. M. Luther, P. K. Jain, T. Ewers, and A. P. Alivisatos, *Nat. Mater.* **10**, 361 (2011).

[7] J. D. Joannopoulos, S. G. Johnson, J. N. Winn, and R. D. Meade, *Photonic Crystals: Molding the Flow of Light*, 2nd ed. (Princeton University Press, Princeton, New Jersey, 2008).

[8] A. Chutinan, S. John, and O. Toader, *Phys. Rev. Lett.* **90**, 123901 (2003).

[9] Y. Liu, F. Qin, Z.-Y. Wei, Q.-B. Meng, D.-Z. Zhang, and Z.-Y. Li, *Appl. Phys. Lett.* **95**, 131116 (2009).

[10] F. Qin, Y. Liu, and Z.-Y. Li, *J. Opt.* **12**, 035209 (2010).

[11] J. D. Cox and M. R. Singh, *J. Appl. Phys.* **108**, 083102 (2010).

[12] N. Tétreault, E. Arsenault, L.-P. Heiniger, N. Soheilnia, J. Brillet, T. Moehl, S. Zakeeruddin, G. A. Ozin, and M. Gratzel, *Nano Lett.* **11**, 4579 (2011).

[13] C. E. Talley, J. B. Jackson, C. Oubre, N. K. Grady, C. W. Hollars, S. M. Lane, T. R. Huser, P. Nordlander, and N. J. Halas, *Nano Lett.* **5**, 1569 (2005).

[14] I. N. Zheludev, *Opt. Photon. News* **22**, 30 (2011).

[15] H. A. Atwater and A. Polman, *Nat. Mater.* **9**, 205 (2010).

[16] L. Novotny and N. Van Hulst, *Nat. Photon.* **5**, 83 (2011).

[17] A. Gonzalez-Tudela, D. Martin-Cano, E. Moreno, L. Martin-Moreno, C. Tejedor, and F. J. Garcia-Vidal, *Phys. Rev. Lett.* **106**, 020501 (2011).

[18] P. R. West, S. Ishii, G. V. Naik, N. K. Emani, V. M. Shalaev, and A. Boltasseva, *Laser Photonics Rev.* **4**, 795 (2010).

[19] A. H. Castro Neto, F. Guinea, N. M. R. Peres, K. S. Novoselov, and A. K. Geim, *Rev. Mod. Phys.* **81**, 109 (2009).

[20] F. Bonaccorso, Z. Sun, T. Hasan, and A. C. Ferrari, *Nat. Photon.* **4**, 611 (2010).

[21] F. Schedin, E. Lidorikis, A. Lombardo, V. G. Kravets, A. K. Geim, A. N. Grigorenko, K. S. Novoselov, and A. C. Ferrari, *ACS Nano* **4**, 5617 (2010).

[22] F. H. L. Koppens, D. E. Chang, and F. J. G. Abajo, *Nano Lett.* **11**, 3370 (2011).

[23] K. P. Loh, Q. Bao, G. Eda, and M. Chhowalla, *Nat. Chem.* **2**, 1015 (2010).

[24] R. R. Nair, P. Blake, A. N. Grigorenko, K. S. Novoselov, T. J. Booth, T. Stauber, N. M. R. Peres, and A. K. Geim, *Science* **320**, 1308 (2008).

[25] T. Mueller, F. Xia, and P. Avouris, *Nat. Photon.* **4**, 297 (2010).

[26] M. Jablan, H. Buljan, and M. Soljacic, *Phys. Rev. B* **80**, 245435 (2009).

[27] Q. Bao, H. Zhang, B. Wang, Z. Ni, C. H. Y. X. Lim, Y. Wang, D. Y. Tang, and K. P. Loh, *Nat. Photon.* **5**, 411 (2011).

[28] C. Tegenkamp, H. Pfnur, T. Langer, J. Baringhaus, and H. W. Schumacher, *J. Phys.: Condens. Matter* **23**, 012001 (2011).

[29] A. Manjavacas, P. Nordlander, and F. J. G. Abajo, *ACS Nano* **6**, 1724 (2012).

[30] A. Cao, Z. Liu, S. Chu, M. Wu, Z. Ye, Z. Cai, Y. Chang, S. Wang, Q. Gong, and Y. Liu, *Adv. Mater.* **22**, 103 (2010).

[31] Z. Chen, S. Berciaud, C. Nuckolls, T. F. Heinz, and L. E. Brus, *ACS Nano* **4**, 2964 (2010).

[32] H. Dong, W. Gao, F. Yan, H. Ji, and H. Ju, *Anal. Chem.* (Washington, DC) **82**, 5511 (2010).

[33] P. Wang, T. Jiang, C. Zhu, Y. Zhai, D. Wang, and S. Dong, *Nano Res.* **3**, 794 (2010).

[34] E. Shafran, B. D. Mangum, and J. M. Gerton, *Nano Lett.* **10**, 4049 (2010).

[35] G. Goncalves, P. A. A. P. Marques, C. M. Granadeiro, H. I. S. Nogueira, M. K. Singh, and J. Gracio, *Chem. Mater.* **21**, 4796 (2009).

[36] C. Xu, X. Wang, and J. Zhu, *J. Phys. Chem. C* **112**, 19841 (2008).

[37] R. Patakfalvi, D. Diaz, P. Santiago-Jacinto, G. Rodriguez-Gattorno, and R. Sato-Berru, *J. Phys. Chem. C* **111**, 5331 (2007).

[38] S. Evangelou, V. Yannopapas, and E. Paspalakis, *Phys. Rev. A* **83**, 023819 (2011); *Phys. Rev. A* **83**, 055805 (2011); V. Yannopapas, E. Paspalakis, and N. V. Vitanov, *Phys. Rev. Lett.* **103**, 063602 (2009).

[39] M. O. Scully and M. S. Zubairy, *Quantum Optics* (Cambridge University Press, Cambridge, UK, 1997).

[40] M. Fleischhauer, A. Imamoglu, and J. P. Marangos, *Rev. Mod. Phys.* **77**, 633 (2005).

[41] M. V. Gurudev Dutt, J. Cheng, B. Li, X. Xu, X. Li, P. R. Berman, D. G. Steel, A. S. Bracker, D. Gammon, S. E. Economou, R.-B. Liu, and L. J. Sham, *Phys. Rev. Lett.* **94**, 227403 (2005).

[42] X. Xu, B. Sun, P. R. Berman, D. G. Steel, A. S. Bracker, D. Gammon, and L. J. Sham, *Nat. Phys.* **4**, 692 (2008).

[43] J. M. Elzerman, K. M. Weiss, J. Miguel-Sanchez, and A. Imamoglu, *Phys. Rev. Lett.* **107**, 017401 (2010).

[44] D. Sarid and W. A. Challener, *Modern Introduction to Surface Plasmons: Theory, Mathematica Modeling, and Applications* (Canbridge University Press, New York, 2010).

[45] P. Hanarp, M. Käll, and D. S. Sutherland, *J. Phys. Chem. B* **107**, 5768 (2003).

[46] C. Langhammer, M. Schwind, B. Kasemo, and I. Zorić, *Nano Lett.* **8**, 1461 (2008).

[47] C. F. Bohren and D. R. Huffman, *Absorption and Scattering of Light by Small Particles* (Wiley, New York, 1983), Chap. 5.

[48] E. C. Le Ru, *Principles of Surface-Enhanced Raman Spectroscopy and Related Plasmonic Effects* (Elsevier, Amsterdam, 2009), Appendix G.

[49] B. E. Kane, *Phys. Rev. B* **82**, 115441 (2010).

[50] S. John and J. Wang, *Phys. Rev. B* **43**, 12772 (1991).

[51] I. Haque and M. R. Singh, *J. Phys.: Condens. Matter* **19**, 156229 (2007).

[52] S. Thongrattanasiri, A. Manjavacas, and F. J. G. de Abajo, *ACS Nano* **6**, 1766 (2012).

Chapter 5

Nonlinear Two-Photon Absorption in Graphene Heterostructures

In the previous chapter, a graphene nanocomposite system was investigated in which linear-optical processes resulted in energy transfer between a quantum emitter and a graphene nanodisk. In this chapter, nonlinear optical processes are explored in a graphene nanocomposite (heterostructure) system.

5.1 Introduction

Recent advances in nanofabrication techniques have led to a rising interest in the optoelectronic properties of nanocomposite systems that combine quantum emitters (e.g., quantum dots or fluorescent molecules) with plasmonic (i.e., conducting) nanoparticles [1]. Typically, these types of nanocomposites employ the strong local electromagnetic field produced by localized surface plasmons in noble metal nanoparticles to enhance and/or control optical processes in nearby molecules or semiconductor nanoparticles. Strong local fields generated by localized surface plasmons are particularly attractive in the study of nonlinear optical processes [1-11], which scale with a high power of the electric field. A number of recent experimental and theoretical studies have demonstrated that nonlinear optical processes such as two-photon absorption/luminescence [2-5] and second- [6, 7] or third-harmonic generation [8] in semiconductor quantum dots (QDs) can be enhanced by surface plasmons in metal nanoparticles, indicating

that QD-metal nanoparticle hybrid systems can be used for nonlinear optical applications such as all-optical switching, biosensing, and other types of signal processing [2, 3]. Two-photon fluorescence from biological markers (dyes, aptamers, etc.) enhanced by noble metal nanoparticles has also been widely studied for applications in biological imaging [9-11]. Zhang et al. [10], for example, demonstrated that energy transfer between a commonly used molecular DNA label and gold nanoparticles under two-photon excitation using fluorescence lifetime imaging microscopy can be used to provide detailed information in biological studies.

Graphene has also attracted a great deal of attention in experimental and theoretical investigations on nanocomposite systems. In several studies, graphene-QD nanocomposites were fabricated and resonant energy transfer was observed through the photoluminescence of the QDs, which was strongly quenched in the presence of graphene [12-14]. Energy transfer in a QD-graphene nanocomposite system has been investigated theoretically [15]. Hybrid graphene-QD phototransistors have been fabricated and were found to exhibit ultrahigh photodetection gain with high quantum efficiency [16]. In the field of plasmonics, graphene has been recognized as a promising alternative to noble metals, as plasmons in chemically or electrostatically doped graphene have been shown to facilitate strong light-matter interactions and can be easily tuned electrostatically [17, 18]. Strong coupling between plasmons in nanostructured graphene with a quantum emitter has been predicted in theoretical studies, which could lead to the development of quantum plasmonic devices that operate at the single-photon/plasmon level [19-21].

In several experimental studies, interesting nonlinear optical effects in graphene-based nanocomposites have been observed. For instance, Feng et al. [22] synthesized graphene nanosheets decorated with tiny CdS QDs and observed nonlinear scattering and nonlinear absorption at two distinct excitation wavelengths. Lee et al. [23] deposited gold nanocrystals of various shapes on graphene oxide and examined the linear and nonlinear optical properties of the graphene oxide-gold nanocrystal composites. They observed a four-fold enhancement in the two-photon excitation emission intensity of the nanocomposite compared to that of pure gold nanocrystals.

In the present chapter, a theory has been developed for the enhancement and control of two-photon absorption in a nanocomposite made by combining an electrostatically doped graphene nanoflake with a QD. In this hybrid system, the electrostatically tunable localized surface plasmons in the graphene nanoflake generate a strong local electromagnetic field that enhances

the nonlinear optical response of the QD. It is shown that the two-photon absorption coefficient and power absorption in the QD can be controlled by changing the Fermi level in the graphene nanoflake via electrostatic gating. This effect can be used to manipulate two-photon absorption and/or fluorescence from the QD. The present findings are also directly applicable to graphene nanocomposites made with other types of quantum emitters such as molecules, dyes, etc. It is anticipated that the present hybrid system can be used to fabricate nonlinear optical devices such as switches, biological sensors and signal processors.

5.2 Theoretical Formalism

5.2.1 Local Field Enhancement

In the present model, a semiconductor QD is placed above a graphene nanoflake lying in the x-y plane, where the center-to-center distance between the nanoflake and the dot is denoted as R. A schematic diagram of the system is shown in Figure 5-1(a). Together the QD and graphene nanoflake form a nanocomposite or hybrid system. It is considered that the graphene nanoflake is deposited on a dielectric substrate with relative permittivity ϵ_s, while the QD is surrounded by a background dielectric material with relative permittivity ϵ_b. An external laser field $E_0 \cos(\omega t)$ is applied to the system, which interacts with both the QD and graphene nanoflake.

In the graphene nanoflake the optical excitations are localized surface plasmon polaritons, which have a resonance frequency ω_{sp}. When the frequency of the external field lies near the surface plasmon resonance frequency (i.e., $\omega \approx \omega_{sp}$), there is a strong excitation of surface plasmons in the graphene nanoflake. These plasmons create a dipole moment P_g in the nanoflake, which in turn produces an enhanced local field at the location of the QD given as

$$E_g = \frac{g_k P_g}{4\pi \epsilon_b \epsilon_0 R^3}.$$

(5.1)

Here g_k $(k = x, y, z)$ is called the polarization parameter, with $g_x = g_y = -1$ when the applied field is in the plane of the graphene nanoflake and $g_z = 2$ when the applied field is perpendicular to the nanoflake. To calculate the polarization of the graphene nanoflake P_g, the quasistatic
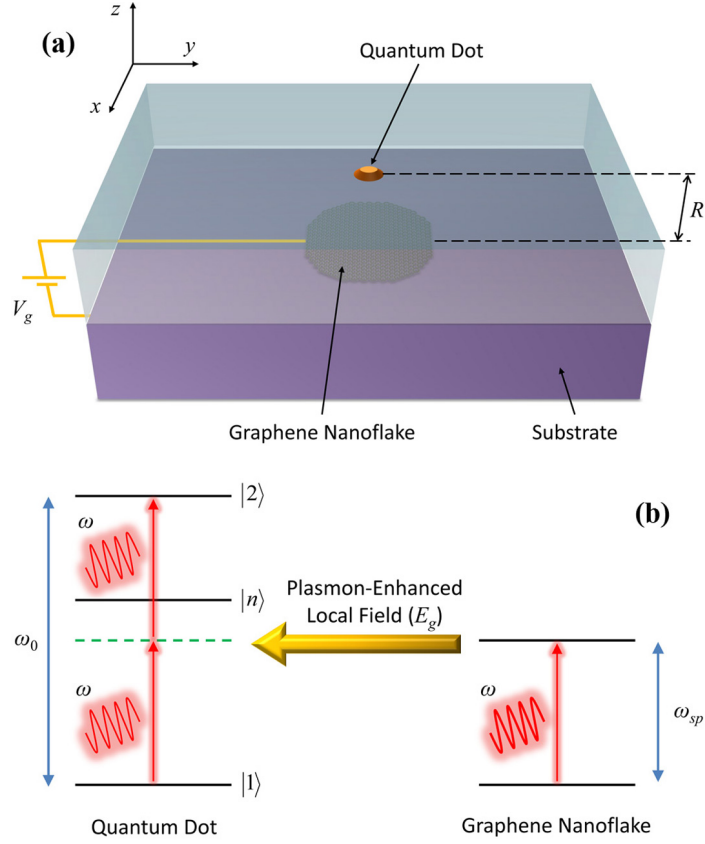
Figure 5-1: (a) Schematic diagram of the QD-graphene nanoflake hybrid system. The graphene nanoflake lies on a dielectric substrate and a QD is placed directly above at a distance R from the nanoflake. A gate voltage V_g is applied to the graphene nanoflake. (b) Energy level diagrams for the QD and graphene nanoflake. The external field excites surface plasmons in graphene and excitons in the QD via two-photon absorption.

approximation is used, in which a spatially uniform but time-varying electric field is assumed to interact with the nanoflake. Note that this approximation is only valid for nanoparticles with dimensions much less than the wavelength of the incident light [24]. An analytic expression for P_g is obtained by modelling the graphene nanoflake as a very flat and thin oblate spheroid with semimajor axes $d_x = d_y$ and semiminor axis d_z, where $d_x > d_z$. The in-plane polarization of the nanoflake for an electric field applied in the plane of the nanoflake (x-y plane) is then found as

$$P_g = \epsilon_{sb}\epsilon_0 \alpha_x\left(\omega\right) E_0, \tag{5.2}$$

91

where

$$\alpha_x\left(\omega\right) = \pi d_x^3 \frac{\left[\frac{\sigma_g(\omega)}{\epsilon_{sb}\epsilon_0\omega d_x}\right]i}{1 + \frac{3\pi}{16}\left[\frac{\sigma_g(\omega)}{\epsilon_{sb}\epsilon_0\omega d_x}\right]i}. \tag{5.3}$$

In the above expression, $\alpha_x\left(\omega\right)$ is the dipole polarizability in the two-dimensional limit $d_x \gg d_z$ [24], while the quantity $\epsilon_{sb} = \left(\epsilon_s + \epsilon_b\right)/2$ is the effective relative permittivity of the medium surrounding the graphene nanoflake, which accounts for the differing dielectric media on either side of the nanoflake [26]. In Eq. 5.3, $\sigma_g\left(\omega\right)$ is the in-plane conductivity of graphene and is obtained as [19]

$$\sigma_g\left(\omega\right) = \sigma_{intra}\left(\omega\right) + \sigma_{inter}\left(\omega\right), \tag{5.4}$$

where

$$\sigma_{intra}\left(\omega\right) = \frac{e^2 E_F}{\pi\hbar^2}\frac{i}{\omega + i\tau^{-1}} \tag{5.5}$$

is the Drude-like intraband conductivity and

$$\sigma_{inter}\left(\omega\right) = \frac{e^2}{4\hbar}\left[\theta\left(\hbar\omega - 2E_F\right) + \frac{i}{\pi}\log\left|\frac{\hbar\omega - 2E_F}{\hbar\omega + 2E_F}\right|\right] \tag{5.6}$$

is the interband conductivity. In the above expressions, the parameter E_F is the Fermi energy of the doped graphene nanoflake and $\tau = \mu E_F/ev_F^2$ is the intrinsic relaxation time, where v_F is the Fermi velocity and μ is the dc mobility. Here, incident photon frequencies such that $\hbar\omega < 2E_F$ are considered, and so only the intraband contribution to the total conductivity $\sigma_{intra}\left(\omega\right)$ plays a significant role in the generation of surface plasmons. At the surface plasmon resonance frequency ω_{sp}, the real part of the denominator in Eq. 5.3 becomes zero and α_x becomes large. This gives the following condition for the surface plasmon resonance frequency in the graphene nanoflake:

$$\omega_{sp} = \sqrt{\frac{3e^2 E_F}{16\hbar^2\epsilon_{sb}\epsilon_0 d_x} - \tau^{-2}} \tag{5.7}$$

Note that the local field from the graphene nanoflake (E_g) is strongest when $\omega = \omega_{sp}$.

In a number of experimental studies it has been shown that the Fermi energy in graphene can be controlled via electostatic gating, where the relationship between E_F and an external

gate voltage V_g can be described using a simple capacitor model as [27, 28]

$$|E_F| = \hbar v_F \sqrt{\pi C_g |V_g + V_0|}. \tag{5.8}$$

In the above expression, C_g is a constant which depends on the gate capacitance and V_0 is the offset voltage caused by natural doping. Hence, the polarizability $\alpha_x(\omega)$ and surface plasmon resonance frequency ω_{sp} of the graphene nanoflake, which depends on the Fermi energy, can be tuned by varying the gate voltage.

Since the QD is near the graphene nanoflake it interacts with both the external laser field and the local field produced by graphene, both of which oscillate at frequency ω. The total electric field experienced by the QD is then given by

$$E_{qd} = \frac{1}{2\epsilon_{eff}} (E_0 + E_g) e^{-i\omega t} + c.c., \tag{5.9}$$

where $\epsilon_{eff} = (2\epsilon_b + \epsilon_{qd})/3\epsilon_b$, ϵ_{qd} being the dielectric constant of the QD. The QD is treated as a two-level system, where $|1\rangle$ and $|2\rangle$ are the ground and excited states, respectively, and the resonant frequency for the transition $|1\rangle \leftrightarrow |2\rangle$ is denoted by ω_0. Here it is considered that the two-photon resonance frequency of the QD is twice the surface plasmon resonance frequency of the graphene nanoflake, i.e., $\omega_0 = 2\omega_{sp}$ (see Figure 5-1(b)). This resonance condition can be achieved for a specific QD simply by choosing an appropriate value for $V_g + V_0$. Due to the strong local field from the graphene nanoflake, nonlinear two-photon absorption occurs in the QD when $2\omega = \omega_0$. In the present model, the QD undergoes two-photon excitation from the ground state $|1\rangle$ to excited state $|2\rangle$ through virtual transitions involving one or more intermediate states $|n\rangle$ which are far from resonance with the external field. In this case the polarization of the QD P_{qd} can be expressed as [29]

$$P_{qd} = (k_{11}\rho_{11} + k_{22}\rho_{22}) \left(\frac{E_0}{\epsilon_{eff}} + \frac{E_g}{\epsilon_{eff}} \right) + 2k_{21} \left(\frac{E_0}{\epsilon_{eff}} + \frac{E_g}{\epsilon_{eff}} \right)^* \rho_{21}. \tag{5.10}$$

In the above expression, ρ_{ij} $(i, j = 1 \text{ or } 2)$ are the two-level density matrix elements which are obtained in the following section of this chapter, and k_{ij} are called the two-photon coefficients

93

and are given as

$$k_{21} = \frac{1}{\hbar} \sum_n \frac{\mu_{2n}\mu_{n1}}{\omega_{n1} - \omega} \tag{5.11}$$

$$k_{ii} = \frac{2}{\hbar} \sum_n \frac{|\mu_{ni}|^2 \omega_{ni}}{\omega_{ni}^2 - \omega^2}.$$

Here ω_{ni} and μ_{ni} and the transition frequencies and dipole matrix elements, respectively, between states $|n\rangle$ and $|i\rangle$. The first and second terms in Eq. 5.10 represent the contributions to the polarization of the QD from the off-resonant dipoles (which depends on the populations in states $|1\rangle$ and $|2\rangle$ given by ρ_{ii}) and the two-photon two-level coherence ρ_{21}, respectively [29, 30].

5.2.2   Density Matrix Formalism

The density matrix elements appearing in Eq. 5.10 are evaluated from their equations of motion obtained using the master equation method [29, 31]. Using Eq. 5.9, the two-level two-photon density matrix equations of motion are obtained as

$$\frac{d\rho_{22}}{dt} = -\Gamma\rho_{22} + i\Omega_0 \left(1 + \Pi_g\right)^2 \rho_{12} - i\Omega_0 \left(1 + \Pi_g^*\right)^2 \rho_{21} \tag{5.12}$$

$$\frac{d\rho_{12}}{dt} = -\left[\gamma - i\left(\Delta + \Delta_S\right)\right]\rho_{12} + i\Omega_0 \left(1 + \Pi_g^*\right)^2 \left(\rho_{22} - \rho_{11}\right), \tag{5.13}$$

where

$$\Delta_S = \beta_S \Omega_0 \left|1 + \Pi_g\right|^2, \tag{5.14}$$

$$\Omega_0 = \frac{k_{21} E_0^2}{2\hbar\epsilon_{eff}^2}, \tag{5.15}$$

and

$$\Pi_g = \frac{g_x \alpha_x(\omega)}{4\pi R^3}. \tag{5.16}$$

Here $\Delta = 2\omega - \omega_0$ is the two-photon detuning parameter, Γ and γ are the relaxation and dephasing rates, respectively, for the transition $|1\rangle \leftrightarrow |2\rangle$, and $\beta_S = (k_{11} - k_{22})/(2k_{21})$ [29]. The equations of motion for the remaining density matrix elements are easily obtained through the relations $\rho_{11} + \rho_{22} = 1$ and $\rho_{12} = \rho_{21}^*$. In the above expressions, the parameter Ω_0 denotes

the two-photon Rabi frequency due to direct two-photon absorption in the QD from the external field, while the term Π_g represents the local field enhancement factor due to the plasmons excited in the graphene nanoflake. Finally, the parameter Δ_S represents the dynamic Stark shift which appears due to frequency shifts in the levels $|1\rangle$ and $|2\rangle$ induced by virtual transitions to the intermediate level(s) $|n\rangle$ [29, 30]. The density matrix equations of motion are solved under steady-state conditions to obtain the elements ρ_{ij}, which are used to calculate P_{qd}.

5.2.3 Two-Photon Absorption

The QD absorbs energy from the external field and from the enhanced local field of the graphene nanoflake through a two-photon absorption process. The two-photon absorption coefficient of the QD can be obtained from P_{qd} as [29]

$$\alpha_{TPA} = \mathrm{Re}\left(-\frac{i\omega}{2\epsilon_b\epsilon_0 cV_{qd}}\frac{P_{qd}}{E_{qd}}\right) \tag{5.17}$$

where V_{qd} is the volume of the QD. Analytical expressions for the density matrix elements ρ_{ij} are obtained in the steady-state and used in Eq. 5.10 to obtain the two-photon absorption coefficient of the QD as

$$\alpha_{TPA} = \frac{\omega k_{21}}{\epsilon_b\epsilon_0 cV_{qd}}\frac{\gamma\Gamma\Omega_0\left|1+\Pi_g\right|^2}{\Gamma\left[\gamma^2+(\Delta+\Delta_S)^2\right]+4\gamma\Omega_0^2\left|1+\Pi_g\right|^4} \tag{5.18}$$

Notice that the above expression depends on both the external field (Ω_0) and the local field produced by the graphene nanoflake (Π_g). The second term in the denominator leads to a broadening of the absorption spectrum that depends on the intensity of the external field through Ω_0. This broadening is referred to as power broadening in the literature [32]. However, the second term in the denominator also depends on the local field from the graphene nanoflake through the term Π_g, which depends on the graphene polarizability $\alpha_x(\omega)$ and the center-to-center distance between the nanoflake and the QD R. This is an interesting effect which here will be referred to as local field broadening. Note also that the two-photon absorption coefficient is inversely related to Ω_0 and Π_g.

Following the method of Ref. [15], the power absorbed by the QD via the two-photon

absorption process is calculated as

$$W_{qd} = \hbar\omega_0 \Gamma \rho_{22} \qquad (5.19)$$

Using the steady-state solution for ρ_{22}, the expression for the QD power absorption is obtained as

$$W_{qd} = \frac{2\hbar\omega_0 \Gamma \gamma \Omega_0^2 |1 + \Pi_g|^4}{\Gamma \left[\gamma^2 + (\Delta + \Delta_S)^2\right] + 4\gamma \Omega_0^2 |1 + \Pi_g|^4} \qquad (5.20)$$

Note that the power absorbed by the QD depends on the population density ρ_{22} of the excited state $|2\rangle$, which in turn depends on the local field enhancement from the graphene nanoflake through Π_g. This shows that energy absorbed by the graphene nanoflake can be transferred to the QD. However, there is no energy transfer from the QD to the graphene nanoflake because conservation of energy would not be satisfied in this process (since $\omega_0 \neq \omega_{sp}$).

5.3   Results and Discussion

The graphene nanoflake has a radius $d_x = 17$ nm and is deposited on a silica substrate ($\epsilon_s = 1.96$). To calculate the optical response of the graphene nanoflake, parameters $C_g = 2 \times 10^{16}$ m^{-2}V^{-1} and $V_g + V_0 = 36.6$ V are used, while $v_F = c/300$ is the Fermi velocity and $\mu = 10000$ cm^{2}V^{-1}s^{-1} is the dc mobility [19]. For finite-sized graphene flakes, a small band gap appears in the electronic dispersion relation [33]. In the present investigation, it is considered that the Fermi level of the doped graphene nanoflake is well above any band gap arising due to size effects. Therefore, edge effects due to the finite size of the graphene nanoflake are neglected. It has been reported in the literature that edge effects play a significicat role in the optical response of graphene nanoflakes with sizes below 10 nm [34].

The background dielectric material for the hybrid system is taken as GaAs ($\epsilon_b = 10.95$). Using the parameters given above, the surface plasmon resonance frequency of the graphene nanoflake is calculated using Eq. 5.3 as $\omega_{sp} = 175$ meV. A p-type InAs/GaAs self-assembled QD ($\epsilon_{qd} = 11.84$) as described in Ref. [35] is chosen as a realistic example. For this QD the energy difference for the transition from the ground state $|1\rangle$ to the intermediate state $|n\rangle$ as $\hbar\omega_{n1} = 160$ meV, while the two-photon resonance frequency and relaxation rate are $\hbar\omega_0 = 350$ meV and $\hbar\Gamma = 200$ μeV, respectively [35]. Note that the p-type InAs/GaAs QD was

chosen so that the resonance frequencies of the graphene nanoflake and QD satisfy the condition $2\omega_{sp} = \omega_0$. The in-plane transition dipole moments are obtained in Ref. [35] as $\mu_{n1} = 0.11$ $e\cdot$ nm and $\mu_{2n} = 0.21$ $e\cdot$ nm. In the following simulations it is considered that the external driving field is polarized along the x-axis and has an intensity of 750 kW/cm^2.

5.3.1 Effect of Quantum Dot-Graphene Separation

Initially, the effect of the separation distance between the QD and graphene nanoflake on two-photon processes in the QD is studied. In Figure 5-2 the two-photon absorption coefficient (α_{TPA}) is plotted as a function of the two-photon detuning parameter Δ for various values of QD-graphene nanoflake separation R.

The results presented in Figure 5-2(a) show that when the graphene-QD separation is larger (i.e. $R = 40$ nm or higher) the absorption spectrum consists of a single, narrow peak located at $\Delta = 0$. As R is decreased to 35 and 30 nm (dashed and dash-dotted curves, respectively), the peak in the absorption spectrum broadens and its height decreases. The observed broadening is attributed to the local field broadening as discussed in Eq. 5.18, while the asymmetry in the two-photon absorption spectrum is a result of the dynamic two-photon Stark shift. The Stark shift parameter Δ_S also depends on the local field enhancement factor Π_g, and it increases as R decreases (see Figure 5-2(a) inset).

In Figure 5-2(b) the two-photon absorption spectrum of the QD is investigated when smaller values of the graphene-QD separation R are considered. In this case the absorption spectrum switches from a single narrow peak at $R = 30$ nm (solid curve) to two local field-broadened peaks near $\Delta = \pm 3$ meV and a minimum at $\Delta = 0$ when $R = 15$ nm (dash-dotted curve). The observed splitting in the absorption spectrum occurs due to the local field enhancement term Π_g in Eq. 5.18, which has frequency-dependence from the graphene polarizability $\alpha_x(\omega)$. The local field enhancement term has a maximum at $\Delta = 0$, where the frequency of the external field coincides with the plasmon resonance frequency in graphene (i.e. $\omega = \omega_{sp}$), and increases as R decreases (see Figure 5-2(b) inset). For sufficiently small values of R, the local field from the graphene nanoflake (E_g) is large enough to suppress two-photon absorption in the QD at frequencies near $\Delta = 0$. This phenomenon is also evident by inspection of Eq. 5.18, which shows that α_{TPA} approaches zero as $|\Pi_g|$ becomes very large.

97
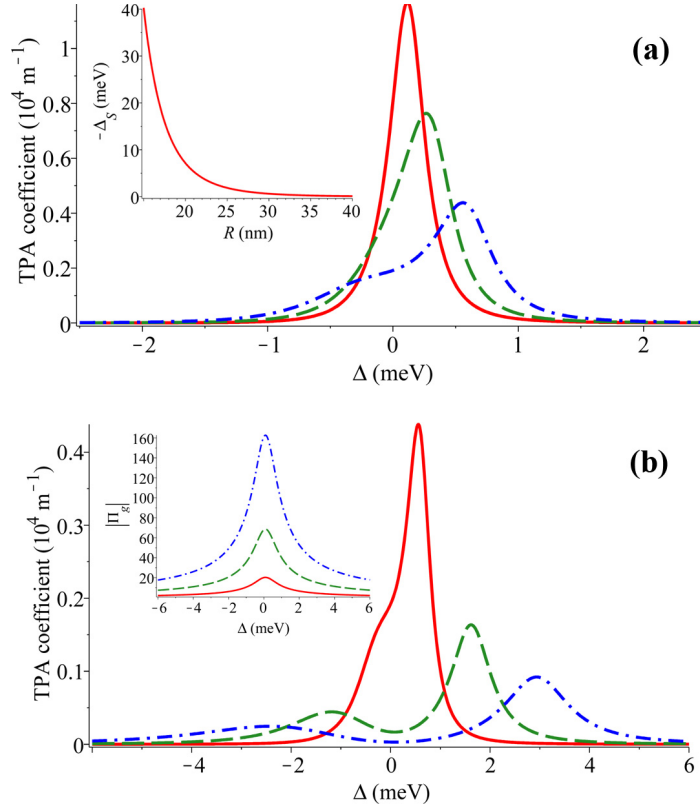
Figure 5-2: Two-photon absorption coefficient (α_{TPA}) vs. two-photon detuning (Δ) for different values of the graphene-QD separation R. Here the gate voltage in graphene is held fixed so that $V_0 + V_g = 36.6$ V. (a) $R = 40$ nm (solid curve), $R = 35$ nm (dashed curve), and $R = 30$ nm (dash-dotted curve). Inset: Stark shift parameter Δ_S as a function of R. (b) $R = 30$ nm (solid curves), $R = 20$ nm (dashed curves) and $R = 15$ nm (dash-dotted curves). Inset: Local field enhancement factor $|\Pi_g|$ as a function of Δ.

The QD power absorption spectrum given by Eq. 5.20 is plotted in Figure 5-3(a). It is found that for larger QD-graphene separation values (i.e. $R = 40$ nm, solid curve) the power absorption spectrum has a single, narrow peak. The width of the power absorption peak drastically increases as R is decreased to $R = 25$ nm (see dashed curve) due to local field broadening, as explained for the results shown in Figure 5-2(a), and the height of the peak also increases. A further decrease of the separation to $R = 15$ nm results in the emergence of a two-peaked, asymmetric structure in the power absorption spectrum, and two maxima (points A and C) and a local minimum (point B) are observed. This behavior arises from the competition between the local field enhancement of both the two-photon Rabi frequency and the Stark shift.

98
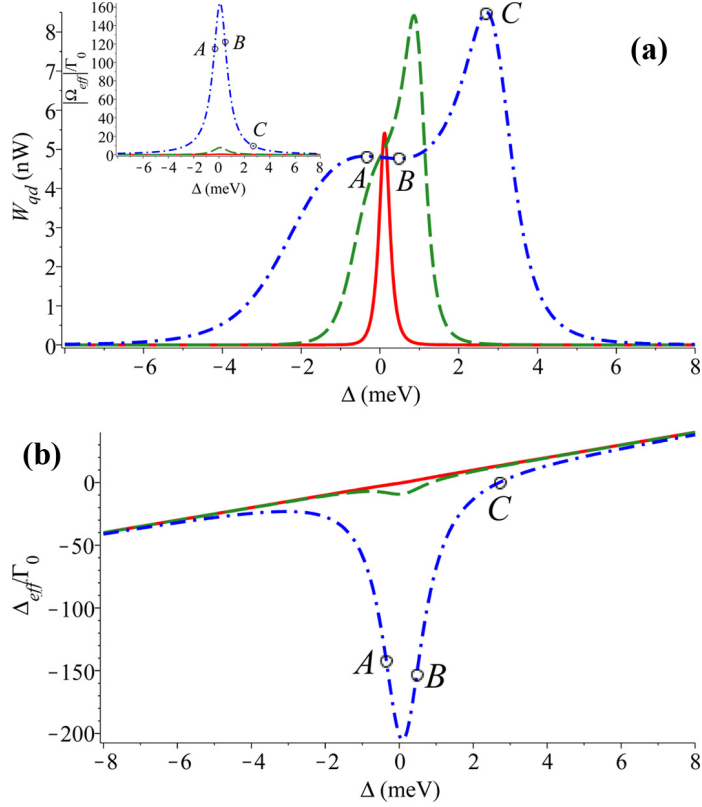
Figure 5-3: (a) Quantum dot power absorption (W_{qd}) vs. two-photon detuning (Δ) for cases where the graphene-quantum dot separation is $R = 40$ nm (solid curves), $R = 25$ nm (dashed curves), and $R = 15$ nm (dash-dotted curves). Here $V_0 + V_g = 36.6$ V. Inset: Effective two-photon Rabi frequency Ω_{eff} normalized to Γ_0 vs. two-photon detuning. (b) Effective detuning $\Delta_{eff} = \Delta + \Delta_S$ normalized to Γ_0 vs. two-photon detuning, where same labels are used as those for the distances considered in (a).

To illustrate this point, consider the equations of motion for the density matrix elements, Eq. (5.13): The effective Rabi frequency which drives the QD is given by $\Omega_{eff} \equiv \Omega_0 \left(1 + \Pi_g^*\right)^2$, while the effective detuning is given by $\Delta_{eff} \equiv (\Delta + \Delta_S)$. Note that Δ_S takes negative values since $\Omega_0 < 0$; hence the system will be close to resonance in the situation that minimizes Δ_{eff} while keeping a value of Ω_{eff} high enough to efficiently drive the QD from the ground level to the upper level through the two-photon step. These two competing effects produced by the plasmon interaction balance each other to produce the two maxima at points A and C, while at point B the effect of the Stark shift Δ_S dominates, resulting in a reduced value of the power transfer to the QD. This can be inferred by considering the Δ-dependence of both magnitudes

(Ω_{eff} and Δ_{eff}) presented in the inset of Figure 5-3(a) and in Figure 5-3(b). The global maximum at point C is obtained when magnitude of Δ_{eff} is small (see Figure 5-3(b)) while the effective Rabi frequency remains appreciable (Figure 5-3(a) inset). The amount of power absorbed at point A is obtained for a point where the effective detuning reaches a large value: In a conventional two-level system this situation would result in a negligible population of the upper-level. However, in the current system the effective Rabi frequency is also Δ-dependent and exhibits a large enhancement, which allows for a large population of the upper level even in the presence of such a large value of Δ_{eff} at point A.

To summarize, it has been demonstrated that two-photon processes in the QD can be enhanced by the local field created by plasmons in the graphene nanoflake. For the present hybrid system, the value of the graphene-QD separation R can be controlled by changing the thickness of GaAs between the graphene nanoflake and the QD during fabrication. Once the system has been fabricated, the separation can be changed by applying stress and strain fields (i.e., the hybrid system can act as a pressure sensor). The results presented here are also valid if the QD is replaced by a chemical or biological molecule for which two-photon absorption occurs. In this case the hybrid system can be used as a biological sensor, where different molecules attached to the graphene nanoflake will have different effective separations R. Another potential application for the present system lies in thermal sensing, where a thermally-sensitive spacing material between the quantum emitter and graphene is used. As the temperature increases the thermal spacer will expand, thereby changing R.

5.3.2 Effect of Gate Voltage

The effect of the gate voltage applied to graphene on the two-photon processes in the QD is now investigated. Recent studies have shown that plasmons in graphene can be conveniently controlled using electrostatic gating [16-21]. By changing the gate voltage V_g applied to the graphene nanoflake, one can change the concentration of conducting electrons in the nanoflake. This changes the Fermi energy in graphene through Eq. 5.8, which in turn changes the plasmon resonance frequency of the nanoflake through Eqs. 5.4 and 5.3. To consider the effect of the gate voltage in these calculations, V_g in Eq. 5.8 is replaced by $V_g + \Delta V_g$ and ΔV_g is varied. Note that in the present investigation the applied gate voltage does not alter the energy levels
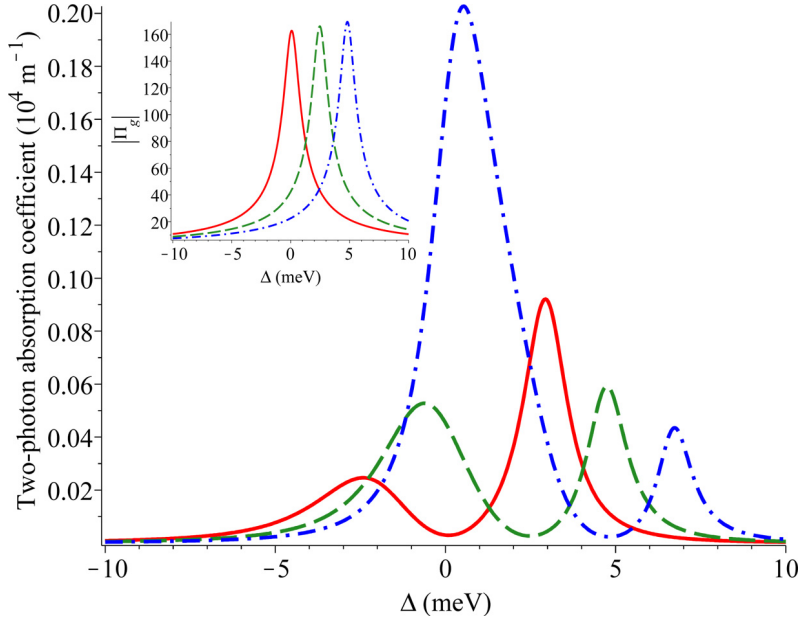
Figure 5-4: Two-photon absorption coefficient (α_{TPA}) vs. two-photon detuning (Δ) for cases where $\Delta V_g = 0$ (solid curve), $\Delta V_g = 1.0$ V (dashed curve), and $\Delta V_g = 2.0$ V (dash-dotted curve). Here $V_g + V_0 = 36.6$ V and $R = 15$ nm. Inset: Magnitude of the local field enhancement factor (Π_g) as a function of the two-photon detuning when $\Delta V_g = 0$ (solid curve), $\Delta V_g = 1.0$ V (dashed curve), and $\Delta V_g = 2.0$ V (dash-dotted curve).

of the QD, but merely modifies the properties of the graphene nanoflake.

The two-photon absorption coefficient of the QD is plotted in Figure 5-4 as a function of the two-photon detuning parameter for various values of ΔV_g. Here the graphene-QD separation is fixed at $R = 15$ nm. Note that the solid curve in Figure 5-4 corresponds to the dash-dotted curve in Figure 5-2(b), where $\Delta V_g = 0$ and a minimum appears at $\Delta = 0$. By increasing the gate voltage such that $\Delta V_g = 1.0$ and 2.0 V (see dashed and dash-dotted curves, respectively, in Figure 5-4), it is found that the minimum in the absorption spectrum shifts towards positive detunings. This phenomenon occurs due to the shift in the plasmon resonance frequency of the graphene nanoflake, which changes from its original value $\omega_{sp} = 175$ meV to $\omega_{sp}^g = \omega_{sp} + 1.24$ meV and $\omega_{sp}^g = \omega_{sp} + 2.41$ meV when $\Delta V_g = 1.0$ and 2.0 V, respectively. The shift in the plasmon frequency changes the frequency at which Π_g reaches its maximum value (see Figure 5-4 inset). It is also worth pointing out that the local field enhancement factor decreases significantly at $\Delta = 0$ as the gate voltage changes from $\Delta V_g = 0$ to $\Delta V_g = 2.0$ V (i.e., the
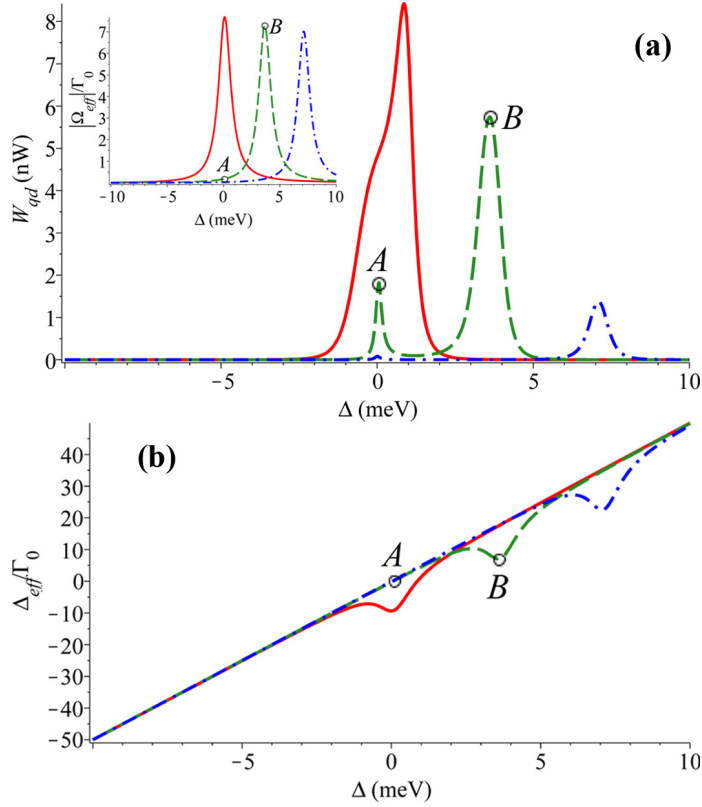
Figure 5-5: (a) QD power absorption (W_{qd}) vs. two-photon detuning (Δ) when the gate voltage in graphene is changed so that $\Delta V_g = 0$ (solid curve), $\Delta V_g = 1.5$ V (dashed curve), and $\Delta V_g = 3.0$ V (dash-dotted curve). Here $V_0 + V_g = 36.6$ V and $R = 25$ nm. Inset: Effective two-photon Rabi frequency Ω_{eff} normalized to Γ_0 vs. two-photon detuning. (b) Effective detuning $\Delta_{eff} = \Delta + \Delta_S$ normalized to Γ_0 vs. two-photon detuning, where the same labels for the gate voltages considered in (a) are used.

peak in $|\Pi_g|$ is shifted away from $\Delta = 0$). When the gate voltage is increased the enhancement factor has a very small value at $\Delta = 0$ and the two-photon absorption coefficient switches from a minimum to a maximum value.

The above discussion indicates that the minimum in the two-photon absorption spectrum can be shifted by changing the applied gate voltage. The secondary peaks in the absorption spectrum at higher detunings (i.e., at $\Delta \approx 5$ meV when $\Delta V_g = 1.0$ V or at $\Delta \approx 7$ meV when $\Delta V_g = 2.0$ V) are smaller because the external field is detuned from the two-photon resonance of the QD. By varying the external gate voltage, these secondary absorption peaks can also be switched from high to low values.

102

In Figure 5-5(a) the two-photon power absorption spectrum when $R = 25$ nm has been plotted for cases where $\Delta V_g = 0$, 1.5 and 3.0 V (see solid, dashed and dash-dotted curves, respectively). Note that the peak in the power absorption spectrum shifts away from $\Delta = 0$ towards positive detuning as the gate voltage is increased. This result demonstrates that the power absorption at $\Delta = 0$ can also be switched from high to very low values as ΔV_g is increased only slightly. As the plasmon resonance is shifted to new frequencies by the change in gate voltage, the effective Rabi frequency also moves to higher detunings. The primary peaks in the power absorption spectra then indicate the location of the maxima in Ω_{eff} (see Figure 5-5(a) inset). In Figure 5-5(b) the effective detuning Δ_{eff} is shown for the same values of ΔV_g used in Figure 5-5(a). At point A, the effective detuning is close to resonance, whereas it is slightly further from resonance at point B. Thus, the enhancement of the pumping by Ω_{eff} is less effective, which would account for the fact that in Figure 5-5(a) the peak value of the dashed curve is less than that for the solid curve.

5.3.3   Effect of Graphene Size

Here, the influence of the graphene nanoflake's size on the power transfer to the QD is investigated. This question is pertinent in view of the fact that the plasmon resonance frequency can be roughly estimated to be given by $\omega_{sp} = \sqrt{3e^2 E_F/16\hbar^2 \epsilon_{sb}\epsilon_0 d_x}$, which explicitly depends on d_x. In order to analyze the effect of the graphene flake's size on W_{qd}, numerical simulations in which the value of d_x is slightly changed around the original value of 17 nm are performed, while keeping fixed the intensity of the driving field (750 kW/cm^2) and the value of $R = 15$ nm. The results are depicted in Figure 5-6(a) for cases where $d_x = 16$ nm and $d_x = 18$ nm.

In the case of the largest value ($d_x = 18$ nm, dashed curve) the power transferred to the QD exhibits a two-peaked structure: One peak is located close to $\Delta = 0$ whereas the other shifts to the negative detuning region. For a nanodisk of this size, the new plasmon resonance ω_{sp} falls downward to 170.8 meV, which in turn leads to a shift of the resonance for the local field enhancement factor Π_g to the negative detuning region. In the case of the smallest value considered in Figure 5-6(a) ($d_x = 16$ nm, solid curve), the power transferred to the QD exhibits a three-peaked structure: A peak (point A) is recovered close to $\Delta = 0$, two outer maxima (points B and D) with similar heights are obtained, and a local minimum (point C) is found
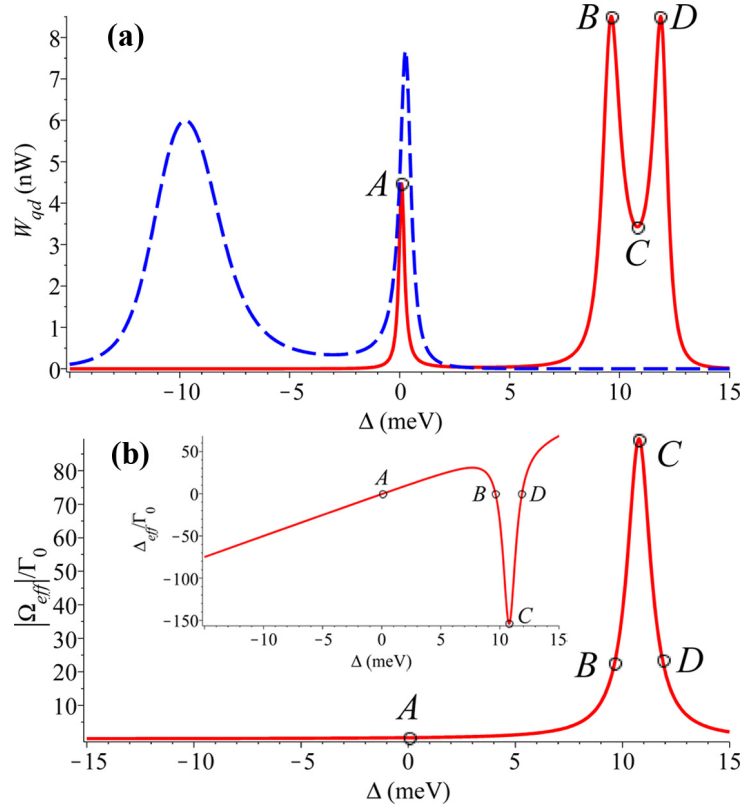
Figure 5-6: (a) QD power absorption (W_{qd}) vs. two-photon detuning (Δ) for cases where the size of the graphene nanodisk is $d_x = 16$ nm (solid curve) and $d_x = 18$ nm (dashed curve). (b) Effective Rabi frequency Ω_{eff} normalized to Γ_0 vs. two-photon detuning for the case where $d_x = 16$ nm. Inset: Effective detuning $\Delta_{eff} = \Delta + \Delta_S$ normalized to Γ_0 vs. Δ. Here $R = 15$ nm and the rest of the parameters are the same as those used in Figure 5-3.

between these two maxima. For this particular size of graphene nanodisk, the new plasmon resonance ω_{sp} rises upward to 181.1 meV, which in turn results in a shift of the resonance for the local field enhancement factor Π_g to the positive detuning region. The split of the expected maximum into two maxima (points B and D in Figure 5-6(a)) arises again from the competition between the dynamical Stark shift and the local field enhancement of the Rabi frequency, in a similar way to the results obtained for the dash-dotted curve in Figure 5-3(a). This can be further confirmed by inspecting Figure 5-6(b), which depicts the effective two-photon Rabi frequency and the effective detuning: The Stark shift at point C is at its maximum (see Figure 5-6(b) inset), and simultaneously, the enhancement of the Rabi frequency reaches its maximum

value. Thus, at point C the Stark shift dominates over the enhancement of the Rabi frequency, whereas at points B and D the latter dominates and produces the maxima.

5.4 Conclusions

In this chapter, two-photon absorption in a QD-graphene nanoflake nanocomposite system is investigated theoretically. It is found that when the frequency of an applied external laser field coincides with the plasmon resonance of the graphene nanoflake, a strong local field is generated by the plasmons in the nanoflake. When the QD is near the nanoflake, the local field from graphene causes a broadening of the two-photon absorption spectrum. If the QD is brought even closer to the nanoflake, the spectrum of two-photon absorption splits from a single peak to two peaks. It is also found that power absorption in the QD is enhanced by the local field from the graphene nanoflake. It is also shown that for this nanocomposite system the two-photon absorption process in the QD can be further manipulated by changing the Fermi energy in the graphene nanoflake via electrostatic gating. The present findings indicate that two-photon absorption and power absorption in the QD can be switched on or off by changing the gate voltage across the graphene nanoflake. These results suggest that the QD-graphene nanoflake hybrid system can be used for nonlinear optical applications such as all-optical switching, biosensing and signal processing.

Bibliography

[1] M. Achermann, *J. Phys. Chem. Lett.* **1**, 2837 (2010).

[2] M. Fu, K. Wang, H. Long, G. Yang, P. Lu, F. Hetsch, A. S. Susha, and A. L. Rogach, *Appl. Phys. Lett.* **100**, 063117 (2012).

[3] B. P. Khanal, A. Pandey, L. Li, Q. Lin, W. K. Bae, H. Luo, V. I. Klimov, and J. M. Pietryga, *ACS Nano* **6**, 3832 (2012).

[4] S. Xiao, H. Gong, X. Su, J. Han, Y. Han, M. Chen, and Q. Wang, *J. Phys. Chem. C* **111**, 10185 (2007).

[5] X. Li, F. -J. Kao, C. -C. Chuang, and S. He, *Opt. Express* **18**, 11335 (2010).

[6] E. Shaviv and U. Banin, *ACS Nano* **4**, 1529 (2010).

[7] P. M. Jais, C. von Bilderling, and A. V. Bragas, *Papers in Physics* **3**, 030002 (2011).

[8] X. Feng, Y. Chen, and D. Hou, *Physica B* **406**, 1702 (2011).

[9] N. J. Durr, T. Larson, D. K. Smith, B. A. Korgel, K. Sokolov, and A. Ben-Yakar, *Nano Lett.* **7** 941 (2007).

[10] Y. Zhang, D. J. S. Birch, and Y. Chen, *Appl. Phys. Lett.* **99** 103701 (2011).

[11] A. Ray, Y.-E. K. Lee, G. Kim, and R. Kopelman, *Small* **8**, 2213 (2012).

[12] Z. Chen, S. Berciaud, C. Nuckolls, T. F. Heinz, and L. E. Brus, *ACS Nano* **4**, 2964 (2010).

[13] H. Dong, W. Gao, F. Yan, H. Ji, and H. Ju, *Anal. Chem.* **82**, 5511 (2010).

[14] P. Wang, T. Jiang, C. Zhu, Y. Zhai, D. Wang, and S. Dong, *Nano Res.* **3**, 794 (2010).

[15] J. D. Cox, M. R. Singh, G. Gumbs, M. A. Antón, and F. Carreño, *Phys. Rev. B* **86**, 125452 (2012).

[16] G. Konstantatos, M. Badioli, L. Gaudreau, J. Osmond, M. Bernechea, F. P. Garcia de Arquer, F. Gatti, and F. H. L. Koppens, *Nat. Nanotech.* **7**, 363 (2012).

[17] Q. Bao and K. P. Loh, *ACS Nano* **6**, 3677 (2012).

[18] A. N. Grigorenko, M. Polini, and K. S. Novoselov, *Nat. Photon.* **6**, 749 (2012).

[19] F. H. L. Koppens, D. E. Chang, and F. J. Garcia de Abajo, *Nano Lett.* **11**, 3370 (2011).

[20] A. Manjavacas, P. Nordlander, and F. J. Garcia de Abajo, *ACS Nano* **6**, 1724 (2012).

[21] A. Manjavacas, S. Thongrattanasiri, D. E. Chang, and F. J. Garcia de Abajo, *New. J. of Phys.* **14**, 123020 (2012).

[22] M. Feng, R. Sun, H. Zhan, and Y. Chen, *Nanotechnology* **21**, 075601 (2010).

[23] Y. H. Lee, L. Polavarapu, N. Gao, P. Yuan, and Q.-H. Xu, *Langmuir* **28**, 321 (2012).

[24] D. Sarid and W. A. Challener, *Modern Introduction to Surface Plasmons: Theory, Mathematica Modeling, and Applications* (Canbridge University Press, New York, 2010).

[25] B. E. Kane, *Phys. Rev. B* **82**, 115441 (2010).

[26] P. Hanarp, M. Käll, and D. S. Sutherland, *J. Phys. Chem. B* **107**, 5768 (2003).

[27] F. Wang, Y. Zhang, C. Tian, C. Girit, A. Zettl, M. Crommie, and Y. R. Shen, *Science* **320**, 206 (2008).

[28] Z. Q. Li, E. A. Henriksen, Z. Jiang, Z. Hao, M. C. Martin, P. Kim, H. L. Stormer, and D. N. Basov, *Nat. Phys.* **4**, 532 (2008).

[29] P. Meystre and M. Sargent III, *Elements of Quantum Optics*, 4th ed. (Springer-Verlag, Berlin, 2007).

[30] D. A. Holm and M. Sargent III, *Opt. Lett.* **10**, 405 (1985).

[31] M. O. Scully and M. S. Zubairy, *Quantum Optics* (Cambridge University Press, Cambridge, UK, 1997).

[32] R. W. Boyd, *Nonlinear Optics*, 3rd ed. (Academic, New York, 2008).

[33] J. Robertson, *Adv. Phys.* **35**, 317 (1986).

[34] S. Thongrattanasiri, A. Manjavacas, and F. J. Garcia de Abajo, *ACS Nano* **6**, 1766 (2012).

[35] T. Brunhes, P. Boucaud, S. Sauvage, F. Glotin, R. Prazeres, J.-M. Ortega, A. Lemaître, and J.-M. Gérard, *Appl. Phys. Lett.* **75**, 835 (1999).

Chapter 6

Nonlinear Switching Mechanism in Metallic Heterostructures

In the previous chapter, nonlinear two-photon absorption was investigated in a graphene-quantum dot (QD) nanocomposite system. There the local field produced by plasmons in graphene was used to control two-photon absorption in the QD. In this chapter, nonlinear second harmonic generation and two-photon photoluminescence are studied in a QD-metal nanoparticle (MNP) nanocomposite system[1]. Here, the nonlinear optical processes in the QD are mediated by the plasmons in MNPs through the dipole-dipole interaction. In this chapter, theoretical results are used to explain experimental observations for several QD-MNP hybrid systems.

6.1 Introduction

In the field of nano-optics there has been considerable interest in studying the strong light-matter interactions that occur due to the enhanced local electromagnetic fields produced by metallic nanoparticles (MNPs) [1-3]. Strong local fields are particularly important for nonlinear optical processes, such as surface-enhanced Raman scattering and SH (second harmonic) generation [4, 5], which scale with a high power of the applied field(s). The symmetry of a

---

[1]The material presented in this chapter has been published in: J. D. Cox, M. R. Singh, C. von Bilderling, and A. V. Bragas, *Adv. Opt. Mater.* **1**, 460 (2013).

MNP and the polarization of the applied field have also been shown to play very important roles in local field enhancement [6]. SH generation has been investigated in metallic tips [7], T-shaped gold nano-dimers [8], bowtie-shaped nano-antennas [9], and metallic nanowires [10]. Controllable local field enhancement would also benefit other photonics applications such as nanoscale antennas [11], nanoscale lenses [12], and two-photon microscopy [13].

In a number of studies, semiconductor quantum dots (QDs) have been combined with MNPs to investigate the strong light-matter interactions that occur due to the enhanced local field of the MNP plasmons [1-3]. QDs are ideal for this purpose because of their size-tunable optical properties. They can also be used for optoelectronic applications such as low-threshold lasers, light-emitting diodes, solar cells, and nonlinear photonic devices. A variety of optical processes in QD-MNP hybrid systems are enhanced by the interaction of excitons in the QD with localized surface plasmons in the MNP. The optical processes that have been studied in these systems include enhanced photo-catalysis, light-harvesting and photovoltaics [14], SP-enhanced fluorescence [15], and Förster resonance energy transfer [16].

It has also been shown that the nonlinear optical response of semiconductor QDs can be enhanced by surface plasmons in metallic nanostructures. For example, MNPs on the surface of semiconductor QDs can greatly enhance the optical nonlinearity of the QDs [17]. Furthermore, the enhancement of SH generation in non-centrosymmetric semiconductor QDs was observed when the QDs were placed in close proximity to silver nanoparticles [18].

In this chapter, SH generation and two-photon photoluminescence (TPPL) in QD-MNP hybrid systems is investigated. In the present theoretical model, these nonlinear optical processes occur in a QD which is also interacting with a proximal MNP. A probe laser field is applied to the hybrid system, which drives SH generation and TPPL in the QD. A secondary control laser field is also applied to the system, which can couple with surface plasmons in the MNP. The MNP is strongly polarized when the frequency of the control field matches the MNP surface plasmon resonance frequency, leading to a dipole-dipole interaction between the QD and MNP. It is shown that when the control laser field is resonant with the plasmons in the MNP, the intensity of the SH signal from the QD can be increased by increasing the intensity of the control laser field. Conversely, the control field has little effect on the SH signal from the QD when it is not resonant with the plasmons in the MNP. These results indicate that the

SH signal enhancement can be switched on or off by changing the intensity or frequency of the control laser field.

The theoretical model presented here is used to explain an experimental study in which SH generation and TPPL are observed in QD-MNP hybrid systems consisting of CdS QDs in the presence of either Au or Ag MNPs. In the experiment, a pulsed laser field (probe field) was used to generate the SH signal from the hybrid system in the presence of a continuous-wave laser field (control field). SH generation and TPPL was measured in samples of CdS QDs alone, Au MNPs alone, CdS QDs with Au MNPs, and CdS QDs with Ag MNPs. In the CdS QD-Au MNP hybrid system, an increase in the SH signal intensity was observed as the power of the control laser field was increased. Here the control laser field was resonant with the localized surface plasmons in the Au MNPs. Conversely in the CdS QD-Ag MNP hybrid sample, the control field intensity was observed to have a negligible effect on the SH signal intensity. In this case, the control field was not resonant with the surface plasmons in the Ag MNP. The results of the theoretical simulations are compared with the experimentally-obtained data, and good qualitative agreement is found. It is anticipated that the results described here can be used to develop nonlinear all-optical nano-switching devices using hybrid systems.

6.2 Experimental Methods

Figure 6-1 shows schematically the experimental setup used to measure SH generation and TPPL from CdS QDs in the presence of MNPs. The experiment was performed in transmission with spectrally-resolved photon counting detection (1P28 Hamamatsu photomultiplier and Stanford Research SR400 Gated Photon Counter). The pulsed laser (probe field) used to generate the SH signal was a tunable modelocked Ti:Sapphire (KMLabs) set at a wavelength of $\lambda_p = 790$ nm, with 50 fs pulse width and 80 MHz repetition rate. A residual continuous-wave (CW) laser field (control field) originating from the $\lambda_c = 532$ nm doubled Ng:YAG pumping laser also reaches the sample.

For preparation of the hybrid Au MNP-QD sample, a drop (3 μl, 10^{10} NP/ml) of the MNP colloidal solution was dried onto a clean coverslip. Here commercial gold nanoparticles (Ted Pella) with an average radius of 40 nm were used. The colloids are surrounded by citrate
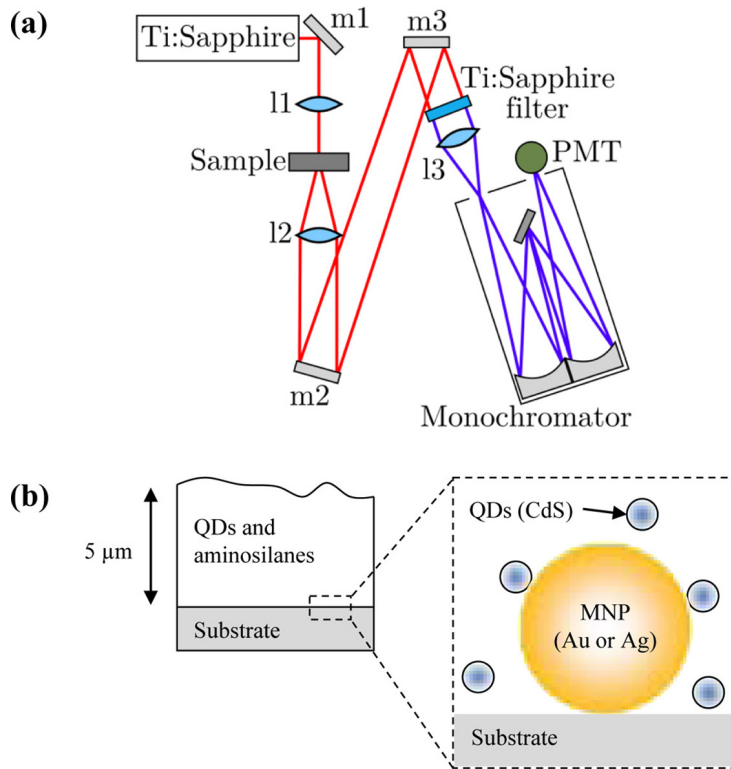
Figure 6-1: (a) Schematic diagram for the experimental setup. The pulsed Ti:Sa laser was tightly focused through l1 onto the coverslip containing the hybrid QD-MNP sample. A second lens, l2, collects the signal, which is sent to the monochromator by two mirrors (m2 and m3). A filter is interposed at its entrance in order to reduce the strong laser signal. Photon counting detection is performed with the photomultiplier (PMT). (b) Schematic diagram for the QD-MNP hybrid sample.

molecules, which provides them with a negative charge that electrostatically attaches them to the glass surface. The final surface concentration of the Au MNPs, measured from SEM images, is about 20 NPs per μm^2 (see Figure 6-2(a)). Finally, a drop of a 1 μM CdS QD colloidal solution is deposited on top of the sample until the solvent is evaporated. The QD solution has a high concentration of aminosilanes that forms a layer about 5 μm in height, so that the QDs are immersed in an aminosilane matrix (see Figure 6-2(b)). From AFM and SEM images it is concluded that there are 200 QDs per Au MNP on average, and that the average radius of the QDs is 1.5 nm. Silver MNPs of average radius 10 nm were synthesized as indicated in Ref. [18]. A similar protocol described above for the Au MNP-QD samples has been followed
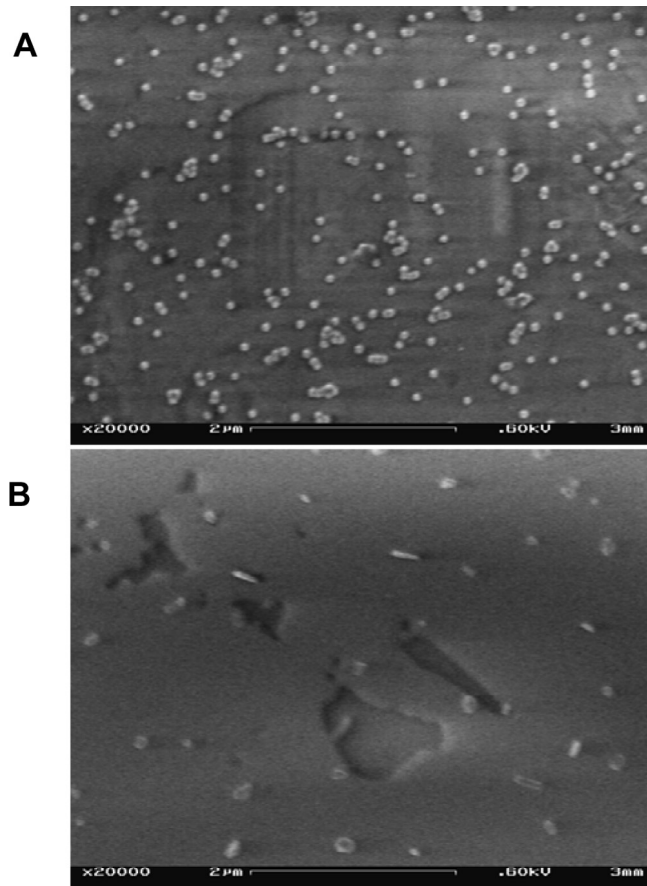
Figure 6-2: (a) SEM image of the Au MNPs, 40 nm in radius (about 20 MNPs per μm^2). (b) SEM image of the Au MNP-QD hybrid sample. It is no longer possible to view the nanoparticles since the QDs at high concentration form a thick layer (~5 μm) when dried.

to prepare the hybrid Ag MNP-QD sample, resulting in about 10 QDs per Ag MNP.

Spectrally-resolved photon counting experiments were performed on the QD-MNP hybrid samples as a function of the wavelength, keeping the incoming Ti:Sapphire laser wavelength fixed. A typical signal is shown by the square points in Figure 6-4 for the Au MNP-QD hybrid sample. The SH signal was highly visible, while a reduced signal of the two photon photoluminescence coming from the QDs was also detected around 490 nm (see Figure 6-7). At the maximum of the SH signal, the intensity is measured as a function of the green ($\lambda_c = 532$ nm) CW laser power at a fixed Ti:Sapphire power (see Figures 6-6(a) and 6-6(b)). To do this experiment, low-pass filters were interposed, taking special care not to affect the Ti:Sapphire

113

power. In Figure 6-6(a) the peak SH signal is collected for the Au MNP-QD hybrid system and in Figure 6-6(b) the peak SH signal is presented for the Ag MNP-QD system. In Figures 6-6(a) and 6-6(b) the horizontal axis gives the power of the $\lambda_c = 532$ nm CW laser field. Note that the Au nanoparticles have a plasmon resonance at about $\lambda_{Au}^{sp} = 532$ nm, whereas the plasmon resonance for the Ag nanoparticles is at about $\lambda_{Ag}^{sp} = 400$ nm. In Figure 6-6(a), an increase in the SH signal intensity is observed as the CW laser field power is increased for the Au-MNP-QD system, whereas in Figure 6-6(b) the Ag-MNP system does not show a significant increase.

6.3   Theoretical Formalism

The present system of interest consists of a QD and a MNP embedded in a background dielectric material with dielectric constant ϵ_b. The QD is modelled as a two-level system, where $|1\rangle$ and $|2\rangle$ denote the ground and excited states, respectively, and the resonant frequency for the transition $|1\rangle \leftrightarrow |2\rangle$ is denoted as ω_0. It is considered that the MNP has a surface plasmon resonance frequency ω_{sp}, which is taken to lie near the excitation frequency of the QD such that $\omega_{sp} \approx \omega_0$. The energy level diagram for the QD-MNP hybrid system is illustrated in Figure 6-3.

A probe laser field with amplitude E_p and frequency $\omega_p = \omega_0/2 + \Delta/2$ is applied to the hybrid system, where Δ is called the two-photon detuning parameter and is a small quantity compared to ω_0. Similarly, an applied control field with amplitude E_c and frequency ω_c are applied to the hybrid system. The interaction of the probe field with the QD leads to nonlinear two-photon excitation and SH generation due to the transitions $|1\rangle \rightarrow |n\rangle \rightarrow |2\rangle$, where $|n\rangle$ are intermediate (virtual) states of the QD. The nonlinear polarization of the QD can be obtained in terms of the two-level density matrix elements ρ_{ij} as [19]

$$P_{qd} = (k_{11}\rho_{11} + k_{22}\rho_{22} + 2k_{21}\rho_{21}) E_p, \tag{6.1}$$

where k_{ij} are the two-photon coefficients and are given explicitly in Ref. [19].

In the presence of the probe and control fields, dipole moments P_{qd} and P_{mnp} are induced in the QD and the MNP, respectively. These dipole moments each generate dipole electric fields (also called near or local fields) around the nanoparticle from which they originate. The electric
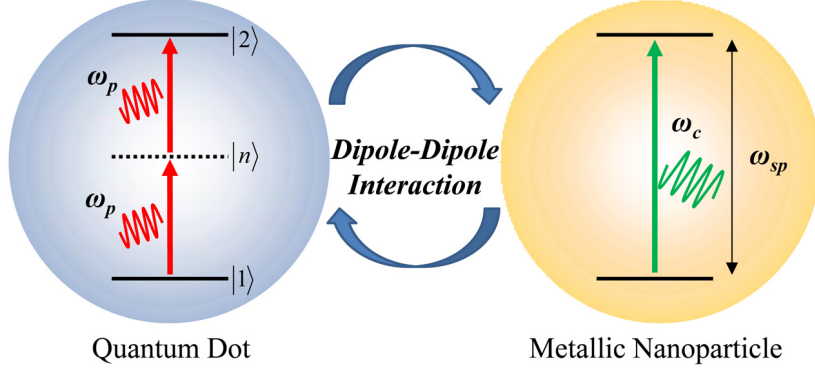
Figure 6-3: Energy level diagram of the QD-MNP hybrid system. A dipole-dipole interaction occurs between the QD and MNP.

field created by the MNP at the location of the QD is denoted as E_{ddi}^{mnp}, and is given as

$$E_{ddi}^{mnp} = \frac{g_k P_{mnp}}{4\pi\epsilon_b\epsilon_0 R^3}. \tag{6.2}$$

Similarly the electric field created by the QD at the location of the MNP is denoted as E_{ddi}^{qd}, and is given by

$$E_{ddi}^{qd} = \frac{g_k P_{qd}}{4\pi\epsilon_b\epsilon_0 R^3}. \tag{6.3}$$

In the above expressions g_k is called the polarization parameter, which takes values $g_k = 2$ ($g_k = -1$) when the dipole lies parallel (perpendicular) to the vector $\mathbf{R}$ linking the centers of the MNP and QD [20].

The total electric field experienced by the MNP is expressed as

$$E_{mnp} = E_p e^{-i\omega_p t} + E_c e^{-i\omega_c t} + E_{ddi}^{qd} e^{-i2\omega_p t} + c.c., \tag{6.4}$$

where the first, second, and third terms represent the electric field of the probe, control, and nonlinear QD-dipole field, respectively. Note that here $\omega_c \approx 2\omega_p$. Using the quasistatic approximation, the dipole moment induced in the MNP due to the above electric field is obtained as [20]

$$P_{mnp} = \chi_{mnp}^{(1)}(\omega_c)\left(E_c + E_{ddi}^{qd}\right)e^{-i\omega_c t} + \chi_{mnp}^{(2)}(\omega_p)E_p^2 e^{-2i\omega_p t}, \tag{6.5}$$

115

where

$$\chi_{mnp}^{(1)}(\omega) = 4\pi\epsilon_b\epsilon_0 a^3 \frac{\epsilon_m(\omega) - \epsilon_b}{\epsilon_m(\omega) + 2\epsilon_b}, \tag{6.6}$$

and

$$\chi_{mnp}^{(2)}(\omega) = \frac{m_e}{(4\pi)^3 e^3} \beta \left[\chi_{mnp}^{(1)}(\omega)\right]^2 \chi_{mnp}^{(1)}(2\omega). \tag{6.7}$$

In the above expressions, $\epsilon_m(\omega)$ is the dielectric constant of the MNP, a is the radius of the MNP, m_e is the electron mass, e is the electron charge, and β is the nonlinear coefficient [21]. In Eq. 6.5, the linear contribution to the MNP polarization from the probe field (i.e., $\chi_{mnp}^{(1)}E_p e^{-i\omega_p t}$) has been neglected because ω_p is far away from ω_{sp}. Note that the surface plasmon resonance frequency ω_{sp} for the MNP can be calculated by setting the real part of the denominator in $\chi_{mnp}^{(1)}(\omega)$ equal to zero and solving for frequency. When $\omega_c \approx \omega_{sp}$, the value of $\chi_{mnp}^{(1)}$ becomes very large and the MNP produces an enhanced local electric field. This leads to a dipole-dipole interaction between the QD and MNP, which is very strong when they are in close proximity to one another and there is resonance coupling between the QD, MNP, and the driving electric fields (i.e., when $\omega_{sp} = \omega_c = 2\omega_p$).

The total electric field felt by the QD is written as

$$E_{qd} = \frac{1}{2\epsilon_{eff}} \left(E_p^0 e^{-i\omega_p t} e^{i\phi_p} + E_{ddi}^{mnp} e^{-i\omega_c t} e^{i\phi_c} + E_{shg}^{mnp} e^{-i\omega_c t} e^{i\phi_c}\right) + c.c., \tag{6.8}$$

where $\phi_p = k_p z$, $\phi_c = k_c z$, and $\epsilon_{eff} = \left(2n_b^2 + n_{qd}^2\right)/3n_{qd}^2$, n_b and n_{qd} being the refractive index of the background dielectric material and QD, respectively. In the above expression, E_{shg}^{mnp} is the electric field at the QD produced by SH generation in the MNP, and is expressed as

$$E_{shg}^{mnp} = \frac{g_k}{4\pi\epsilon_b\epsilon_0 R^3} \chi_{mnp}^{(2)}(\omega_p)\left(E_p^0\right)^2. \tag{6.9}$$

Using Eq. 6.8, the equations of motion for the two-level two-photon density matrix elements

ρ_{ij} are obtained using the master equation method [19, 22] as

$$\frac{d\rho_{22}}{dt} = -\Gamma_{qd}\rho_{22} + i\left[\Omega_{2p} + \Lambda_{ddi}e^{i\Delta\phi} + \Lambda_{shg}^{mnp}e^{i\Delta\phi}\right]e^{i2\phi_p}\rho_{12} \tag{6.10}$$
$$-i\left[\Omega_{2p} + \Lambda_{ddi}^*e^{-i\Delta\phi} + \left(\Lambda_{shg}^{mnp}\right)^*e^{-i\Delta\phi}\right]e^{-i2\phi_p}\rho_{21}$$
$$\frac{d\rho_{12}}{dt} = -\left[\Gamma_{qd}/2 - i\left(\Delta + \Delta_S\right)\right]\rho_{12} + i\left[\Omega_{2p} + \Lambda_{ddi}^*e^{-i\Delta\phi} + \left(\Lambda_{shg}^{mnp}\right)^*e^{-i\Delta\phi}\right]e^{-i2\phi_p}\left(\rho_{22} - \rho_{11}\right),$$

where $\Delta\phi = \phi_c - 2\phi_p$ and

$$\Delta_S = \beta_S\left|\Omega_{2p} + \Lambda_{ddi} + \Lambda_{shg}^{mnp}\right|, \tag{6.11}$$

$$\Omega_{2p} = \frac{k_{21}\left(E_p^0\right)^2}{2\hbar\epsilon_{eff}^2}, \tag{6.12}$$

$$\Lambda_{ddi} = \frac{g_k\mu_{21}\chi_{mnp}^{(1)}\left(\omega_c\right)}{4\pi\hbar\epsilon_b\epsilon_0\epsilon_{eff}R^3}\left(E_c^0 + \frac{g_kP_{qd}}{4\pi\epsilon_b\epsilon_0 R^3}\right), \tag{6.13}$$

and

$$\Lambda_{shg}^{mnp} = \frac{g_k\mu_{21}\chi_{mnp}^{(2)}\left(\omega_p\right)}{4\pi\hbar\epsilon_b\epsilon_0\epsilon_{eff}R^3}\left(E_p^0\right)^2. \tag{6.14}$$

In Eq. 6.10, Γ_{qd} and μ_{21} are the linewidth and dipole moment, respectively, for the transition $|1\rangle \leftrightarrow |2\rangle$, and β_S is defined in Ref. [19]. The equations of motion for the remaining density matrix elements are easily obtained using the relations $\rho_{11} + \rho_{22} = 1$ and $\rho_{12} = \rho_{21}^*$. In the above expressions, the parameter Ω_{2p} denotes the two-photon Rabi frequency due to direct two-photon absorption in the QD from the probe field, the term Λ_{ddi} accounts for the dipole-dipole interaction between the QD and MNP, and the quantity Λ_{shg}^{mnp} is the contribution from the field produced by SH generation in the MNP. Finally, the parameter Δ_S represents the dynamic Stark shift which appears due to frequency shifts in the levels $|1\rangle$ and $|2\rangle$ induced by virtual transitions to the intermediate levels $|n\rangle$ [19].

Transforming the density matrix elements as $\rho_{12} = \widetilde{\rho}_{12}e^{-i2\phi_p}$ and $\rho_{21} = \widetilde{\rho}_{21}e^{i2\phi_p}$, the density matrix equations of motion in Eq. 6.10 reduce to

$$\frac{d\rho_{22}}{dt} = -\Gamma_{qd}\rho_{22} + i\left(\Omega_{2p} + \Lambda_{ddi} + \Lambda_{shg}^{mnp}\right)\widetilde{\rho}_{12} - i\left[\Omega_{2p} + \Lambda_{ddi}^* + \left(\Lambda_{shg}^{mnp}\right)^*\right]\widetilde{\rho}_{21} \tag{6.15}$$
$$\frac{d\widetilde{\rho}_{12}}{dt} = -\left[\Gamma_{qd}/2 - i\left(\Delta + \Delta_S\right)\right]\widetilde{\rho}_{12} + i\left[\Omega_{2p} + \Lambda_{ddi}^* + \left(\Lambda_{shg}^{mnp}\right)^*\right]\left(\rho_{22} - \rho_{11}\right).$$

Note that the elements ρ_{11} and ρ_{22} are not affected by the phase factors because they are real quantities. Here $k_p = 2\pi/\lambda_p$ and $k_c = 2\pi/\lambda_c$ are used in the expressions of the phases for the probe and control field, respectively, where λ_p (λ_c) is the wavelength of the probe (control) field. The phase factors are then rewritten as $\exp(i2\pi z/\lambda_p)$ and $\exp(i2\pi z/\lambda_p)$. In the present study, λ_p and λ_c are on the order of several hundred nanometers, while the distance z is on the order of the diameter of the QD, i.e., ˜3 nm for a typical CdS QD. Hence, the phase factors $\exp(i2\pi z/\lambda_p)$ and $\exp(i2\pi z/\lambda_p)$ are close to unity. This is known as the quasistatic approximation in the literature [20, 23]. Here the quasistatic approximation is used to calculate the dipole-dipole interaction, SH generation and TPPL. In the quasistatic approximation the phase-matching condition is also satisfied. One can also say that the phase-matching condition does not apply in the quasistatic approximation.

SH generation occurs in the QD due to the nonlinear polarization induced by the transition $|1\rangle \leftrightarrow |2\rangle$. The electric field produced by SH generation in the QD is obtained as

$$E_{qd}^{SH} = \frac{P_{qd}}{r_{qd}^3 \epsilon_b \epsilon_0}, \tag{6.16}$$

where P_{qd} is the nonlinear polarization of the QD given in Eq. 6.1. The intensity of the electric field produced by SH generation in the QD is then calculated as $I_{qd}^{SH} = \frac{1}{2}\varepsilon_0 c\sqrt{\epsilon_b}\left|E_{qd}^{SH}\right|^2$, which gives

$$I_{qd}^{SH} = \frac{\varepsilon_0 c\sqrt{\epsilon_b}}{2} \left| \frac{(k_{11}\rho_{11} + k_{22}\rho_{22} + 2k_{21}\rho_{21})\, E_p}{r_{qd}^3 \epsilon_b} \right|^2. \tag{6.17}$$

Note that the intensity of the electric field produced via SH generation from the QD depends on the density matrix elements ρ_{ij}, which in turn depend on the dipole field produced by the MNP as shown in Eqs. 6.15. In a similar manner the SH field intensity produced by the MNP is calculated as

$$I_{mnp}^{SH} = \frac{1}{2}\varepsilon_0 c n_b \left| \frac{\chi_{mnp}^{(2)}\,(\omega_p)\, E_p^2}{r_{mnp}^3 \epsilon_b \epsilon_0} \right|^2. \tag{6.18}$$

In this case, however, SH generation in the MNP does not depend on the dipole field produced by the QD.

The QD absorbs energy from the external probe field through a two-photon absorption process. The energy acquired via two-photon absorption is subsequently emitted through TPPL.

The power absorbed by the QD is denoted by W_{qd} and can be calculated as [2]

$$W_{qd} = \hbar\omega_0 \Gamma_{pl} \rho_{22}. \tag{6.19}$$

Here Γ_{pl} is the TPPL decay rate. Notice that W_{qd} depends on ρ_{22}, which in turn depends on the dipole-dipole interaction between the QD and MNP through Eqs. 6.15. For a sample consisting only of QDs, the power absorbed by the QD is W_{qd}^0, which is evaluated from Eqs. 6.15 in the absence of the dipole-dipole interaction terms (i.e. $\Lambda_{ddi} = \Lambda_{shg}^{mnp} = 0$). On the other hand, the power absorbed by the QD solely due to the interaction with the MNP is denoted as W_{qd}^{ddi} and is evaluated from Eqs. 6.15 in the absence of the probe laser field (i.e. $\Omega_{2p} = 0$). The intensity of the TPPL signal from the QDs alone can then be expressed as

$$I_{2p}^{qd} = \frac{W_{qd}^0}{4\pi r_{qd}^2}, \tag{6.20}$$

while the intensity of the TPPL signal from the QD-MNP hybrid is

$$I_{2p}^{qd-mnp} = \frac{W_{qd}^0 - W_{qd}^{ddi}}{4\pi r_{qd}^2}. \tag{6.21}$$

6.4   Results and Discussion

Numerical simulations for the intensity of the SH field produced by a CdS QD in the presence of either a Au or Ag MNP have been performed. In these simulations, parameters $\epsilon_{qd} = 6.4$ and $\epsilon_b = 1.96$ have been used, while the dielectric constant of the MNP is taken for Au and Ag from the experimental data in Ref. [24]. To calculate the thermo-optic properties of the background dielectric medium, parameters $\kappa_{th} = 0.2$ W/(mK) and $\beta_b = 1 \times 10^{-3}$ K^{-1} were used, while those for the CdS QDs were taken as $\kappa_{th} = 0.2$ W/(mK) and $\beta_{qd} = 10^{-6}$ K^{-1} [25]. Note that the volume expansion coefficient for CdS is much smaller than that for the background aminosilane matrix, and so in our calculations only ϵ_b can be affected significantly by plasmonic heating. The surface plasmon resonance wavelengths for the Au and Ag MNPs were measured experimentally as $\lambda_{Au}^{sp} \simeq 532$ nm and $\lambda_{Ag}^{sp} \simeq 400$ nm, respectively. The two-photon coefficient and dipole moment in the CdS QD were taken as $k_{21} = 0.9 \times 10^{-34}$ C^{2}m/N and $\mu_{21} = 1.3\ e$

nm, respectively, and in the numerical simulations the effective linewidth $\hbar\Gamma_{qd} = 0.06$ eV was used, which was determined from the experimental data (Figure 6-4).

In the numerical simulations, the probe field is described by a Gaussian pulse such that

$$E_p = E_p^0 e^{-i\phi_p} \exp\left[-\frac{(t - t_0)^2}{2\sigma^2}\right] \tag{6.22}$$

where $\sigma = 50$ fs is the pulse width and E_p^0 is the peak amplitude obtained from the average power of the probe laser (270 mW) and the spot diameter (5 μm). The density matrix elements are obtained by numerically solving Eqs. 6.15 at the time of probe field pulse center, t_0.

In Figure 6-4 the (normalized) intensity of the SH field from the CdS QD in the presence of the Au MNP is plotted (see solid curve). For this calculation only the strongest QD-MNP dipole-dipole interaction is considered, corresponding to QDs that have diffused close to the Au MNP, i.e., when R is its minimum value ($R = r_{qd} + a$). The majority of the QDs in the ~5 μm QD-aminosilane film are comparatively further away and do not participate in the dipole-dipole coupling. Note that a good agreement between theory and experiment is found. The inset in Figure 6-4 shows numerical simulations for the SH signal intensity when the control field is applied and the separation between the Au MNP and the CdS QD, R, is increased. Here the simulations show that increasing the QD-MNP separation decreases the strength of the dipole coupling field, thereby reducing the SH signal enhancement due to Λ_{ddi}. A similar effect can be observed if the control field power is decreased.

Theoretical calculations for the SH signal intensity have also been presented in Figure 6-5(a) as a function of the CW control field power for the Au MNP-QD hybrid system (see solid curve in Figure 6-5(a); square points correspond to experimental data). It is found that there is an increase in the SH signal intensity from the CdS QDs as the control field power is increased. There is a good agreement between the theoretical calculations and experimental results. The observed enhancement is due to the dipole field produced by the Au MNPs. Here, a strong dipole field is produced by the coupling between the CW control field and the Au MNP because the control field ($\lambda_c = 532$ nm) is in resonance with the surface plasmon frequency of the Au MNP ($\lambda_c = \lambda_{Au}^{sp} = 532$ nm). Additionally, the SH signal intensity is plotted for the case where the MNP is far away from the QD or when the control field is not in resonance with the surface
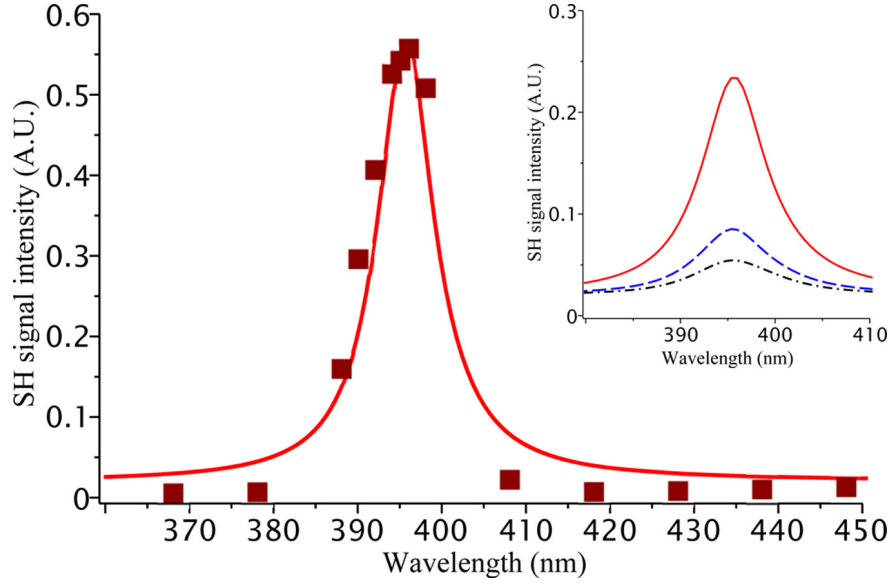
Figure 6-4: (a) Photon counting experiment on the $a = 40$ nm Au MNP-QD hybrid system (square points) and numerical simulation results (solid curve) in arbitrary units. Here the control field power is 15 mW. In the numerical simulation, $R = a + r_{qd}$ and $k_{11} = -k_{22} = k_{21}/10$. Inset: Numerical simulations for the SH signal for $R = 50$ nm (solid curve), 70 nm (dashed curve) and 100 nm (dash-dotted curve).

plasmon frequency. In either situation the numerical results are indicated by the dashed curve in Figure 6-5(a). Note that the hybrid system can be switched from a low-SH signal intensity state (dashed curve) to a high-SH signal intensity state (solid curve) by applying the CW control laser field. The enhancement of the SH signal can also be switched on and off by changing the frequency of the control laser field. When $\lambda_c = \lambda_{Au}^{sp}$, the SH signal will be enhanced due the strong dipole-dipole coupling (solid curve) and when $\lambda_c \neq \lambda_{Au}^{sp}$ the SH signal will not change (dashed curve) because the dipole-dipole coupling is absent.

In Figure 6-5(b) the SH signal intensity as a function of the CW control field power is presented for the Ag MNP-QD hybrid system. In this case there is only a very small enhancement of the SH signal when the CW control laser field is applied. This is because there is negligible coupling between the control field ($\lambda_c = 532$ nm) and the surface plasmon resonance of the Ag MNPs ($\lambda_{Ag}^{sp} \simeq 400$ nm). The inset in Figure 6-5(b) shows a numerical simulation for the SH signal as a function of the control field power when the control field is resonant with the surface
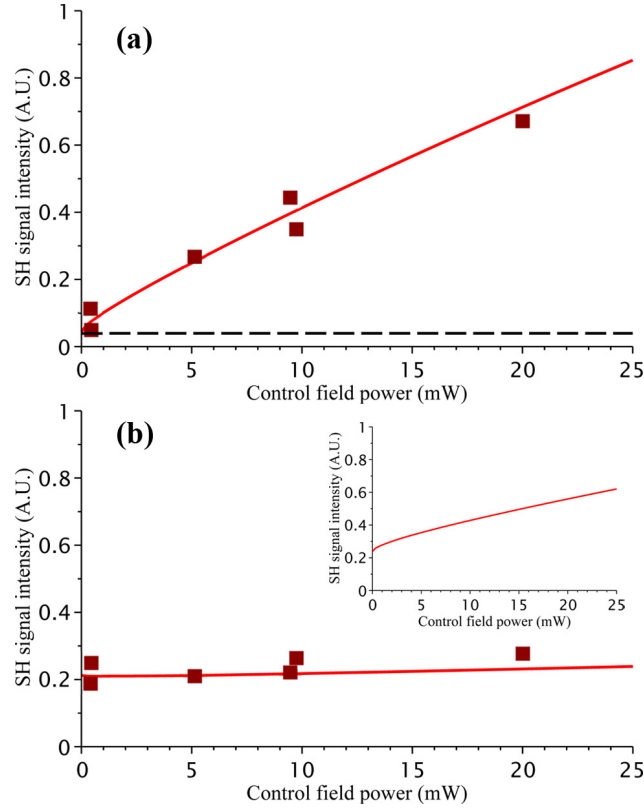
Figure 6-5: (a) SH signal (at $\lambda = 395$ nm) for the Au MNP-QD hybrid system vs. control field power. The square points and solid curve correspond to the experimental and numerical results, respectively. The dashed line indicates the SH signal when the control field is absent. (b) SH signal for the Ag MNP-QD hybrid vs. control field power, where the square points and solid curve correspond to experimental and numerical results, respectively. Inset: Numerical simulation of the SH signal for the Ag MNP-QD hybrid system when $\lambda_c = \lambda_{Ag}^{sp} = 400$ nm.

plasmons in the Ag MNPs such that $\lambda_c = \lambda_{Ag}^{sp} = 400$ nm. In this case it is found that the SH signal is enhanced as the control field power is increased. Note however that the increase in the SH signal intensity predicted for the QD-Ag MNP hybrid when $\lambda_c = \lambda_{Ag}^{sp} = 400$ nm is less than that observed from the QD-Au MNP hybrid when $\lambda_c = \lambda_{Au}^{sp} = 532$ nm. The enhancement of SH generation is weaker for the Ag MNP because its size is less than that of the Au MNP ($a_{Ag} = 10$ nm whereas $a_{Au} = 40$ nm), and dipole field produced by the MNP depends on the size of the MNP through Eq. 6.5.

In Figure 6-4, the SH signal intensity spectra originating from the QD-MNP hybrid system
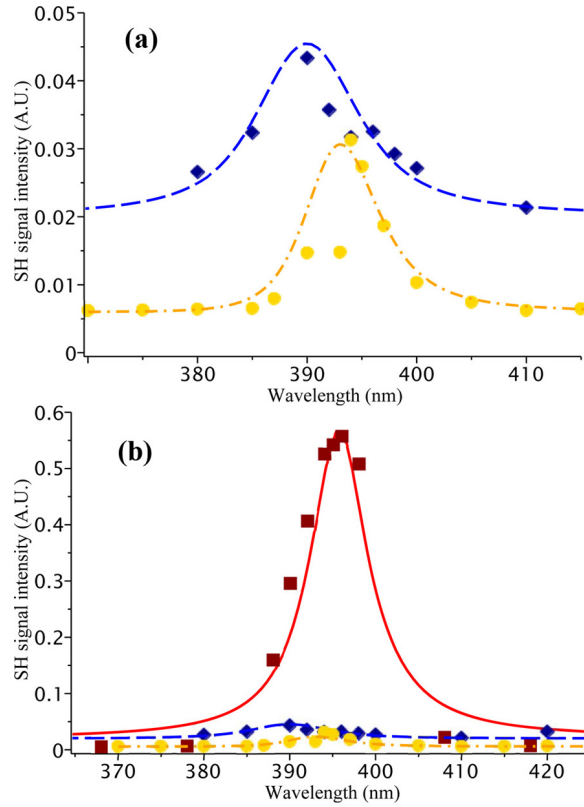
Figure 6-6: (a) Experimental data for the SH signal intensity from the CdS QDs alone (solid diamonds) and Au MNPs alone (solid circles). For the QD sample the Ti:Sa wavelength has been taken at $\lambda = 780$ nm rather than 790 nm elsewhere. Numerical simulation results for the QD and MNP are shown by the dashed and dash-dotted curves, respectively. (b) The combined results from Figures 6-4 and 6-6(a).

is plotted. However, it is not clear from this figure alone what the contributions to this signal are from the QD and the MNP individually. Therefore, a control experiment consisting of measurements on samples that contain only gold, silver or QDs has been performed. The experimental results are plotted in Figure 6-6(a), where the solid circles and solid diamonds correspond to the data obtained from the QDs and Au-MNPs, respectively. Using the present theory for SH generation, numerical simulations for the SH signal intensity from the QD and Au-MNP alone have also been performed, which are indicated in Figure 6-6(a) by the dashed and solid curves, respectively. A good agreement between the theoretical and experimental results is obtained for both the QD and Au-MNP. To compare the contribution from SH generation
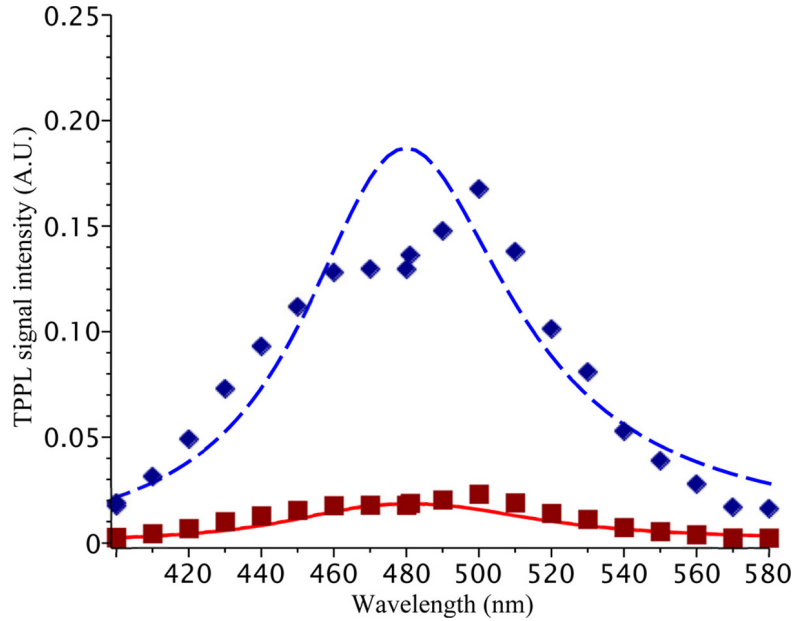
Figure 6-7: Two-photon photoluminescence (TPPL) signal from the CdS QDs in the absence (solid diamonds, dashed curve) and presence (solid squares, solid curve) of the Au MNPs. The points and curves correspond to the experimental and theoretical results, respectively. In these simulations, $\hbar\Gamma_{pl} = 6.6$ μeV was used.

of the isolated QDs and MNPs with the QD-MNP hybrid system, the combined results of Figures 6-4 and 6-6(a) are plotted in Figure 6-6(b). Figure 6-6(b) shows clearly that there is an enhancement of the SH signal intensity from the QDs in the presence of the Au-MNPs. This enhancement is due to the dipole-dipole interaction between the QDs and MNPs as mentioned previously.

TPPL from the QD has also been measured experimentally and studied theoretically. The results for TPPL are presented in Figure 6-7, where the solid diamonds (dashed curve) and solid squares (solid curve) correspond to the experimental data (numerical simulations) for the QDs alone and QD-Au MNP hybrid system. In both the theoretical and experimental results, there is a quenching of the TPPL signal from the QD in the presence of the MNPs. Similar TPPL quenching has been observed by Jais et al. in Ref. [18] for a CdS-QD/Ag-MNP hybrid system. Single-photon excitation photoluminescence quenching has also been observed experimentally for CdSe-ZnS QDs in the presence of Au MNPs [26]. For the QD-MNP

hybrid system considered here it is found that as the intensity of the control field increases the photoluminescence quenching is enhanced.

The influence of plasmonic heating on SH generation has been investigated theoretically in the Appendix of this chapter, as the SH spectrum from the QDs is influenced by the plasmonic heating due to the MNPs. In the present case is was found that the plasmonic heating has a negligible effect on SH generation in the QDs (see Figure 6-9 in the Appendix of this chapter).

Finally, to understand the physics of SH generation and TPPL, the time evolution of the QD density matrix elements ρ_{22} and ρ_{12} has been studied, as they are directly related to SH generation and TPPL. Note that ρ_{12}, which controls the coherence between states $|1\rangle$ and $|2\rangle$, is a complex quantity and can be expressed as $\rho_{12} = |\rho_{12}|\, e^{i\phi}$ where $\phi = \arctan(\operatorname{Im}\rho_{12}/\operatorname{Re}\rho_{12})$. On the other hand, ρ_{22} represents the probability of finding the QD in the excited state $|2\rangle$. The time variation of ρ_{11} can be found from ρ_{22} via the condition $\rho_{11} + \rho_{22} = 1$.

In Figures 6-8(a) and 6-8(b), ρ_{22} and $|\rho_{21}|$, respectively, are plotted as functions of time for zero probe field detuning ($\Delta = 0$ or $\lambda_p = 790$ nm). Here the solid and dashed curves are plotted in the presence or absence of the dipole-dipole interaction between the QD and MNP, respectively. In performing these simulations, it is considered that initially only the ground state in the QD is populated, i.e., $\rho_{11}(0) = 1$, and the excited state is empty, i.e., $\rho_{22}(0) = 0$. Note from Figure 6-8(a) that when the probe field is applied, ρ_{22} increases with time and reaches a steady-state. There are no observable Rabi oscillations because in the present case the Rabi frequency Ω_{2p} related to the probe field is smaller than the linewidth Γ_{qd}. This behaviour is consistent with results found in the quantum optics literature [21, 22].

When the dipole-dipole interaction is included in the simulation, it is found that the value for ρ_{22} increases, which in turn enhances the TPPL quenching. In Figure 6-8(b) the amplitude of the density matrix element ρ_{21} has been plotted both in the absence or presence of the dipole-dipole interaction. Note that in either case, $|\rho_{21}|$ also increases in time and reaches a steady-state value. In the presence of the dipole-dipole interaction this term also increases. To understand the enhancement of the SH signal produced by the QD due to the dipole-dipole interaction, one can use the following argument: It is found that in Eq. 6.17, the main contribution originates from the term which depends on ρ_{12}. If the first two terms in this equation are ignored then the SH signal intensity is proportional to $|\rho_{12}|^2$, and the phase factor does not appear. In other
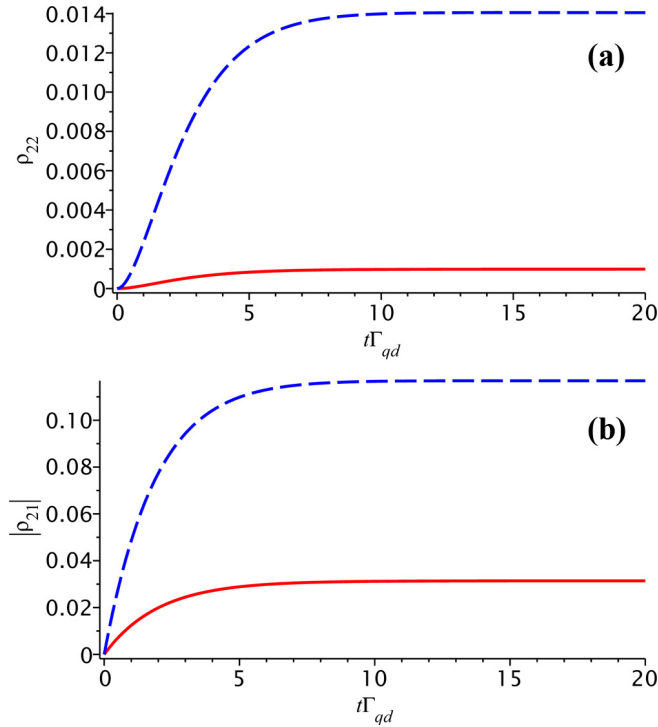
Figure 6-8: Time evolution of the density matrix elements ρ_{22} (a) and $|\rho_{21}|$ (b) in the absence (solid curves) or presence (dashed curves) of the dipole-dipole interaction. Initially the QD is in the ground state, i.e. $\rho_{11}(0) = 1$.

words, due to the enhancement in $|\rho_{12}|$ from the dipole-dipole interaction the SH generation process in the QD is enhanced.

6.5 Conclusions

In conclusion, SH generation and TPPL in QD-MNP hybrid systems have been investigated both theoretically and experimentally. It is found that an applied CW control field can be used to enhance the SH signal intensity from the QDs. The enhancement of the SH signal intensity can be switched on or off by changing the intensity of the control field when it is resonant with the surface plasmons in the MNP. Alternatively, the SH signal enhancement can be switched on or off by changing the frequency of the control field. These findings can be used to fabricate all-optical nano-switching devices using QD-MNP hybrid systems. The role of plasmonic heating

from the MNPs in the observed SH signal enhancement has also been investigated, and is found to have a negligible effect on SH generation in the QDs.

Appendix: Plasmonic Heating

Here the influence of plasmonic heating on the SH signal intensity spectrum of the QD-MNP hybrid system is investigated theoretically. Due to the plasmonic heating of the MNP, the temperature of the surrounding aminosilane matrix increases, which in turn changes its refractive index (dielectric constant). The SH spectrum is influenced by the plasmonic heating because it also depends on the refractive index of the background medium, n_b.

Plasmonic heating is the process by which power is transfered out of the surface plasmons in an MNP and converted to thermal energy [27, 28]. The mechanism for plasmonic heating can be understood as follows: The applied electric field drives surface plasmons in the MNP and the energy gained by these surface plasmons is converted into heat. This heat diffuses away from the MNP and leads to an elevated temperature in the surrounding medium. Because MNPs are very poor light emitters, one can consider that all the power absorbed by the MNP from an external field is converted into thermal energy. Therefore, it is considered that the power absorbed by the MNP from probe field, control field and the dipole field from the QD is converted into thermal energy.

The power absorbed by the MNP due to the external fields can be calculated as follows [23, 28]

$$Q_{mnp} = \left\langle \int j_{mnp} E_{mnp} dV \right\rangle. \tag{6.23}$$

In the above expression, j_{mnp} is the magnitude of the electric current density induced in the MNP and the integration is performed over the volume of the MNP, $V_{mnp} = 4\pi a^3/3$. The symbol $\langle ... \rangle$ denotes the time average taken over the period of the oscillating laser fields. The current density in the MNP is calculated as

$$j_{mnp} = \frac{1}{V_{mnp}} \frac{dP_{mnp}}{dt}. \tag{6.24}$$

After performing some mathematical manipulation, an expression for the plasmonic heating

power is obtained as

$$Q_{mnp} = \omega_c E_c^2 \operatorname{Im}\left[\chi_{mnp}^{(1)}(\omega_c)\right]. \tag{6.25}$$

Here the contributions to Q_{mnp} from the probe field and dipole field produced by the QD are negligible compared to that from the CW control field, and so they have been neglected in the above expression for simplicity. Note that the thermal power Q_{mnp} generated by the MNP becomes especially strong in the regime of plasmon resonance, i.e. when $\operatorname{Re}\epsilon_m \simeq -2\epsilon_b$ (see Eq. 6.5).

The heat generated by the MNP raises the temperature of the surrounding medium by some amount ΔT, which is quantified by [28]

$$\Delta T = \frac{Q_{mnp}}{4\pi R \kappa_{th}}, \tag{6.26}$$

where R is the distance from the center of the MNP and κ_{th} is the thermal conductivity of the surrounding medium.

The medium surrounding the MNP in the present case consists of CdS QDs and aminosilanes. Due to the change in the temperature there is also a change in the refractive index of the surrounding medium. This phenomenon is known as the photothermal effect, which leads to a shift in the refractive index of the QDs (n_{qd}) and aminosilanes (n_b) as [29]

$$n_i' = n_i + \frac{|\beta_i|}{6n_i}\left(n_i^2 + 2\right)\left(n_i^2 - 1\right)\Delta T \tag{6.27}$$

In the above expression, the subscript i denotes either $i = qd$ (CdS QD) or $i = b$ (aminosilane matrix), and β_i is the volume expansion coefficient of the ith material.

In the present model for the QD-MNP hybrid system, the SH field intensity and TPPL are calculated from the dipole moment of the QD P_{qd}, which in turn depends on the refractive indices of the aminosilane matrix n_b (i.e. ϵ_b) and QD n_{qd} (i.e. ϵ_{qd}). Due to plasmonic heating from the MNP, the refractive indices of the QD and aminosilanes will change, thereby affecting SH generation and TPPL.
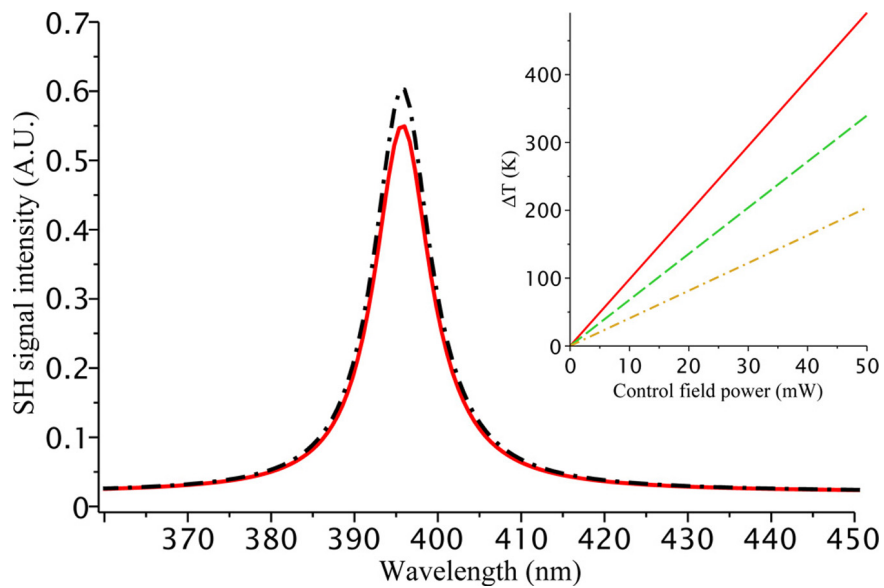
Figure 6-9: SH signal intensity from the QD-Au MNP hybrid system when the effect of plasmonic heating is included (solid curve) and omitted (dash-dotted curve). The solid curve shown here corresponds to the solid curves shown in Figures 6-4 and 6-6(b). Inset: Temperature change in the aminosilane matrix surrounding the Au MNP vs. control field power. Here the solid, dashed and dash-dotted curves correspond to $R = r_{qd} + a$, 60 nm and 100 nm, respectively.

Bibliography

[1] M. Achermann, *J. Phys. Chem. Lett.* **1**, 2837 (2010).

[2] R. D. Artuso and G. W. Bryant, *Phys. Rev. B* **82**, 195419 (2010).

[3] M. R. Singh, D. G. Schindel, and A. Hatef, *Appl. Phys. Lett.* **99**, 181106 (2011).

[4] M. I. Stockman, D. J. Bergman, C. Anceau, S. Brasselet, and J. Zyss, *Phys. Rev. Lett.* **92**, 057402 (2004).

[5] M. Zielinski, S. Winter, R. Kolkowski, C. Nogues, D. Oron, J. Zyss, and D. Chauvat, *Opt. Express* **19**, 6657 (2011).

[6] P. Mühlschlegel, H.-J. Eisler, O. J. F. Martin, B. Hecht, and D. W. Pohl, *Science* **308**, 1607 (2005).

[7] A. Bouhelier, M. Beversluis, A. Hartschuh, and L. Novotny, *Phys. Rev. Lett.* **90**, 013903 (2003).

[8] H. Husu, B. K. Canfield, J. Laukkanen, B. Bai, M. Kuittinen, J. Turunen, and M. Kauranen, *Metamaterials* **2**, 155 (2008).

[9] T. Hanke, G. Krauss, D. Träutlein, B. Wild, R. Bratschitsch, and A. Leitenstorfer, *Phys. Rev. Lett.* **103**, 257404 (2009).

[10] A. Benedetti, M. Centini, C. Sibilia, and M. Bertolotti, *J. Opt. Soc. Am. B* **27**, 408 (2010).

[11] D. P. Fromm, A. Sundaramurthy, P. J. Schuck, G. Kino, and W. E. Moerner, *Nano Lett.* **4**, 957 (2004).

[12] A. Sundaramurthy, P. J. Schuck, N. R. Conley, D. P. Fromm, G. S. Kino, and W. E. Moerner, *Nano Lett.* **6**, 355 (2006).

[13] C. Anceau, S. Brasselet, J. Zyss, and P. Gadenne, *Opt. Lett.* **28**, 713 (2003).

[14] I. Diukman, L. Tzabari, N. Berkovitch, N. Tessler, and M. Orenstein, *Opt. Express* **19**, A64 (2011).

[15] K. T. Shimizu, W. K. Woo, B. R. Fisher, H. J. Eisler, and M. G. Bawendi, *Phys. Rev. Lett.* **89**, 117401 (2002).

[16] M. Lunz, V. A. Gerard, Y. K. Gun'ko, V. Lesnyak, N. Gaponik, A. S. Susha, A. L. Rogach, and A. L. Bradley, *Nano Lett.* **11**, 3341 (2011).

[17] H. M. Gong, X. H. Wang, Y. M. Du, and Q. Q. Wang, *J. Chem. Phys.* **125**, 024707 (2006).

[18] P. M. Jais, C. von Bilderling, and A. V. Bragas, *Papers in Physics* **3**, 030002 (2011).

[19] P. Meystre and M. Sargent III, *Elements of Quantum Optics*, 4th ed. (Springer-Verlag, Berlin, 2007).

[20] D. Sarid and W. A. Challener, *Modern Introduction to Surface Plasmons: Theory, Mathematica Modeling, and Applications* (Canbridge University Press, New York, 2010).

[21] R. W. Boyd, *Nonlinear Optics*, 3rd ed. (Academic, New York, 2008).

[22] M. O. Scully and M. S. Zubairy, *Quantum Optics* (Cambridge University Press, Cambridge, UK, 1997).

[23] L. Novotny and B. Hecht, *Principles of Nano-Optics* (Cambridge University Press, New York, 2006).

[24] P. B. Johnson and R. W. Christy, *Phys. Rev. B* **6**, 4370 (1972).

[25] W. Martienssen and H. Warlimont (Eds.), *Springer Handbook of Condensed Matter and Materials Data* (Springer, Berlin, 2005).

[26] T. Pons, I. L. Medintz, K. E. Sapsford, S. Higashiya, A. F. Grimes, D. S. English, and H. Mattoussi, *Nano Lett.* **7**, 3157 (2007).

[27] N. Harris, M. J. Ford, and M. B. Cortie, *J. Phys. Chem. B* **110**, 10701 (2006).

[28] A. O. Govorov and H. H. Richardson, *Nano Today* **2**, 30 (2007).

[29] S. E. Bialkowski, *Photothermal Spectroscopy Methods for Chemical Analysis* (John Wiley and Sons Inc., Toronto, 1996).

Chapter 7

Concluding Remarks

In this thesis, nanophotonics and light-matter interactions were studied in a variety of photonic and metallic heterostructures. The nanophotonic systems explored in this thesis included single and double photonic quantum wells (waveguides), nonlinear photonic crystal waveguides, and graphene/metallic nanocomposites. These heterostructures were found to possess novel optical properties that surpass the capabilities of their individual components. For example, the combination of two different photonic crystals in a photonic quantum well heterostructure resulted in the formation of bound photonic states and resonant tunnelling peaks in the structure's transmission spectrum, while individually the constituent photonic crystals would simply reflect light at certain frequencies. Similarly, the dipole-dipole interaction between excitons in a quantum dot and plasmons in a graphene nanodisk or metal nanoparticle was shown to lead to energy transfer or the enhancement of optical nonlinearities in the individual nanostructures. As nanofabrication techniques improve, the number of available nanostructures that can be combined to create heterostructures or nanocomposites with exotic optical properties will increase significantly. The results presented in this thesis can be used to motivate future experimental or theoretical investigations on heterostructures made using photonic crystals, quantum dots, graphene, and noble metal nanoparticles.

In Chapter 2, the resonant photonic tunnelling effect was studied in both single (PQW) and double photonic quantum well (DPQW) heterostructures made using two photonic crystals. The transfer matrix method was used to simulate the transmission coefficient of these heterostructures along the direction of confinement. The transmission spectra for the PQW

and DPQW heterostructures reveal sharp peaks of perfect transmission at specific energies, indicating the energy levels of resonant states. In the PQW heterostructure, discrete resonant tunnelling peaks appear in the transmission spectra, the number of which can be changed by adjusting the width of the photonic well. In the DPQW heterostructure, resonant tunnelling peaks occur in split pairs due to the coupling of degenerate states in two photonic wells. It is shown that the energy splitting can be controlled by varying width of the photonic barrier separating the wells. It is anticipated that the resonant tunnelling phenomenon described in this chapter can be used to develop photonic switching devices, high-quality optical filters and other optoelectronic devices.

In Chapter 3, the resonant states and transmission spectra in DPQW heterostructures were investigated in greater detail. Expressions for the energy levels of bound photonic states and their energy splitting in the DPQW heterostructure were derived, and the transmission coefficient of the system was simulated using the transfer matrix method. In this chapter, Kerr-nonlinear photonic crystals were included in the design of the DPQW heterostructures. The use of nonlinear photonic crystals in the DPQW heterostructure allows the system to function as an all-optical switch, whereby an incident probe laser field applied along the direction of confinement can be switched between transparent or reflecting states by an external pump laser field. It is demonstrated that the nonlinear DPQW heterostructure can be switched between zero to one or more pairs of resonant states by varying the intensity of the pump laser field or by applying external stress or strain fields to the system. The results presented in this chapter may be used to develop all-optical switching devices, tunable filters, and coupled waveguides.

Light-matter interactions in a graphene nanocomposite heterostructure were investigated in Chapter 4. In this chapter, the dipole-dipole interaction and energy transfer were studied in a quantum dot (QD)-graphene nanodisk nanocomposite system using the density matrix method. The graphene nanocomposite was embedded in a Kerr-nonlinear photonic crystal, which served as an optically-tunable photonic reservoir for the QD. Here it was demonstrated that energy absorption in the QD and energy transfer from the QD to graphene can be switched on or off (i.e. controlled) by changing the distance between the QD and graphene or by applying a pump laser field to the nonlinear photonic crystal. It was also shown that the energy absorption/transfer rates in the graphene nanocomposite are highly sensitive to changes in

134

the thickness of graphene or the dielectric constant of the QD. The theory presented in this chapter is very general and can be applied to nanocomposite systems consisting of graphene and three-level quantum emitters such as quantum dots, nanocrystals, atoms, molecules, etc. The proposed nanocomposite system can be used to construct sensors, all-optical switches, and energy transfer/storage devices.

In Chapter 5, the enhancement and control of nonlinear optical processes in a graphene nanocomposite (heterostructure) was studied. Here, the strong local fields produced by plasmons in a graphene nanoflake were used to manipulate two-photon absorption in a proximal quantum dot. In this chapter, the density matrix method was used to simulate the two-photon absorption coefficient and power absorption in the QD. It was found that the two-photon absorption coefficient of the QD can be switched between single- or double-peaked spectra by changing the separation between the QD and graphene. The effect of an electrostatic gate voltage applied to the graphene nanoflake was also studied in this chapter. By tuning the gate voltage, the plasmon resonance frequency in the graphene nanoflake can be adjusted, thereby changing the frequency at which the maximum local field enhancement occurs. This phenomenon was used here to electrostatically control the two-photon absorption coefficient and power absorption in the QD, demonstrating that the present nanocomposite system can function as an electro-optic switch. The results presented in this chapter indicate that the present QD-graphene nanocomposite system can be used for nonlinear optical applications such as all-optical switching, biosensing, and signal processing.

Finally in Chapter 6, nonlinear optical processes in QD-metallic nanoparticle (MNP) hybrid systems were investigated both theoretically and experimentally. In the theoretical model, two-photon photoluminescence (TPPL) and second harmonic (SH) generation were studied using the density matrix method. A probe laser field is used to excite the QD via two-photon absorption, while a control field is applied to excite plasmons in the MNP. It is predicted that the dipole-dipole coupling between the QD and MNP results in an enhancement of SH generation and TPPL in the QD. In this chapter, experimental measurements of SH generation and TPPL in nanocomposite systems consisting of CdS QDs with either Au or Ag MNPs are reported. An enhancement of SH generation was observed when a control laser field was applied to the hybrid system and was resonant with the plasmons in the MNP. Good qualitative agreement

was found between the theoretical results and experimentally-obtained data for the QD-MNP nanocomposites. These findings can be used to fabricate all-optical nonlinear switching devices using QD-MNP hybrid systems.

There is already a colossal number of available photonic and metallic nanostructures that can be used to create optically-active heterostructures and nanocomposites. Countless possibilities for future research on heterostructures exist, as many different combinations and permutations of nanostructures can be explored. As an immediate extension of the present research, photonic crystal heterostructures can be combined with semiconductor and metallic nanocomposites. In such a system, the exciton-plasmon interaction between a quantum dot and a noble metal (or graphene) nanostructure could be manipulated by their interaction with the tunable bound photonic states in a Kerr-nonlinear photonic quantum well. Numerous possibilities also exist for metamaterial-based heterostructures. Metamaterials are a new class of artifical materials which possess exotic optical properties determined by the nano-scale organization of their structural components. For example, metamaterials based on periodic arrangements of metallic nanocomposites have been demonstrated to possess simultaneously negative dielectric permittivity and permeability for a range of frequencies in the electromagnetic spectrum. The interaction of metamaterials with optically-active media such as quantum dots or fluorescent molecules is currently being pursued.

Copyright and Reprint Permissions

AIP Publishing (Chapters 2 and 3)

Dear Dr. Cox:

Thank you for requesting permission to reproduce material from AIP Publishing LLC publications.

Permission is granted – subject to the conditions outlined below – for the following:

1) "Resonant Photons in Nanophotonic Quantum Well Heterostructures" in AIP Conference Proceedings, Volume 1147, Issue 1, page 256 (2009).

2) "Energy Splitting of Resonant Photonic States in Nonlinear Nanophotonic Double Waveguides" in Journal of Applied Physics, Volume 108, Issue 8, page 083102 (2010).

To be used in the following manner:

Reproduced in your Doctoral thesis entitled, "The Study of Nanophotonic Switching Mechanisms in Photonic and Metallic Heterostructures." It is also understood that the electronic version will be accessible through the Western Libraries web pages, the Library's web catalogue, and also through web search engines and that you are granting Library and Archives Canada and ProQuest/UMI a non-exclusive license to reproduce, loan, distribute, or sell single copies of the thesis by any means and in any form or format.

1. AIP Publishing LLC grants you non-exclusive world rights in all languages and media.

2. This permission extends to all subsequent and future editions of the new work.

3. The following copyright notice must appear with the material (please fill in the information indicated by capital letters): "Reprinted with permission from [FULL CITATION]. Copyright [PUBLICATION YEAR], AIP Publishing LLC."
Full citation format is as follows: Author names, journal title, Vol. #, Page #, (Year of publication).
For an article, the copyright notice must be printed on the first page of the article or book chapter. For figures, photographs, covers, or tables, the notice may appear with the material, in a footnote, or in the reference list.

4. This permission does not apply to any materials credited to sources other than the copyright holder.

Please let us know if you have any questions.

Sincerely,
Manager, Rights and Permissions
AIP Publishing

Nanoscale Research Letters (Chapter 2)

Authors of articles published in Nanoscale Research Letters are the copyright holders of their articles and have granted to any third party, in advance and in perpetuity, the right to use, reproduce or disseminate the article, according to the SpringerOpen copyright and license agreement.

SpringerOpen Access license agreement

Brief summary of the agreement

Anyone is free:
- to copy, distribute, and display the work;
- to make derivative works;
- to make commercial use of the work;

Under the following conditions: Attribution
- the original author must be given credit;
- for any reuse or distribution, it must be made clear to others what the license terms of this work are;
- any of these conditions can be waived if the authors gives permission.

Statutory fair use and other rights are in no way affected by the above.

American Physical Society (Chapter 4)

Dear Dr. Cox,

As the author of the APS paper, you have the right to use figures, tables, graphs, etc. in subsequent publications using files prepared and formatted by you or the APS-prepared versions. The appropriate bibliographic citation must be included.

Best wishes,
Circulation and Fulfillment Assistant
American Physical Society
http://librarians.aps.org/

Wiley-VCH (Chapter 6)

Dear Joel Cox

According to our Copyright Transfer Agreement, the Contributor may archive the submitted version (= the pre-peer review version) of his Contribution:

C. PERMITTED USES BY CONTRIBUTOR

1. Submitted Version. Wiley-VCH licenses back the following rights to the Contributor in the version of the Contribution as originally submitted for publication:

a. After publication of the final article, the right to self-archive **on the Contributor's personal intranet page or in the Contributor's institution's/ employer's institutional intranet repository or archive**. The Contributor may not update the submission version or replace it with the published Contribution. The version posted must contain a legend as follows: This is the pre-peer reviewed version of the following article: FULL CITE, which has been published in final form at [Link to final article].

For a printed version of the thesis, the Contributor may reprint the final version of the Contribution.

If material appears within our work with credit to another source, authorisation from that source must be obtained.

Credit must include the following components:

- Books: Author(s)/ Editor(s) Name(s): Title of the Book. Page(s). Publication year. Copyright Wiley-VCH Verlag GmbH & Co. KGaA. Reproduced with permission.
- Journals: Author(s) Name(s): Title of the Article. Name of the Journal. Publication year. Volume. Page(s). Copyright Wiley-VCH Verlag GmbH & Co. KGaA. Reproduced with permission.

With kind regards,

Senior Rights Manager
Rights & Licenses

Wiley-VCH Verlag GmbH & Co. KGaA
Boschstraße 12
69469 Weinheim
Germany
www.wiley-vch.de

Curriculum Vitae

Name: Joel Cox

Post-secondary   The University of Western Ontario
Education and   London, Ontario, Canada
Degrees: 2004-2008 Honors B.Sc. Physics

                        The University of Western Ontario
                        London, Ontario, Canada
                        2008-Present Ph.D. Physics

Honours and   Teaching Assistant Demonstrators Award of Excellence
Awards: 2008-2009

                        Faculty of Science Graduate Student Teaching Award
                        2010-2011

                        Province of Ontario Graduate Scholarship
                        2011-2012 and 2012-2013

Related Work   Teaching Assistant
Experience   The University of Western Ontario
                        2008-2013

Papers Published or Accepted in International Journals:

1) **J. D. Cox**, M. R. Singh, M. A. Antón and F. Carreño, "Plasmonic control of nonlinear two-photon absorption in graphene nanocomposites," J. Phys.: Condens. Matter (Accepted, 2013).

2) **J. D. Cox**, M. R. Singh, C. Von Bilderling, and A. V. Bragas, "A nonlinear switching mechanism in quantum dot and metallic nanoparticle hybrid systems," Adv. Opt. Mater. 1, 460 (2013).

3) M. A. Antón, F. Carreño, S. Melle, O. G. Calderón, E. Cabrera-Granado, **J. Cox**, and M. R. Singh, "Plasmonic effects in excitonic population transfer in a driven semiconductor-metal nanoparticle hybrid system," Phys. Rev. B 86, 155305 (2012).

4) **J. D. Cox**, M. R. Singh, G. Gumbs, M. A. Anton, and F. Carreno, "Dipole-dipole interaction between a quantum dot and a graphene nanodisk," Phys. Rev. B 86, 125452 (2012).

5) **J. D. Cox**, M. R. Singh, C. Racknor, and R. Agarwal, "Switching in polaritonic-photonic crystal nanofibers doped with quantum dots," Nano Lett. 11, 5284 (2011).

6) **J. D. Cox** and M. R. Singh, "Energy splitting of resonant photonic states in nonlinear nanophotonic double waveguides," J. Appl. Phys. 108, 083102 (2010).

7) **J. D. Cox**, J. Sabarinathan, and M. R. Singh, "Resonant photonic states in coupled heterostructure photonic crystal waveguides," Nanoscale Res. Lett. 5, 741 (2010).

8) **J. D. Cox** and M. R. Singh, "Resonant tunnelling in photonic double quantum well heterostructures," Nanoscale Res. Lett. 5, 484 (2010).

9) M. R. Singh and **J. D. Cox**, "Resonant photons in nanophotonic quantum well heterostructures," AIP Conf. Proc. 1147, 256 (2009).

Papers Communicated or in Preparation:

1) M. R. Singh, **J. D. Cox**, and M. Brzozowski "Photoluminescence and power absorption enhancement in metamaterial heterostructures," (Communicated, 2013).

Refereed Conference Presentations (* indicates presenting author):

- A. V. Bragas*, **J. D. Cox**, M. R. Singh, and C. von Bilderling, "Hybrid plasmonic nanodevices: switching mechanism for the nonlinear emission," International Conference on Nanomaterials, London, Canada (2013).

- **J. D. Cox*** and M. R. Singh, "Plasmon-enhanced two-photon absorption and second harmonic generation in graphene-quantum dot nanocomposites," Centre for Advanced Materials and Biomaterials Research Distinguished Lecturer and Research Day, London, Canada (2012).

- **J. D. Cox***, C. Racknor, D. Schindel and M. R. Singh, "Energy transfer mechanisms in nanocomposites," Theoretical Physics Workshop, London, Canada (2012).

- M. R. Singh*, **J. D. Cox**, D. Schindel, and A. Hatef, "Photon switching mechanism in graphene and quantum dot hybrid systems," Workshop on Graphene, San Sebastian, Spain (2011).

- **J. D. Cox*** and M. R. Singh, "Photon transmission through a 2-D photonic quantum well structure doped with quantum dots," Ontario Nanoscience and Nanotechnology Workshop, London, Canada (2010).

- **J. D. Cox**, J. Sabarinathan and M. R. Singh*, "Resonant photonic states in coupled heterostructure photonic crystal waveguides," Villa Conference in Interactions Among Nanostructures, St. Thomas, U. S. Virgin Islands (2009).

- **J. D. Cox*** and M. R. Singh, "Resonant tunnelling in photonic double quantum well heterostructures," Nano and Giga Challenges in Electronics, Photonics and Renewable Energy/14th Canadian Semiconductor Technology Conference, Hamilton, Canada (2009).

- M. R. Singh* and **J. D. Cox**, "Resonant photons in nanophotonic quantum well heterostructures," International Conference on Transport and Optical Properties of Nanomaterials, Allahabad, India (2009).

- T. Poepping*, B. Chronik, I. MacDonald, E. Wong, **J. Cox**, R. Taylor, and J. Battista, "A new medicine for physics: Using medical imaging as a tactic for teaching physics," Spring Perspectives on Teaching, London, Canada (2008).

- **J. D. Cox***, B. A. Chronik, E. Wong, and T. L. Poepping, "A handheld imaging system for teaching ultrasound principles," First Annual International Conference for Expanding Scholarship in Radiology Education, London, Canada (2007).